Spring 2013

Chemical, physical and mechanical properties of nanomaterials and its applications

Suman Ghorai
University of Iowa

Recommended Citation

Ghorai, Suman. "Chemical, physical and mechanical properties of nanomaterials and its applications." PhD (Doctor of Philosophy) thesis, University of Iowa, 2013.
http://ir.uiowa.edu/etd/2501.

CHEMICAL, PHYSICAL AND MECHANICAL PROPERTIES OF NANOMATERIALS AND ITS APPLICATIONS

by

Suman Ghorai

An Abstract

Of a thesis submitted in partial fulfillment
of the requirements for the Doctor of
Philosophy degree in Chemistry
in the Graduate College of
The University of Iowa

May 2013

Thesis Supervisor: Assistant Professor Alexei V. Tivanski

ABSTRACT

The contribution of atmospheric aerosols towards radiative forcing has a very high uncertainty due to their short atmospheric lifetime. The aerosol effects are largely controlled by the density, elemental composition, and hygroscopic properties of the aerosol particles. Therefore, we have performed designed new methodology using Scanning Transmission X-ray Microscopy (STXM), Atomic force spectroscopy (AFM), micro-FTIR spectroscopy and Scanning Electron Microscopy (SEM) to quantify these important aerosol properties. Hygroscopic properties are quantified by plotting the mass of water on a single particle basis, calculated from STXM, as a function of relative humidity. Alternatively, micro-FTIR spectra have been used to study the effect of composition of aerosol particles on the hygroscopic properties of NaCl. Moreover, a unique combination of STXM and AFM has been utilized to quantify density and elemental composition of micrometer dimensional particles. This method has also been extended towards exploring mixing state of particles, consisting of heterogeneously mixed inorganic and organic compounds. In addition to these above mentioned properties, the fate of an atmospheric particle is often altered by chemical transformation and that in turn is influenced by the atmospheric RH. Therefore, we have studied an unusual keto-enol tautomerism in malonic acid particles at high RH, which is not observed in bulk. This observation could potentially be utilized to significantly improve the models to estimate Secondary Organic Aerosols (SOA). Using STXM and micro-FTIR technique, RH dependent equilibrium constant of the tautomerism reaction has been quantified as well.

Organic nanocrystals capable of undergoing solid state photochemical changes in a single-crystal-to-single-crystal (SCSC) manner have been particularly important in fabricating molecular switches, data storage devices etc. Mechanical properties of these nanomaterials may control its SCSC reactivity. In addition, investigation of mechanical stiffness is important to define allowable limit of stiffness towards device application. Therefore, we studied mechanical properties of series organic nano cocrystals primarily consisting of trans-1,2-bis(4-pyridyl)ethylene and substituted resorcinol using AFM nanoindentation technique. Dependence of mechanical properties and SCSC reactivity on the resorcinol structure is also investigated as well. Moreover, photolithography on the thin film of these organic cocrystals has been performed to demonstrate its applicability as a photoresist.

Abstract Approved: ______________________________
Thesis Supervisor

____
Title and Department

____
Date

CHEMICAL, PHYSICAL AND MECHANICAL PROPERTIES OF NANOMATERIALS AND ITS APPLICATIONS

by

Suman Ghorai

A thesis submitted in partial fulfillment
of the requirements for the Doctor of
Philosophy degree in Chemistry
in the Graduate College of
The University of Iowa

May 2013

Thesis Supervisor: Assistant Professor Alexei V. Tivanski

Graduate College
The University of Iowa
Iowa City, Iowa

CERTIFICATE OF APPROVAL

PH.D. THESIS

This is to certify that the Ph.D. thesis of

Suman Ghorai

has been approved by the Examining Committee
for the thesis requirement for the Doctor of Philosophy
degree in Chemistry at the May 2013 graduation.

Thesis Committee: ________________________________
Alexei V. Tivanski, Thesis Supervisor

____
Leonard MacGillivray

____
Sarah Larsen

____
Christopher Cheatum

____
Gregory Carmichael

To my parents Manju and Prabhat Ghorai

A person who never made a mistake never tried anything new.

Albert Einstein

ACKNOWLEDGMENTS

Foremost, I would like to express my sincere respect and gratitude to my advisor Prof. Alexei V. Tivanski for his continuous scientific and moral support throughout my research career. His guidance and deep knowledge has helped me overcome obstacles in my research in numerous occasions. He has not only been a great advisor, he has been an excellent instructor for my teaching assignment. His guidance in research and teaching assignment has been one of the primary causes of my success as a graduate student.

I would like to thank all my committee members Prof. Len MacGillivray, Prof. Sarah Larsen, Prof. Christopher Cheatum and Prof. Gregory Carmichael for their time and valuable suggestions and comments to improve the presentation of my dissertation. I would also like to thank instructors for teaching assignment for making the teaching experience enjoyable rather than a time consuming process. I would like to thank advanced laboratory manager Brian Morrison for his help during teaching assignment.

I would also like to thank Joe Sumrak, Kristin Kester and Dejan-Kresimir Bucar for their cooperation and time for several collaborative projects. Without this help, those projects would not have been successful. I would also like to sincerely thank Dr. Alexander Laskin from Pacific Northwest National Lab (PNNL) for his continuous suggestion and help in multiple collaborative projects. His guidance in those projects provided a great deal of boost towards my dissertation.

All the members of Tivanski Research Group has helped me a lot during my stay in graduate school. I would like to thank Chandana, Lindsay, Zack, Thilini, Holly and Mitch for their numerous help. I would like to extend my gratitude especially to Chandana and Lindsay. Chandana has taught me a lot about the research while I was beginning my research. Lindsay and I worked together for last four years before she graduated last summer. Without their contribution, this whole journey would not have been so enjoyable.

My stay at University of Iowa was an enjoyable journey due to many of my friends. I would like to thank my closest friends Abhinaba, Pradeep, Nirmal, Oishik, Aashay, Biswanath, Nisarga and Sanmitra. I would also like to thank Bhakti, Varsha, Sai for this enjoyable journey.

Most importantly, I would like to thank my parents Manju and Prabhat Ghorai along with my sister Tanushree for their support and encouragement throughout the whole life and letting me pursue my dream of going to graduate school. Last but not the Least I would like to thank my fiancé Sangeeta for her continuous support when things were not working ideally. Her mental support has endlessly helped me overcoming hardships in several occasions.

TABLE OF CONTENTS

LIST OF TABLES

LIST OF FIGURES

CHAPTER 1

INTRODUCTION

1.1 Contribution of atmospheric aerosols towards total radiative forcing

One of the major warnings in recent years is the increasing amount of Greenhouse gases present in the atmosphere.[1-3] Carbon dioxide, water vapor, other polyatomic molecules in the atmosphere absorb thermal infrared radiation emitted from the Earth surface and re-radiate some of this energy back toward the surface.[4-6] This phenomenon is in part responsible for resulting temperature of the planet; without it the average temperature of the planet would be about -19 °C (-2 °F) instead of the actual average temperature, about 15 ° C (59 ° F).[7] This infrared heating of the planet, which is additive to the heating by absorbed solar radiation, is commonly referred to as the "greenhouse effect". In this context, we can presume that quantification of the total radiative flux due to greenhouse effect would allow us to quantitatively explain the climate change over the last century. Unfortunately, the overall effect cannot be described in such a simplistic manner because of the influence of atmospheric aerosols, small suspended particles in the atmosphere.[8-11] These particles influence absorption and scattering of solar radiation,[12,13] formation of cloud condensation nuclei,[14,15] atmospheric reactions,[16] visibility[17] etc. These phenomena reduce the amount of solar radiation that is absorbed by the climate system, and, as concentrations of aerosols have increased over the industrial era, have exerted a cooling influence on Earth's climate system that is confidently believed to have offset some of the warming influence of the incremental greenhouse gases.[18-21] The overall radiative forcing on the earth, reported by Intergovernmental Panel on Climate

Change (IPCC), is shown in Figure 1.1 along with the uncertainty range. (IPCC, 2007) Noticeably, aerosol effects represent most of the negative radiative forcing on the climate. Moreover, the uncertainties of the several aerosol forcings substantially exceed those associated with the greenhouse gases and other forcings. Hence, it is evident that atmospheric effects of aerosols are vaguely understood at present. Therefore, we will discuss the overall aerosol effects in the next section.

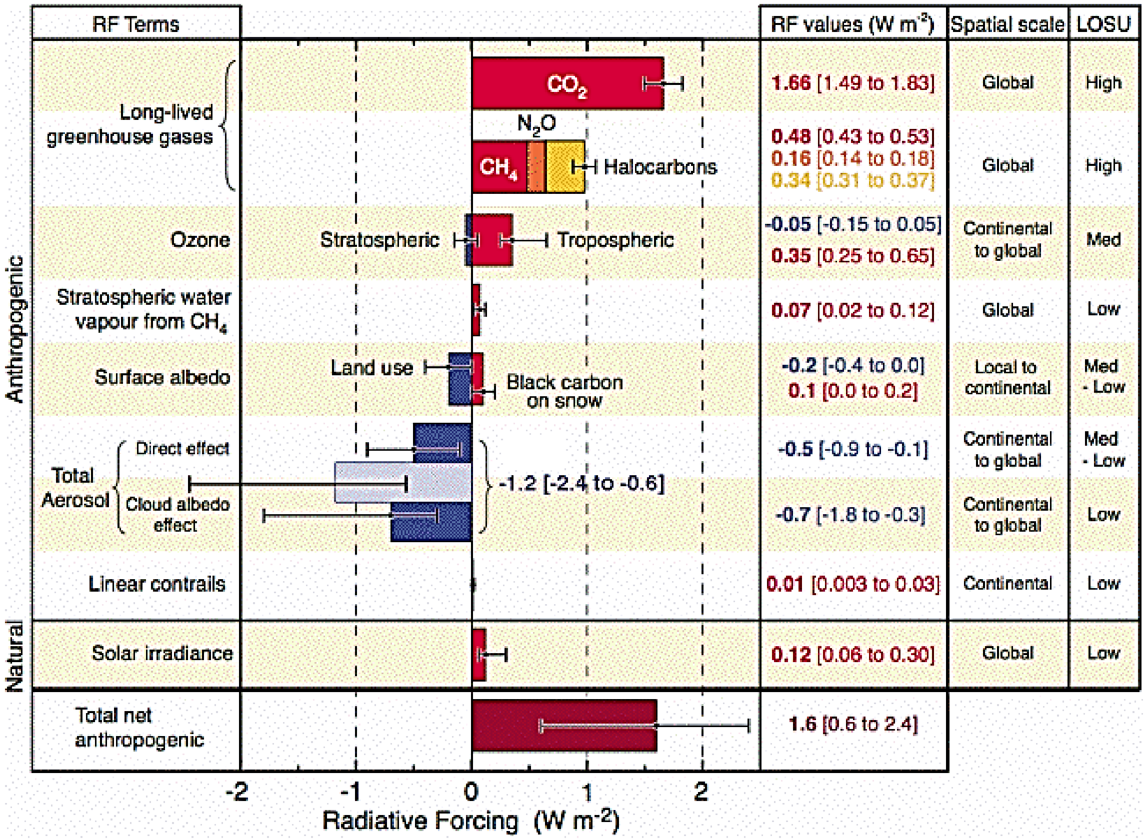

Figure 1.1 Global radiative forcing of climate change in 2005 reported by Intergovernmental panel on Climate Change (IPCC)

1.2 Role of atmospheric aerosols

The overall effect towards radiative forcing due to atmospheric aerosol particles are classified in mainly two categories, namely, direct and indirect aerosol effects.[22-24] The direct aerosol effect accounts for the total radiative forcing due to absorption of solar and infrared radiations by these particles; whereas the indirect effect mainly accounts for the effect of aerosol on formation and alteration of the nucleation of cloud condensation nuclei (CCN), influencing the overall cloud optical depth.

The quantification of aerosol radiative forcing is more complex than the quantification of radiative forcing by greenhouse gases because aerosol mass, composition and particle number concentrations are highly variable in space and time.[25,26] This variability is largely due to the much shorter atmospheric lifetime of aerosols compared with the important greenhouse gases.[27,28] The quantification of indirect radiative forcing by aerosols is especially difficult. In addition to the variability in aerosol concentrations, some quite complicated aerosol influences on cloud processes must be accurately modeled. Important parameters are size distribution,[29] change in size,[30] chemical and elemental composition and particle water content with relative humidity (RH),[31] complex refractive index,[32] and solubility of aerosol particles.[33] Therefore, these RH dependent changes in atmospheric particles are one of the most important studies to quantitatively understand total radiative forcing. Hence, an important field of research in recent years has been studies on particle size, composition, density, hygroscopic properties etc. of aerosol particles.

1.3 Hygroscopic properties: climate and health effects

Hygroscopic properties of aerosols are their ability to uptake water as a function of RH. Aerosol particles with unique chemical components exert characteristic hygroscopic properties. Inorganic salts typically show deliquescent behavior, which means that they form liquid droplets as they dissolve at a material-specific deliquescence relative humidity (DRH). Upon decreasing RH, such particles crystallize at an efflorescence relative humidity (ERH). The ERH is typically lower than the DRH, resulting in a hysteresis effect. In contrast, other particles (e.g., malonic acid) grow monotonically with increasing RH and do not show deliquescence or efflorescence.[34]

The hygroscopic properties of ambient aerosols play a major role in numerous areas of the environment ranging from large scale phenomena, such as global climate change, (IPCC report, 2007) to local events,[35] such as the induction of adverse health effects in humans.[36] For example, black carbon (BC) strongly absorbs UV and near infrared radiation and its direct aerosol effect is considered to be a principle contributor towards global warming.[37] To the contrary, BC internally mixed or coated with a hygroscopic species serves as an efficient cloud condensation nuclei (CCN) and hence this indirect aerosol effect leads to an overall cooling effect towards the Earth climate.[38-41] Therefore, water uptake properties of these particles largely control the balance between global warming and cooling effect.[42]

The chemical complexity and uncertainties in production mechanisms of atmospheric aerosol species pose difficulty to access its impact on public health/welfare. These interactions depend not only on composition but also on particle size, which is linked to composition owing to the process of hygroscopic water uptake.[43] The aerosol particles are often found to be a complex mixture of metals and other water soluble species. Metals do not contribute as much as the water-soluble species to the hygroscopic properties of the aerosol. Considering very humid condition of human respiratory tract,[44] the overall hygroscopicity of particles is crucial information to predict where they deposit upon inhalation.[43] For example, report on aerosols collected near a copper smelter in Arizona showed that the maximum concentrations of As, Cd, and Pb in the particle size range of 0.18 - 0.55 μm at 90% RH overlaps with the allowed concentration in human body. Therefore, these aerosols are of special concern from a health perspective, particularly considering their size range.[45]

In addition to above mentioned effects, the aerosol water provides a medium for aqueous-phase chemical reactions that can alter the chemistry and morphology of particles. Hence, hygroscopicity of atmospheric particles can control fate of some chemical reactions in the atmosphere.[34] In addition, particle size increase due to hygroscopic growth has a major influence on the direct radiative forcing of these particles.[34] The hygroscopic behavior, including the exact DRH and ERH values of most atmospherically relevant inorganic salts, is well established.[46] However, the hygroscopic growth of complex mixtures of inorganic and organic matter in ambient particles is difficult to predict from the properties of their individual constituents.[34] Therefore, we will report new methods utilizing Scanning Transmission X-ray Microscopy (STXM), Atomic Force Microscopy (AFM) and micro-FTIR spectroscopy in order to quantify the hygroscopic properties of micro- and nano-dimensional particles with single as well as multiple chemical components.

1.4 Effect of particle density and elemental/chemical composition on climate

The important radiative properties of atmospheric particles (both direct and indirect) are determined at the most fundamental level by the aerosol composition and size distribution.[34] Elemental composition of the atmospheric particles strongly influences scattering and absorption of UV and infrared radiation,[42] hygroscopic properties,[47] complex refractive index etc.[34] For example, UV and infrared absorption of BC is highest compared to other chemical components usually present in the atmosphere.[42] Moreover, their climate effect varies widely with the inclusion (both externally or internally mixed) of sulphate, nitrate etc. Formation of Secondary Organic Aerosol (SOA) and the solubility of organic compounds in aerosols depend largely on the amount of organic oxygen in the sample under examination.[48] Studies on the kinetics of various environmental oxidation and reduction processes have shown that the density and composition of the aerosol controls the kinetics.[49] Hence, we realize the importance of quantifying density and elemental composition of atmospheric particles. Herein, we report a new method to simultaneously quantify the density and elemental composition of sub-micrometer particles. Moreover, a new method was developed that allowed us to calculate spatially resolved density and elemental composition to explore mixing state on a single particle basis.

1.5 Scanning Transmission X-ray Microscopy (STXM)

Scanning transmission X-ray microscopy (STXM) generates microscopic images of a thin section of specimen by raster-scanning in a focused mono-energetic X-ray beam.[50] The flux of transmitted beam is measured to obtain the image intensity. The cartoon in Figure 1.2 explains the basics of STXM. Along with microscopic images, X-ray absorption spectra can also be obtained using this technique. Therefore, this technique falls into the category of 'spectromicroscopy' and applied to study chemical properties of materials along with observing morphology.

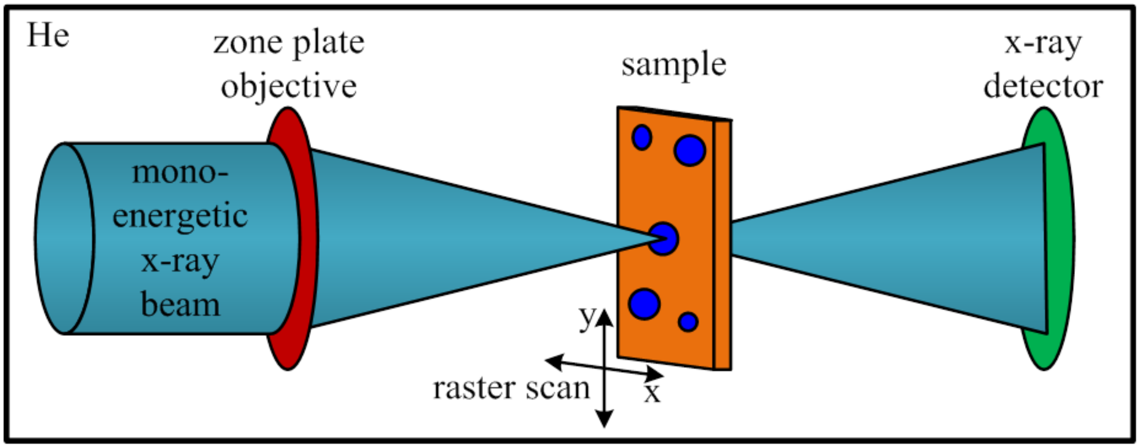

Figure 1.2 Cartoon of STXM showing the data collection mode

The working principle of STXM is near edge X-ray absorption fine structure spectroscopy (NEXAFS).[51,52] NEXAFS spectroscopy measures photoabsorption cross section for excitation or photoionization of tightly bound core electrons. Hence, NEXAFS spectroscopic transitions are used as a chemically sensitive image contrast mechanism. These spectra are atom specific as each element has a characteristic core binding energy (i.e. Carbon 1s: ~290 eV, Nitrogen 1s: ~400 eV, and Oxygen 1s: ~530 eV).[53] The spectral feature corresponds to transitions from ground state to core excited states. Therefore, depending on the specific transitions to the core excited state, we can obtain functional group information. For example, Carbon 1s NEXAFS spectrum of poly(styrene-r-acrylonitrile) is dominated by intense transitions at 285 eV and 287 eV corresponding to C 1s to π* transitions for phenyl and acrylonitrile group.[54,55] Therefore, we have used this spectroscopy for characterization of several organic and inorganic materials in my work.

STXM, being a transmission mode spectromicroscopic technique, is primarily used to obtain images of fine particles. As the signal in the image is directly proportional to type of element present at a particular X-ray energy, STXM is popularly used for spatially resolved chemical mapping of micrometer dimensional particles of complex chemical mixture.[56,57] Depending on the absorption energy range for different elements and that element containing functional groups, absorption edges are defined (C: 280-320 eV; N: 390-420 eV; O: 525-550 eV).[31,58] Single energy images can be obtained at any particular energy in the absorption edge. The beginning and the end of the absorption edge is defined as preedge and postedge.[31,58] For example, preedge and postedge for carbon is 280 and 320 eV, respectively. The pre-edge background arises from the combined absorption of other elements at that energy.[58] The C postedge absorbance depends on the number of C atoms. Therefore, subtracting the preedge image from the postedge generates an image, which shows the intensity solely due to the presence of the carbon containing functional group in the sample. This type of imaging is called total absorbance map.[31] Taking advantage of the total absorbance map in different (C, N, O) absorption edges, we have developed several unique methodologies to quantify physical properties such as hygroscopic properties, elemental composition, density, mixing state of micrometer dimensional particles on a single particle basis.

1.6 Organic materials in electronics and photovoltaics

Organic materials have attracted significant attention in recent decades, resulting in rapid development of organic devices.[59,60] Basic advantages in using organic materials lie in their unique properties such as their chemical versatility, purity, long range ordered structure, easier control of electrical, mechanical and optical properties by tuning chemical functionality.[61-64] In particular, micro- and nanoscale organic crystals have been widely used in designing flexible devices. Recent studies using functionalized TTF (tetrathiafulvalene) showed fabrication of single crystal organic circuits that function with high performance and extremely low power consumption.[61] In other studies semiconducting organic crystals are used to design OFETs,[65-67] whereas most popular use of organic crystals was observed in OLED display technology.[68-70] Photolithography in organic thin film has been performed for its applications as photoresist materials[71,72] and used in solar cells.[73-75] Applicability of these materials depends largely on the structure-property relationship.[61] For example, highly conjugated molecules with strong conjugation with the neighboring molecules often results in high mobility values. Therefore, development of new materials and characterizing their electrical,[76] mechanical[64] and optical[77,78] properties has been popularly studied by researchers in recent years.

1.7 Solid state single-crystal-to-single-crystal (SCSC) reaction in cocrystals and its applications

Single-crystal-to-single-crystal (SCSC) reactions are defined as the class of solid state reaction of a single crystal to form the product without any changes in crystal integrity.[79,80] Although this phenomenon has been rarely observed where the crystal remains virtually unchanged after the solid state reaction, several examples of this type has been reported for cocrystals in the literature.[64,81] The cocrystals are defined as a multicomponent crystal in which all components are solid under ambient conditions when they are in pure form;[82] these components co-exist as a stoichiometric ratio of target molecule and a molecular cocrystal former. Cocrystals are an exciting group of material as the composition of the matter and chemical/physical properties of a molecular species can be modified without any changes in covalent bonding.[82-84]

Cocrystals has been utilized in several applications in pharmaceutical science,[82] data storage devices[85] and molecular switches[86] etc. For example, the diversity in pharmaceutical cocrystals provides exciting opportunity to design novel and improved forms of active pharmaceutical ingredients (APIs).[82] For example, carbamazepine (CBZ) are popularly used in anti-epileptic drug Tegretol® for decades and its physical stability has been significantly improved by forming CBZ : saccharin cocrystals.[87,88] Cocrystals of fluoxetine hydrochloride (Prozac®) with benzoic, succinic and fumaric acid showed significant changes in aqueous dissolution rate of the drug.[89] Therefore, cocrystals of APIs bring about intriguing modification in their physicochemical properties and hence popularly applied in pharmaceutical industry. Moreover, the simplistic approach of solid state synthesis provides an added dimension to their applicability.[82]

Use of SCSC reactivity in device applications has also been well documented in data storage device and photoactivated molecular switch.[85,86] Cycloaddition reactivity of photochromic compounds such as diarylethenes in solid state has been reported to dramatically augment the memory density in data storage devices as compared to the conventional materials.[90] Therefore, these materials are considered among the most promising materials for the future of data storage devices.[90] In addition, *Li et al* reported a successful design and synthesis of a fluorescent switch material system by utilizing photochemical reactivity of diarylethylene.[91] Herein, it is worthwhile to mention that [2+2] photocycloaddition and photocycloreversion is photo-allowed and thermo-forbidden reaction, making the molecular switch system thermally stable.[91]

1.8 SCSC reactivity and mechanical properties

Due to the structural changes during a solid state photoreaction, large strain energy generates within the crystal, leading to the possibility of crystal cracking.[92,93] Hence, effective stress and strain relaxation within the crystal network is necessary for a SCSC reaction to occur.[64,94] On the other hand, stress and strain is inherently related with the mechanical properties of the materials. Therefore, we have studied the changes in mechanical properties in a SCSC reaction involving [2+2] cycloaddition reaction of 5-CN-resorcinol and trans-1,2-bis(4-pyridyl)ethylene (4,4'-bpe).[64] In order to understand the dependence of SCSC reactivity on mechanical properties of the material, we need to explore structure property relationship of several other cocrystal systems which can undergo similar [2+2] cycloaddition reaction. In this report, we show mechanical changes involved in several other cocrystals involving 4,4'-bpe. The ultimate goal of these measurements is to establish a relation of structure and SCSC reactivity with mechanical properties of the cocrystal.

1.9 Conclusions

Realizing the importance of the effect of aerosol particles in the atmospheric, we have designed several novel methodologies to accurately quantify their physicochemical properties. Hygroscopic properties, elemental composition and density, study of atmospheric tautomerism reaction has been perform taking advantage of unique and powerful spectromicroscopic techniques, such as STXM, micro-IR, AFM and Scanning Electron Microscopy (SEM). The ability of STXM to obtain chemical information along with a sufficient spatial resolution enables us studying single particle hygroscopic properties along with spatially resolved density and elemental composition. The direct applicability of these studies has been realized in this work in the context of environmental fate of atmospheric particles.

Importance of unique physical properties of nanocrystalline organic materials has been realized in the context of device application. AFM nanoindentation technique was used to study mechanical properties of organic nanocrystals. Mechanical changes associated with SCSC reactivity of these materials were examined. Moreover, structure and mechanical property correlation has been established by introducing structural changes in the nanomaterials. Furthermore, the potential device application ability of these nanocrystals is demonstrated by forming thin films of these materials. Photolithography on the thin film showed its potential application as a photoresist.

CHAPTER 2

HYGROSCOPIC BEHAVIOR OF INDIVIDUAL SUB-MICROMETER PARTICLES STUDIES BY X-RAY SPECTROMICROSCOPY

2.1 Introduction

Airborne particles from various natural and anthropogenic sources have significant effects on the atmospheric chemistry,[95-97] climate,[98] and air quality.[99] The climate effects are classified as direct and indirect aerosol effects.[100,101] The direct effect corresponds to the net radiative flux in the atmosphere caused by the modulation of light scattering and absorption by alteration in concentration and optical properties of aerosols. The indirect effect accounts for the changes in net radiative transfer in the atmosphere caused by the modulation of cloud properties due to changes in the concentration of cloud condensation nuclei, CCN.[100,102] Both effects depend on particle shape, size, phase, chemical composition, mixing state, and particle water content,[103-108] all of which may strongly depend on relative humidity (RH).[109] Thus, as atmospheric humidity fluctuates, airborne particles can experience humidity-dependent changes in the particle size, phase, concentration, and even chemical composition.[110-112] Such changes cause both positive and negative effects on the interplay between the direct and indirect aerosol effects, making overall prediction of the radiative forcing difficult.[113,114] Therefore, studies focusing on the changes in the chemical composition or reactivity of aerosols as a function of relative humidity are important, especially on a single particle level.[115-118] Studies that focus on individual particles allow one to not only determine an ensemble-averaged response but also probe how, for example, particle size and shape influences the hygroscopic properties. The size-dependent chemical and hygroscopic properties become especially noteworthy for fine (submicrometer) atmospheric aerosols.[119,120] Therefore, development of analytical methods for quantitative measurements of hygroscopic and chemical properties of individual submicrometer particles is critical for better understanding of their environmental effects.

Hygroscopic properties of aerosols are typically defined by two phase transitions, deliquescence and efflorescence, and the extent of hygroscopic growth as a function of RH. Deliquescence is a phase transition from the solid to liquid state due to rapid absorption of water, while efflorescence is the reverse transition from the liquid to solid state that is accompanied by a spontaneous release of water. These transitions occur at a characteristic relative humidity, specific of a particular particle composition and size. The relative humidity at which deliquescence and efflorescence occur are defined as deliquescence relative humidity (DRH) and efflorescence relative humidity (ERH), respectively. DRH and ERH values have been established for many atmospherically relevant submicrometer inorganic particles.[34,46,121,122] However, changes in the chemical properties and mixing states as a function of relative humidity are yet to be studied extensively, especially for aerosols consisting of a mixture of organic and inorganic compounds. Different microscopy and spectromicroscopy techniques have been used to study the hygroscopic properties of atmospheric particles. For instance, environmental scanning electron microscopy (ESEM) has been utilized to study hygroscopic properties and changes in morphology of NaNO3 particles and their implications for aged sea salt aerosols.[123] Environmental transmission electron microscopy (ETEM) was used to observe the hygroscopic and morphological changes of laboratory generated sodium chloride particles by imaging the same particles at increasing relative humidity.[124] Both techniques provide a direct way to determine the DRH and ERH on a single particle basis but cannot be used to quantify the extent of water uptake. On the other hand, uptake of water by laboratory generated micrometer-sized NaCl, sea salt, $NaNO_3$, and $(NH4)_2SO_4$ particles have been quantified using micro-FT-IR spectroscopy,[125] which determines ensemble-average hygroscopic properties but does not permit measurements on a single particle basis nor provides imaging resolution capable of resolving submicrometer particles. Additionally, several other techniques including tandem differential mobility analysis and electrodynamic balance and micro-Raman spectroscopy have been used to quantify hygroscopic properties on a single particle basis, but similar to micro-FT-IR, the spatial resolution is not sufficient to resolve submicrometer particles.[126-129]

Another aspect of the aerosol research is to examine changes in the optical and chemical properties as a function of relative humidity. For example, a combination of particle soot absorption photometer, photoacoustic spectrometer, and scanning mobility particle analyzer techniques was used to characterize the optical and physical properties of aerosols in the Amazon Basin during biomass burning season.[130] Moreover, the partial crystallization and deliquescence of mixed ammonium sulfate and dicaboxylic acid particles was studied during water uptake and evaporation using a combination of elastic light scattering and Raman spectroscopy.[131] Overall, while numerous techniques exist that permit either qualitative or quantitative determination of the hygroscopic properties of particles, there is no experimental approach available until now that allows quantitative characterization of the spatially resolved hygroscopic and chemical properties of individual submicrometer particles as a function of relative humidity.

Scanning transmission X-ray microscopy (STXM) is a unique spectromicroscopic technique that can provide spatially resolved information on the physical, morphological, and chemical properties of individual particles as a function of relative humidity.[132,133] STXM provides a unique opportunity to investigate the spatial resolution (~25 nm) of carbon, nitrogen, and oxygen atom containing functional groups of different environmental samples by means of near edge X-ray absorption fine structure (NEXAFS) spectroscopy. NEXAFS spectroscopy probes an excitation of core electrons by soft X-rays into unoccupied valence orbitals and provides element-specific functional group information.[134] STXM has been used to determine chemical speciation of environmental particles such as biomass burn tarballs,[58] marine particles,[135] and particles collected in urban areas of Mexico City.[136] In addition, STXM has been also utilized to study the nighttime chemical evolution of particles from coal-fired power plant plume[137] and probe oxidation state and morphology of iron-containing particles from various field campaigns.[138]

In this work, we present a novel application of STXM/NEXAFS that allows quantitative analysis of physical, chemical, and hygroscopic properties of individual submicrometer particles. The approach is developed to measure the water-to-solute ratios of individual submicrometer particles. The approach utilizes quantitative X-ray absorption measurements in the presence of water vapor. In the present paper, we report single particle hygroscopic measurements of a series of atmospherically relevant sodium halide and nitrate particles as a function of relative humidity. The samples were selected in part because the hygroscopic properties for some have been previously reported, providing us with an opportunity to validate the developed approach.

2.2 Experimental section

2.2.1 Materials and sample preparation

Particles of NaCl, NaBr, NaI, and $NaNO_3$ were generated using a constant output atomizer (TSI, Inc., model 3076) from aqueous 0.5 M solutions prepared from reagent-plus-grade chemicals (99.99%+ purity, Aldrich). All solutions were prepared with deionized water (18 $M\Omega \cdot$ cm). The generated particles were dried down to ~30% RH in a diffusion dryer (TSI, Inc., model 3062) prior to sizing and substrate deposition using a micro-orifice uniform deposit impactor (MOUDI) (MSP, Inc., model 110). Particles were deposited on Si_3N_4 windows (Silson Ltd., England) mounted on the impaction plate of the seventh stage. The aerodynamic cutoff size of the seventh stage is 0.56 μm. All samples were prepared at room temperature and used within a couple of days after the preparation.

2.2.2 Scanning Transmission X-ray Microscopy (STXM)

Single energy images and oxygen (O) K-edge near edge X-ray absorption fine structure (NEXAFS) spectra were acquired using a STXM instrument on beamline 5.3.2 of the Advanced Light Source at Lawrence Berkeley National Laboratory (Berkeley, CA). For STXM measurements, the X-ray beam is focused with a custom made Fresnel zone plate onto the sample, and the transmitted light intensity is detected. The diffraction limited spot size at the sample was ~25 nm for these experiments. Images at a single energy are obtained by raster-scanning the sample at the focal plane of X-rays and collecting transmitted monochromatic light as a function of sample position. Spectra at each image pixel or a particular sample region are extracted from a collection of images recorded at multiple photon energies across the absorption edge. Dwell times used to acquire an image at single photon energy were typically 0.5 ms per pixel. To quantify the absorbance signal, the measured transmitted intensity (I) is converted to optical density (OD) using the Beer-Lambert's law:[139] OD = ln (I/I_0) = $\mu \rho d$, where I_0 is the incident photon flux intensity, d is the sample thickness, and μ and F are the mass absorption coefficient and density of the sample material, respectively. Incident beam intensity is measured through the area of substrate free of particles. The particle spectrum is obtained by averaging the absorbance signal over the particle projection area on the substrate. The X-ray energy calibration (accuracy of ±0.05 eV) is performed using addition of CO_2 gas (6 Torr) to the STXM chamber and through comparison of the position of CO_2 Rydberg transitions at 292.74 and 294.96 eV.[140]

NEXAFS spectral features arise from electronic resonance transitions of core electrons specific to different bonding of elements (e.g., different functional groups) and involve both 1s to π^* and/or 1s to σ^* transitions. Peaks arising due to σ^* transitions are usually broader than for π^* transitions and superimposed on the photoionization continuum. Spectra from 1s electrons for O atoms are in the energy region of 525-550 eV. The pre-edge background arises from the combined absorption of other elements at that energy. The O postedge absorbance depends on the number of O atoms. The total O absorbance is defined as the difference between the O postedge absorbance at 550 eV and the O pre-edge absorbance at 525 eV. The total O absorbance is directly proportional to the number of oxygen atoms inside a particle and can be used as a direct measure of oxygen concentration.[58] In the present study, the total O absorbance is used to quantify the amount of O atoms present in the particle at various relative humidity (RH).

STXM experiments at different RH were afforded by sequentially adding controlled amounts of water vapor into the STXM chamber from a stainless bulb containing room temperature deionized water (18 MΩ· cm). Prior to addition of water vapor, the chamber was evacuated to a pressure of 80 mtorr. The amount of water vapor added to the STXM chamber was regulated using a mechanical leak valve and measured using a capacitance manometer. Water vapor pressure range used here is between 0.1 and 22 Torr. The temperature inside the chamber was around 26 °C, and the saturated equilibrium water vapor pressure at this temperature is 25.2 Torr.[141] The RH was calculated by dividing the corresponding water vapor pressure by the saturation vapor pressure. After each change of water vapor pressure in the system and prior to the STXM measurements at a particular RH, a typical delay time of approximately 5 min was necessary to obtain stable and reproducible STXM images and single particle NEXAFS spectra.

2.3 Results and discussion

The work is organized in the following way. We first report STXM measurements in the presence of water vapor utilized to establish the maximum RH that can be used without limiting quantitative nature of the X-ray absorbance measurements. Second, we present the experimental approach used to obtain spatially resolved water uptake measurements on individual submicrometer particles. Next, we describe a model developed for quantifying mass of water within an individual particle and demonstrate model application for particle standards with known hygroscopic properties: NaCl, NaBr, NaI, and $NaNO_3$ particles. Finally, we present the NEXAFS spectra of deliquesced particles that provide important information on chemical environment of the content.

Specifically, we present spectroscopic evidence of the halide-water complex formation in deliquesced particles that can alter their optical properties and influence the atmospheric halogen cycle.

2.3.1 STXM/NEXAFS measurement with water vapor

The first set of experiments was conducted to determine the range of RH at which STXM can operate and provide quantitative X-ray absorbance measurements. Addition of water vapor to the STXM chamber provides a number of light absorbing gas phase water molecules in the path of the X-ray beam that can attenuate the intensity of transmitted light and, thus, contribute to the measured absorbance signal. To determine the absorbance due to the presence of water vapor, O K-edge NEXAFS spectra were acquired at different RH through a sample-free Si_3N_4 substrate. Figure 2.1a shows the O K-edge NEXAFS spectra at five selected RH. Here, only a narrower spectral range out of the measured energy range between 525 and 550 eV is shown to better visualize the main resonance transitions of water. For all spectra, the corresponding constant linear pre-edge background signal (525 eV) was subtracted to remove the absorbance due to the Si_3N_4 substrate. Therefore, the background-subtracted spectra provide a direct way to measure the amount of water present inside the chamber. As expected, the absorbance is increasing at higher RH.

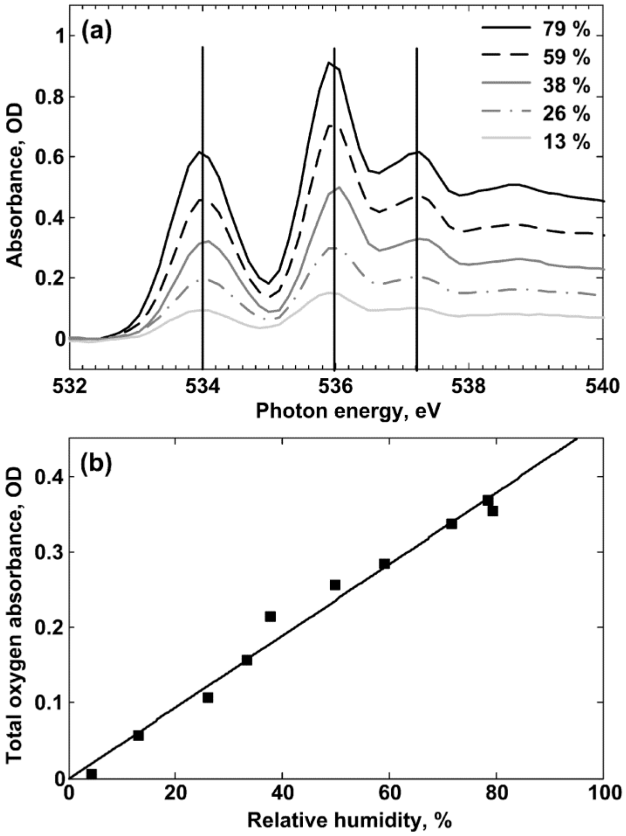

Figure 2.1 (a) NEXAFS oxygen K-edge spectra of water vapor in STXM chamber at different RH values. Vertical lines indicate three main electronic transitions at 534, 536, and 537.2 eV. (b) Total O absorbance (550-525 eV) of water vapor is plotted as a function of RH. Triangles are the measured absorbances, and the solid line is a linear fit with zero intercept. The linear dependence confirms the applicability of the Beer-Lambert's law within the studied RH range (~2-90%).

The water vapor spectra have three main sharp transitions at 534, 536, and 537.2 eV, as indicated by vertical lines in Figure 2.1a. The spectral profile and transition energies observed here are in excellent agreement with the literature.[142-144] In particular, the peak at 534 eV corresponds to 1s to $4a_1$ transition,[142-144] the peak at 536 eV is the 1s to $2b_2$ transition,[142-144] and the peak at 537.2 eV accounts for the 1s to $3pb_1/3pa_1$ Rydberg transition.[145] According to the Beer-Lambert's law, the total O absorbance (550-525 eV) should be directly proportional to the number of gas phase water molecules. Thus, a linear relationship is expected between the total O absorbance and the corresponding RH. Figure 2.1b shows the plot of the total O absorbance of gas phase water molecules as a function of RH, and the solid line shows the best linear fit with zero intercept ($R^2 = 0.98$). The observed linear correlation indicates that the Beer-Lambert's law is applicable between the ~2% and 90% humidity range, and the amount of gas phase water molecules can be quantified on the basis of these measurements.

2.3.2 Spatially resolved water uptake measurement

For these experiments, single energy STXM images are first acquired prior to adding water vapor to locate an individual particle or a collection of individual particles deposited on a Si_3N^4 substrate. Once a particle is located, transmitted intensity images over the same sample region that include the particle is collected at the O pre-edge (525 eV) and postedge (550 eV) energies. The images are next converted to the corresponding absorbance images in the optical density (OD) units. Finally, by subtracting the OD preedge image from OD postedge image, the O absorbance map is generated. The O map provides spatially resolved (~25 nm) information on the concentration of O atoms detected within a region of interest. Subsequently, a controlled amount of water vapor is added until a desired RH is reached. After allowing the system to equilibrate for at least 5 min, new O pre-edge and postedge single energy STXM images are collected over the same sample region and then converted to the O map. The experiment is repeated at increased RH until a desired maximum value is reached. The combined results provide a series of quantitative O maps at various RH collected over either the same particle or an ensemble of particles. This completes the hydration part of the experimental cycle. The dehydration part is obtained by gradually decreasing the water vapor pressure in the

STXM chamber. Ultimately, the combination of hydration and dehydration paths generates a full hydration/dehydration cycle that includes a series of spatially resolved single energy O pre-edge and postedge absorbance images and O absorbance maps at various RH obtained over the same individual particle or a collection of particles.

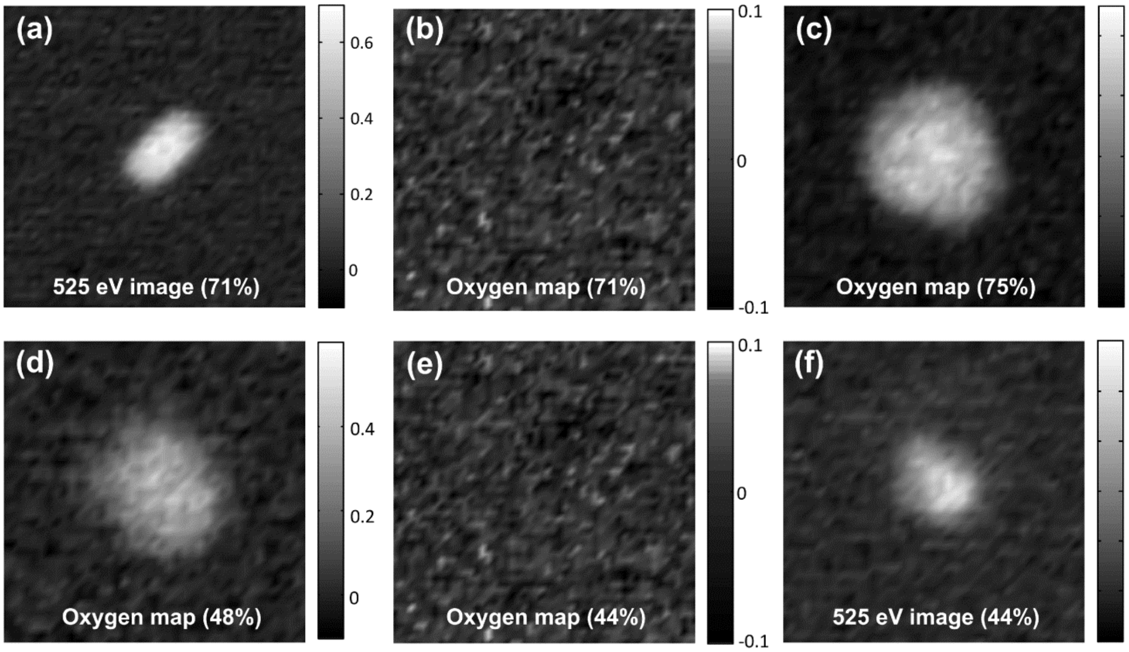

Figure 2.2 Typical sequence of STXM absorbance maps (2 μm × 2 μm, OD units) collected during the hydration/dehydration cycle over the same NaCl particle. (a) O pre-edge (525 eV) map of the particle at 71% RH (below DRH) and (b) corresponding O map (550 eV - 525 eV) showing absence of O within the particle. (c) O map immediately after 75% DRH. (d) O map before the 48% ERH and during the dehydration path. (e) O map at 44% after efflorescence displaying zero absorption by O and (f) corresponding O pre-edge map.

Figure 2.2a-f illustrates this approach with a series of selected single energy absorbance images and O absorbance maps obtained by monitoring changes in the size and total O absorbance of an individual NaCl particle deposited on a Si_3N_4 substrate. The hydration/dehydration cycle was performed between ~2% and 90% RH. All images shown in Figure 2 have the same size of 2 μm × 2 μm and were collected over the same particle. The color bars indicate changes in the absorbance in OD units where the lighter color corresponds to particle regions with higher absorbance. No changes in the particle shape, size, or total O absorbance were detected until the deliquescence RH was reached. Figure 2.2a shows an O pre-edge (525 eV) absorbance map of the particle at 71% RH prior to deliquescence. The particle has crystalline prism morphology with a base size of approximately 550 nm × 900 nm. The O map at this RH is shown in Figure 2b and indicates zero oxygen absorbance (<0.02 OD) in the particle, confirming the absence of water inside the particle. Figure 2.2c shows O map of the particle at 75% RH, collected immediately after the deliquescence phase transition. A drastic change in the particle size and shape, as well as a significant increase in the total O absorbance is observed. Specifically, particle shape has changed from the prism morphology to a rounded shape with a geometrical mean diameter of approximately 1.6 μm. The maximum total O absorbance determined at a center of the particle has increased from 0 to 0.65 OD. These observations clearly imply the deliquescence has occurred and the crystalline NaCl particle transformed into the microdimensional droplet at DRH 73 ± 2%.

During the dehydration path, a decrease in RH led to a continuous decrease in the particle size and the total O absorbance until the efflorescence relative humidity (ERH) of 46 ± 2% was reached. At the ERH, reverse phase transition has occurred and the particle returns to the original solid state. Figure 2.2d,e shows O maps before (panel d, 48% RH) and immediately after (panel e, 44% RH) efflorescence. At 48% RH, the maximum total O absorbance is 0.35 OD and the particle size is approximately 1.3 μm. Immediately after the ERH, the maximum total O absorbance of the particle decreased to zero (<0.02 OD).

(Figure 2.2e) The zero total O absorbance implies the particle is fully dehydrated and does not retain water after efflorescence. Figure 2.2f shows an O pre-edge (525 eV) map of the particle at this RH where a clear change in the particle size and shape is observed with the particle becoming irregular with the base size of approximately 1 μm × 0.7 μm. Further decreases in the RH until ∼2% did not lead to observable changes in the size and O absorbance of the particle, as expected.

It is worthwhile to comment on the O absorbance sensitivity of the STXM measurement. The change in the particle size during the dehydration path between 75% and 48% RH is relatively small (1.6 versus 1.3 μm). On the other hand, the maximum total O absorbance decreased from 0.65 OD at 75% RH to 0.35 OD at 48% RH. The fact that the relative change in the total O absorbance between these two RH values is ∼50% while the change in the size is only 19% clearly indicates a superior STXM detection sensitivity as compared to other microscopy techniques, such as ESEM or ETEM.[123,125,146] For the later two, direct determination of the water-to-solute ratio is not possible and RH-dependent changes in the cross-sectional size are used instead to estimate the hygroscopic response.[147] In the next section, we present an analytical approach we developed to quantify changes in the particle size and the amount of water uptake during the hydration/dehydration cycle and how it can be used to accurately determine the mass of water and water-to-solute ratio within an individual particle at various values of RH.

2.3.3 Quantifying mass of water on a single particle basis

To determine the mass of water quantitatively on a single particle basis, we employ an averaged cross sectional analysis of the O maps collected at different RH over the particle. A typical O map of the deliquesced NaCl particle (80% RH) is shown in Figure 2.3a, where vertical lines indicate the map region selected to obtain the averaged vertical cross-sectional profile shown in Figure 2.3b. The profile averages all horizontal image pixels absorbances for a particular vertical coordinate resulting in a single averaged absorbance value for this coordinate. From the profile, the vertical full width at the half-maximum (fwhm, Δy) and the maximum averaged O absorbance (OD_{max}) are recorded. Similarly, the averaged horizontal cross-sectional profile is used to determine the horizontal fwhm (Δx) and the maximum averaged total O absorbance. The maximum averaged values of total O absorbance obtained from the horizontal and vertical cross sections are similar, and the average of two is used. As will be described below, the similarity in the absorbance values is expected. In a case when the particle is elongated, the horizontal and vertical cross sections are performed along the two main axis of the particle. Overall, for each particular RH, the data analysis results in recording the horizontal and vertical fwhm along with the maximum averaged total O absorbance.

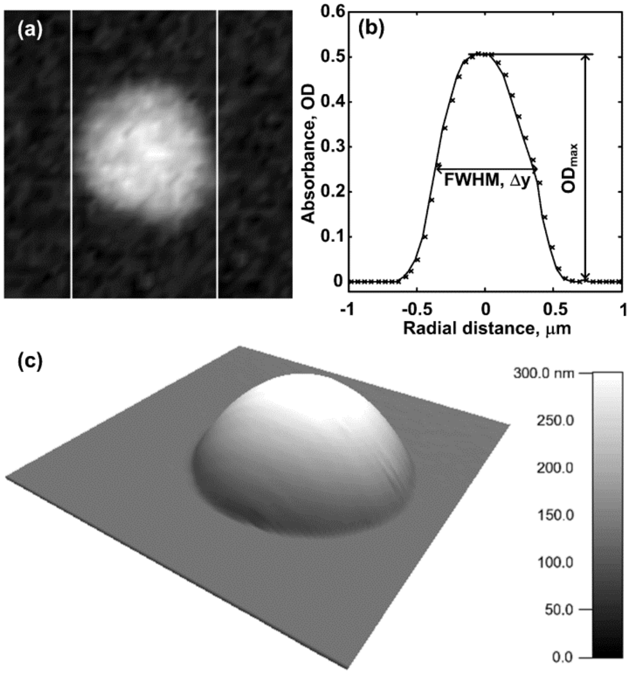

Figure 2.3(a) Typical O absorbance map (2 μm × 2 μm) of a deliquesced NaCl particle (80% RH). White vertical lines indicate the map region selected to obtain the averaged vertical cross-sectional profile shown in (b). The profile is used to determine the vertical fwhm (Δy) and the maximum total O absorbance (ODmax). (c) Representative AFM height image (2 μm × 2 μm) of a similar size deliquesced NaCl particle (80% RH) showing a half-ellipsoidal shape with the particle height approximately three times smaller than the diameter.

In order to relate the cross-sectional measurements described above to the O mass determination, two main assumptions were used: particle shape is a half-ellipsoid and water inside the particle is homogeneously distributed within the particle. Both assumptions can be justified as follows. Since STXM cannot differentiate particles with the half and full ellipsoidal shape, complementary single particle atomic force microscopy (AFM) measurements were performed on the same samples that were studied with STXM. A representative AFM height image of a NaCl particle after deliquescence (80%) is shown in Figure 2.3c. The observed shape is indeed a half-ellipsoid with the particle height approximately three times smaller than the diameter. Similar measurements were also performed for NaBr, NaI, and $NaNO_3$ particles; all displayed half-ellipsoidal shapes, therefore justifying the shape assumption above. The second assumption can be directly inferred from the spatially resolved O maps. Since homogeneous distributions (~25 nm resolution) of O atoms within the particles were observed for all samples (NaCl, NaBr, NaI, and $NaNO_3$), the water molecules are indeed uniformly distributed within the particle. We note that these assumptions may not be applicable in some cases, however, and more sophisticated models may be required. These may include other particle shapes and include factors that account for possible inhomogeneity of water within and around the particle.

A brief description of the model and corresponding derivations is presented here. On the basis of the equation of a standard axis-aligned half-ellipsoid in a *xyz*-Cartesian coordinate system, the averaged vertical cross-sectional height $<z_{ver}(y)>$ as a function of vertical coordinate *y* can be determined from the following equation:

$$\langle z_{ver}(y)\rangle = \frac{1}{4p}\int_{-p}^{p} c\sqrt{\left(1-\frac{x^2}{a^2}-\frac{y^2}{b^2}\right)}\,dx\,, p = \frac{a}{b}\sqrt{b^2-y^2} \ldots\ldots\ldots\ldots\ldots\ldots (1)$$

where *a* and *b* are the equatorial radii of the half-ellipsoid along the horizontal (*x*) and vertical (*y*) axis that lie within the substrate plane, and *c* is the polar radius along *z* axis normal to the substrate. From eq 1, the maximum averaged height can be calculated by equaling the *y* coordinate to zero, resulting in the value $<z_{ver}(\max)> = c\pi/2$. An identical result can be obtained for the maximum averaged height using the averaged horizontal cross sectional profile. The maximum averaged height can then be related to the maximum averaged total O absorbance using the Beer-Lambert's law:

$$OD_{max} = \mu\rho\frac{c\pi}{2} \ldots\ldots\ldots\ldots\ldots\ldots\ldots (2)$$

where ρ is the density of O atoms within the particle and μ is the difference in mass absorption coefficients for atomic O between 550 eV and 525 eV. The difference in mass absorption coefficients is calculated from the atomic scattering factors and found to be 1.96×10^4 cm^2/g.[58] The mass of O atoms inside the particle, m_O, is then calculated by multiplying the volume of the half-ellipsoid ($V = (2/3)\pi abc$) to the O density (ρ) determined from Eq. 2, resulting in the following equation for the O mass:

$$m_O = \frac{4}{3}\frac{ab\langle OD_{max}\rangle}{\mu} \ldots\ldots\ldots\ldots\ldots\ldots\ldots\ldots\ldots (3)$$

Again using the half-ellipsoidal particle shape assumption, the equatorial radii a and b can be directly related to the horizontal and vertical FWHM determined from the averaged cross-sectional analysis above, giving rise to $a = \Delta x/\sqrt{3}$ and $b = \Delta y/\sqrt{3}$. Substituting these two parameters to Eq. 3, the mass of O atoms within the particle can be calculated by

$$m_O = \frac{4}{9}\frac{\Delta x \Delta y\langle OD_{max}\rangle}{\mu} \ldots\ldots\ldots\ldots\ldots\ldots\ldots\ldots (4)$$

The model developed here in the final form of eq 4 provides a direct link between the experimentally measured O-edge absorbance and the O mass. To determine the mass of water, scaling by the molecular weights of O and water is performed. If O atoms are present in the molecular formula or there is some amount of water in the particle prior to exposure to water vapor, eq 4 can be used to calculate the initial O mass and then subtract it from the measurements at other RH. We also note a somewhat interesting result that, while STXM measurements alone cannot be used to calculate the density of O nor determine height of the particle, the model nonetheless still allows us to estimate the oxygen mass. The quantitative determination of mass of water within individual particles that this approach uniquely permits is important for visibility and air quality research.[148] In particular, different models are currently used to predict the mass of water in airborne particles using various experimental parameters such as light scattering properties or particle size.[148-150] However, the estimations are not accurate in part due to propagation and amplification of uncertainties when mass is computed.[150] Therefore, a direct way to measure mass of water within a compound of unknown composition is important. Moreover, we present below how the model can be extended to determine water-to-solute ratio within individual particles with known or measured composition. To summarize, the experimental approach developed here provides a direct and accurate analytical method to measure mass of water within a submicrometer particle of unknown composition and also determine water-to-solute ratio for a known composition of fine particles. In the next section, we present our experimental results that validate this model, thus uniquely offering an opportunity to quantify the mass of O or water on a single particle basis.

2.3.4 Hygroscopic properties of individual NaCl, NaBr and NaI and $NaNO_3$ particles

Using the cross-sectional analysis and eq 4 described above, the mass of water within a single particle at various RH during the hydration/dehydration cycle was measured on individual submicrometer NaCl, NaBr, NaI, and $NaNO_3$ particles. These measurements provide a direct way to measure the amount of water in units of mass on a single particle basis. In this paper, a total of ten different individual NaBr, four NaI, three NaCl, and four $NaNO_3$ particles were studied. Particles with the same composition displayed a similar hygroscopic response with obvious variations in the O mass due to differences in the particle sizes. Figure 2.4 shows representative plots of the mass of water as a function of RH for NaCl, NaBr, and NaI particles with sizes of approximately 0.7, 0.6, and 0.5 μm, respectively. Several conclusions are readily available from the data. First, all particles showed zero initial water content, implying the particles are fully dehydrated. Second, clear deliquescence and efflorescence phase transitions were evident by abrupt changes in the mass of water and were observed for all halide particles. Specifically, the DRH values are 73 ± 2%, 45 ± 4%, and 19 ± 4%, while the ERH values are 46 ± 2%, 22 ± 1%, and 10 ± 1% for the NaCl, NaBr, and NaI submicrometer particles, respectively. Measured values for the NaCl and NaBr are in excellent agreement with the previously reported results.[124,125,147] Below, we will present a comparison figure between our measurements for the DRH and ERH and that based on the literature accepted values. We were unable to find the hygroscopic measurements for NaI and would not compare our measurements with the literature. Thus, to the best of our knowledge, the hygroscopic properties of NaI shown in Figure 2.4c were not reported previously. We note the DRH and ERH values systematically decrease for the halide salts with the largest for the NaCl and lowest for NaI. The trend is due to an increase in an anion size from Cl^- to Br^- and then to I^- that corresponds to a decrease in the lattice energy from NaCl to NaBr and then NaI.[151,152] Finally, a close inspection of the dehydration path for the NaI particle after the ERH shows the particle still retains a small amount of water, unlike other halides.

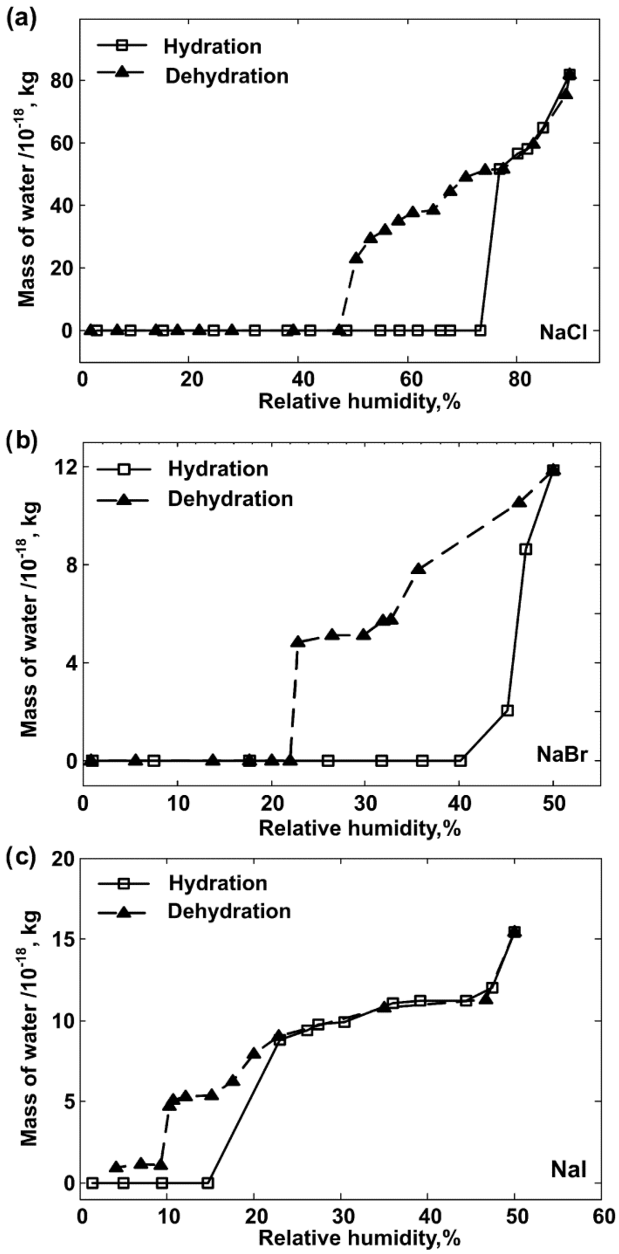

Figure 2.4 Plot of the mass of water during hydration and dehydration cycle as a function of RH for an individual 0.7 μm NaCl particle (a), 0.6 μm NaBr particle (b), and 0.5 μm NaI particle (c).

Since the halides do not contain O atoms, their concentration within a particle cannot be measured directly by STXM. However, using eq 4 and the cross-sectional analysis of the O pre-edge OD image that contains dry particle allows us to determine a normalization factor, defined as an effective mass here, which is directly proportional to the halide concentration within the particle. The effective mass is determined using eq 4 where the maximum averaged optical density is obtained from the O pre-edge map instead of the total O map used for mass of water measurements. The effective mass can then be used as a normalization factor to scale the mass of water. We utilized this scaling approach for all halide particles studied here, and particles with the same composition all displayed a practically identical normalized hygroscopic response (Figure 2.5) with a small deviation that presumably originates from particle to particle variation. This confirms that such scaling can be used to remove the solute concentration contribution to the mass of water measurements and allows, in principle, one to study how the size of the particle influences the hygroscopic properties. The fact that no size variation was observed for these samples is expected since the particles studied here were around 500 nm in size, significantly larger than sizes of up to 60 nm where size-dependent hygroscopic properties were observed.[109]

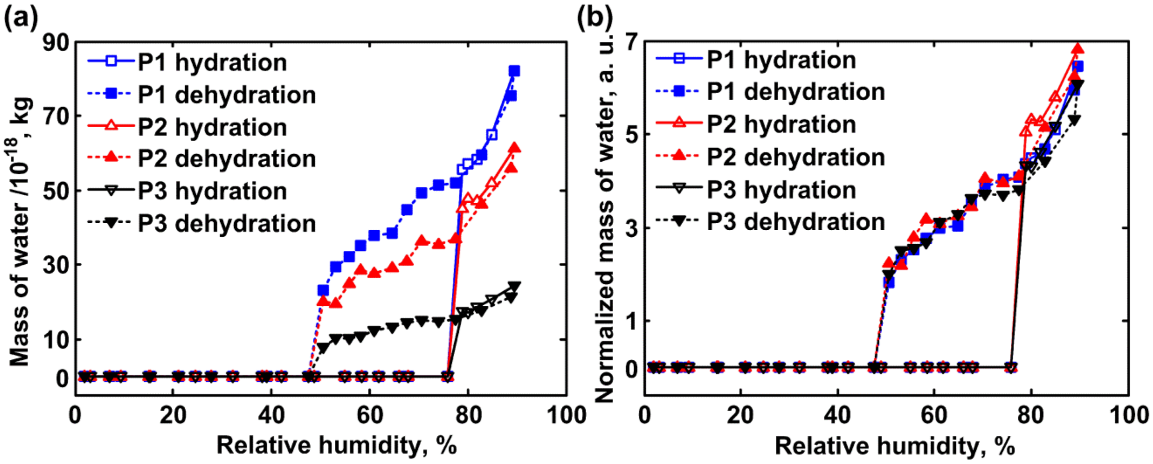

Figure 2.5 Plot of hygroscopic response of three submicron NaCl particles of different sizes as a function of relative humidity with mass of water in absolute scale (a) and normalized by the corresponding effective mass (b) P1, P2, and P3 refers to three different individual NaCl particles.

We next turned to $NaNO_3$ since, unlike the halides, this molecule has three O atoms and, thus, the O absorbance measurements can be used to determine the initial amount of the solute ($NaNO_3$). When the initial number of solute molecules is measured, water-to-solute ratio (WSR) can be determined in addition to the mass of water. Figure 2.6 shows a representative plot of how WSR during the hydration/dehydration cycle depends on RH for an individual $NaNO_3$ particle. The hydration path exhibits deliquescence at around 75% RH, while efflorescence is observed at approximately 35% RH. Both transitions are in close agreement with the previously reported measurements by Tang and Munkelwitz,[153] indicated by the solid line in Figure 2.6. Nearly perfect overlap provides strong evidence that our measurements and model interpretation are accurate and produce results that are in quantitative agreement with the literature data. To further validate our approach, our experimentally determined DRH and ERH values for NaCl, NaBr, and $NaNO_3$ are compared with the available literature data and the comparison plot is shown in Figure 2.7. As can be seen, our results agree very well with the accepted literature values. In summary, results obtained using several laboratory-generated inorganic particles and their excellent agreement with the corresponding results obtained using accepted experimental methods strongly indicate that our methods for the determination of the humidity-dependent mass of water on a single submicrometer particle basis are valid and can be used to obtain accurate and quantitative results. We note the approach developed here not only is limited to atmospherically relevant particles but also can be similarly applied to all types of nano- and micro-dimensional particles where quantitative knowledge of the hygroscopic properties is required.

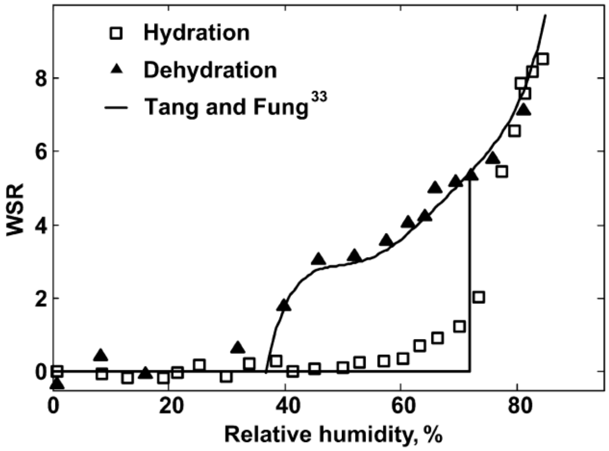

Figure 2.6 WSR during hydration and dehydration as a function of RH for an individual 1 μm $NaNO_3$ particle. The solid line shows the literature result taken from Tang *et al.*[153]

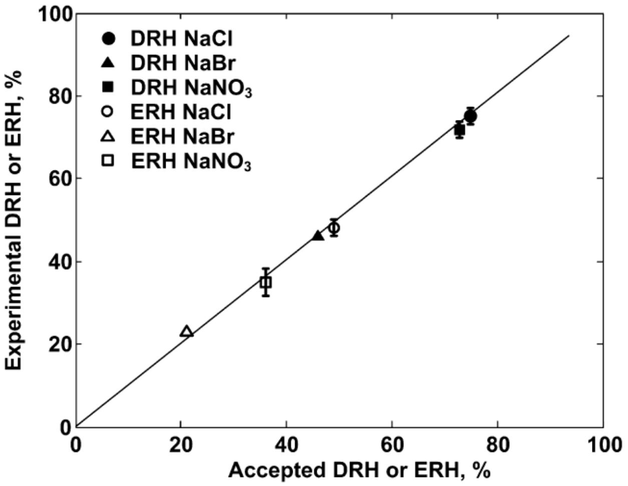

Figure 2.7 Plot of the experimentally determined DRH and ERH values using STXM versus the corresponding literature values for NaCl, NaBr, and NaNO$_3$.

2.3.5 NEXAFS spectra of microdimensional liquid droplets

One of the greatest utilities of STXM is it uniquely allows spatially resolved NEXAFS measurements on an individual submicrometer deliquesced particle. This allows, for example, one to study particles with a complex mixture of multiple components that may be mixed externally and have different solubility. The spatially resolved NEXAFS spectra of individual particles can be acquired to determine how different constituents within the particle respond to water uptake. Here, we report O K-edge NEXAFS spectra of deliquesced NaCl, NaBr, and NaI droplets. All spectra were preedge background subtracted and normalized to the total O absorbance, hence allowing one to compare the relative concentrations of corresponding O-containing functional groups. Figure 2.8a shows liquid phase O K-edge NEXAFS spectra for NaCl, NaBr, and NaI micrometer dimensional liquids at 80%, 50%, and 50% RH, respectively. The same particles were also used for the hygroscopic measurements presented above. In general, spectral features of liquid water are red-shifted relative to the gas phase.[154] All spectra share two well-defined peaks at approximately 535.1 and 537.5 eV that correspond to the σ^* and Rydberg transitions of liquid water, respectively.[144,155] The well-defined and separated Rydberg transitions observed in the gas phase (Figure 2.1a) are transformed to a broad band in liquid phase. It has been reported previously that the ionization potential of oxygen K-shell core electrons shifts to a lower energy region in the liquid state (from 539.9 to 538 eV),[156] consistent with our observations.

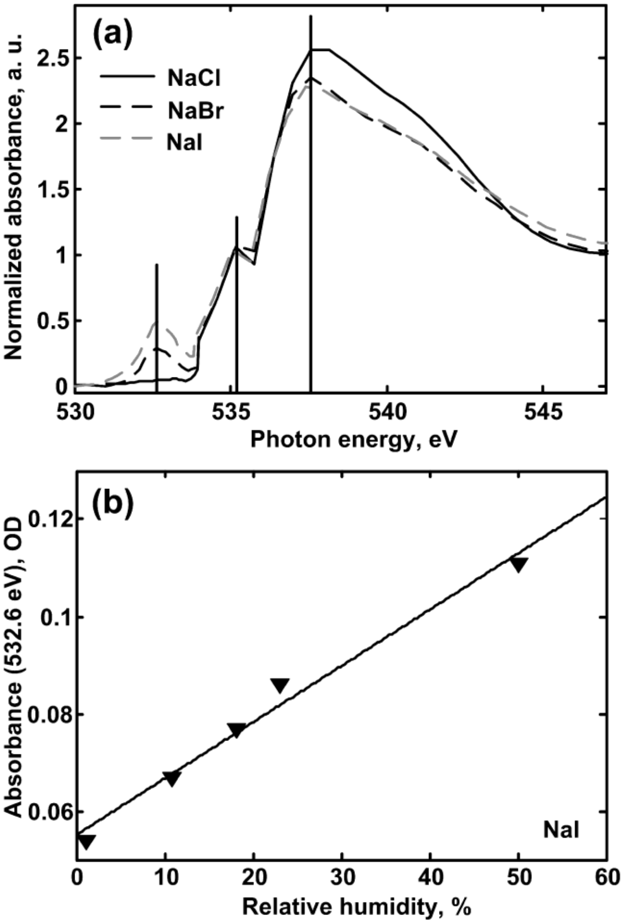

Figure 2.8(a) Normalized O K-edge NEXAFS spectra of a deliquesced individual particle of NaCl (80% RH), NaBr (50% RH), and NaI (50% RH). Spectra were pre-edge subtracted and normalized to the same total O absorbance. Vertical lines indicate three main transitions at 532.6, 535.1, and 537.5 eV. (b) Plot of the absorbance of the peak at 532.6 eV for NaI particle as a function of RH during the hydration/dehydration cycle. Triangles are the measured absorbances, and the solid line is a linear fit. The positive correlation supports the assignment of this transition to the water-halide complex.

In addition to the spectral features of the liquid water, we observe an additional peak at 532.6 eV for the NaBr and NaI droplets which, to the best of our knowledge, was not observed previously. The peak is not present for the sodium chloride, and the normalized intensity of this transition is increasing with an increase in the size of the halide anion. To verify that the observed transition is not due to a possible X-ray damage, experiments were repeated under various extents of X-ray exposure and similar spectra were observed. Additionally, we examined how the absolute absorbance of the peak at 532.6 eV for the NaI droplet changes as a function of RH during the hydration/dehydration cycle (Figure 2.8b). Clear linear correlation between the amount of water present and the peak intensity is observed. On the other hand, no correlation was observed between the intensity of this transition and the degree of X-ray exposure. These observations indicate that the observed peak at 532.6 eV does not originate from the X-ray damage.

According to the molecular dynamics calculations by Cappa et al,[154] a halide-water anionic complex can form in a highly concentrated aqueous halide solution producing a characteristic signature in the energy region similar to where transition at 532.6 eV is observed. The transition was not observed experimentally, however. We, therefore, assign the transition at 532.6 eV to the halide-water anionic complex. We have several additional arguments that justify this assignment. First, we observed that the peak intensity correlates with the RH and, thus, the amount of water within the particle, consistent with the peak assignment. Second, a close inspection of the relative intensities of the 532.6 eV transition and two peaks at 535.1 and 537.5 eV that originate from the non-complexed (free) liquid water[154] clearly show a concurrent decrease in the intensity of the non-complexed water peaks as the size of halide anion increases. This implies the relative concentration of non-complexed water molecules is decreasing between NaCl and NaI as more water molecules participate in the complex formation, thus justifying our assignment. An increase in the size of anion is expected to facilitate the complex formation,[157] and this is exactly what we observe. The absence of the halide-water complex for the NaCl is likely due to the smaller size of the chloride anion and its significantly lower concentration relative to other halides, since NaCl particles uptake significantly more water relative to the NaBr and NaI (see Figure 2.4).

The finding of the water-halide complex formation within micrometer-sized NaBr and NaI particles under atmospherically relevant relative humidity is important as it can affect their optical properties. In particular, a relatively high concentration of the complex can lead to a significant red shift in the UV absorption spectrum of water as the water-water hydrogen bond is weaker than in the water-halide complex. The effect is likely to be especially important at relative humidity slightly above efflorescence, where the lowest WSR (largest halide concentration) in deliquesced particles is expected. In addition, the complex formation can alter the reactivity between the dissolved halide ions and atmospheric ozone gas molecules, potentially leading to a decrease in the number of gas phase bromide and iodide molecules in the atmosphere.[158] Thus, this decrease might affect the atmospheric halogen cycle.[159] Finally, halogens are also used as tracers of igneous processes to monitor magmas from their point of origin through their differentiation and evolution in vapor and escape to the Earth’s atmosphere and hydrosphere.[160] Therefore, the experimentally observed decrease in available atmospheric halogen might also influence the accuracy of the use of halogens as tracers of igneous processes.

2.4 Conclusions

We have presented a novel analytical method based on a combination of STXM and NEXAFS spectroscopy that allows quantitative analysis of the chemical and hygroscopic properties of individual submicrometer particles. The approach permits quantification of water in an individual particle during hydration and dehydration cycles. Through the case studies using several atmospherically relevant particles, we have showed the STXM/NEXAFS approach could provide unique and quantitative information on the physical and chemical properties of environmental particles and how these change as a function of relative humidity. We anticipate the approach will be especially useful for quantitative studies of the spatially resolved hygroscopic properties of multicomponent aerosols with complex mixing states.

CHAPTER 3

EFFECT OF ORGANIC ACIDS IN THE HYGROSCOPIC PROPERTIES OF NACL PARTICLES USING CCSEM AND MICRO-FTIR SPECTROSCOPY

3.1 Introduction

3.1.1 Composition and physical properties of aerosols

Environmental particles are typically a complex mixture of various compounds in a unique molecular ratio.[161,162] Compositional differences in these particles can often create significant impact on Earth's climate and the atmospheric environment.[163,164] For example, absorption and scattering of solar radiation, formation of cloud condensation nuclei, heterogeneous reaction during their transport etc. are directly dependent on the composition of the particles in the atmosphere.[163-166] Whereas mixture of organic substances is ubiquitous in the environment, a prime example being the humic substances and secondary organic aerosols (SOAs),[167,168] complex aerosol particles with mixture of inorganic and organic compounds are also regularly detected in the atmosphere as well.[12] Inclusion of organic component in inorganic salt is particularly interesting as their physical properties tend to show a significant change in the mixture as compared to the pure component.[128] Therefore, study of compositional dependence of physical properties of the atmospheric particles is important in this scenario.

3.1.2 Hygroscopic properties and its composition dependence

One of the most important physical properties of atmospheric particles which directly influence the radiative and non-radiative effects is the hygroscopic properties as described in the previous chapter while discussing the hygroscopic properties of inorganic salts. The amount of water uptake at a particular atmospheric relative humidity (RH) largely depends on the functional group type (i.e. polar/nonpolar) and the overall chemical composition inside the particle. For example, water uptake of clay particles was observed to be influenced significantly by the presence of sodium chloride salt.[169] Recent studies have shown noticeable changes in hygroscopic properties of ammonium sulphate on internally mixing it with organic acids.[128,170] In addition, these changes cannot be justified in most cases by linear combination of hygroscopic response of the two chemical components present. Moreover, prediction of water uptake using different environmental models also observed to fail for these complex mixtures.[169] Therefore, study of hygroscopic properties as a function of composition in a two component mixture would enable us to predict environmental effects of fine particles with varying composition.

In this project we have focused on NaCl particles which show distinct water uptake with DRH and ERH being 75% and 48% respectively.[31] On the other hand organic di-carboxylic acids such as malonic acid (MA) and glutaric acid (GA) show continuous water uptake as a function of RH. Internally mixing MA and GA with NaCl in various molar ratios resulted in drastic changes in water uptake properties, studied by micro-FTIR spectroscopy. Scanning electron microscopy (SEM) combined with Energy-dispersive X-ray spectroscopy has been used to observe changes in morphology and ratio of Na/Cl in the particles. The result of CCSEM elemental analysis is finally used to predict the changes in hygroscopic properties of NaCl on inclusion of MA and GA in different molar ratio. Furthermore, mixture of NaCl with fulvic acid in different mass ratio has also been studied.

3.2 Experimental details

3.2.1 Materials and sample preparation

All sample of sub-micrometer sized particles were generated using constant output atomizer (TSI, Inc., model 3076) from aqueous 0.2 M solution prepared from reagent-plus-grade chemicals (99.99%+ purity, Aldrich). The solution was prepared with deionized water (18 MΩ•cm). Aerosol was dried down to ~30% RH in a diffusion dryer (TSI, Inc., model 3062) prior to sizing and substrate deposition using a micro-orifice uniform deposit impactor (MOUDI) (MSP, Inc., model 110). Particles were deposited on Si_3N_4 windows (Silson Ltd., England) mounted on the impaction plate of the seventh stage of the MOUDI. The aerodynamic cutoff size of the seventh stage is 0.32 µm. All samples were prepared at room temperature and used within a couple of days after the preparation.

3.2.2 micro-FTIR spectroscopy

Detailed description of the micro-FTIR experimental setup and its application for studies of particle hygroscopic phase transitions and growth has been reported elsewhere,[125,171] and thus will be described only briefly here. The apparatus comprised a Bruker A590 IR optical microscope interfaced with a Bruker IFS 66/S FTIR spectrometer equipped with a liquid-nitrogen-cooled mercury-cadmium-telluride (MCT) detector. Turning mirrors were used to switch between pathways for visible (optical mode for sample location) and IR irradiation of the sample (acquisition of FTIR spectra). Cassegrainian optics was used to focus the IR beam on the sample and to collect the transmitted IR light after its interaction with the sample. The Si_3N_4 window substrate with deposited particles was placed in a sample holder inside a sealed environmental stage (model THMS 600, Linkam, Inc.). An aperture placed in the optical path defined the sample area over which the FTIR spectrum was acquired. RH inside the environmental stage was controlled by a continuous flow of mixed dry and humidified nitrogen with a total flow rate of 1.0 slpm. An inline sensor (Honeywell, inc., model HIH4000) was used to monitor RH with an accuracy of 3%. Experiments were performed at room temperature (24 °C).

The micro-FTIR was first set at the optical mode, which allows selection of the specific area of the sample defined by the aperture to be irradiated by the IR beam. After switching the microscope to the IR transmission mode, FTIR absorbance spectra were acquired by co-adding 512 scans at a resolution of 4 cm^{-1}. After changing RH to a new setting, a typical delay of 5 min was required before equilibrium between particles and water had been reached. The same ensemble of approximately 100 particles was monitored in the experiments. Condensed-phase water in the particles was quantified from the integrated absorbance of the OH stretching band.[125]

3.2.3 Atomic force microscopy (AFM)

Atomic force microscopy (AFM) has been used to obtain height images of MA and GA particles. AFM imaging was conducted using a molecular force probe 3D AFM

(Asylum Research, Santa Barbara, CA). Height images were collected at room temperature using silicon probes (MikroMasch, San Jose, CA,CSC37) with a nominal spring constant of 0.35 Nm^{-1} and a typical tip radius of curvature of 10 nm.

3.2.4 Scanning Electron Microscopy (SEM) and Energy-dispersive X-ray spectroscopy (EDX)

An FEG XL30 scanning electron microscope (FEI, Inc.) was used in this work. The microscope is equipped with an X-ray spectrometer (EDAX, Inc) with a Si(Li) detector of an active area of 30 mm^2 and an ATW2 window. The instrument can also operate in computer-controlled (CCSEM/EDX) mode for analysis of individual particles. Details of this instrument and its applications for the analysis of substrate-deposited particles can be found in a recent review article and references therein.[172]

3.3 Results and discussion

This work is presented in following manner. First, we will present morphology and hygroscopic properties pure component such as NaCl, MA and GA. Second, SEM images and FTIR spectra of mixture samples of malonic and glutaric acid with NaCl will be shown to characterize their morphology and chemical composition respectively. Then, elemental composition analysis will be correlated with the changes in hygroscopic properties. In the final part, hygroscopic properties of fulvic acid (FA) and NaCl mixtures will be presented.

3.3.1 Morphology and hygroscopic properties of pure NaCl particles

Figure 3.1a shows the SEM images of sodium chloride crystals before exposure to water vapor. The rectangular shape of the particles indicates highly crystalline behavior. This type of morphology of NaCl sub-micrometer particles are consistent with the literature.[125] Figure 3.1b shows the FTIR spectra acquired for an ensemble of NaCl particles over the unmasked sample area at increasing values of RH. Initially, no distinct signature in the FTIR spectra was observed due to absence of any vibrational mode in NaCl. The integrated peak area of the OH stretching band in the region from 3660 to 2750 cm^{-1} is used to quantify the hygroscopic properties as the peak area is directly proportional to the amount of water in particles.[125,173]

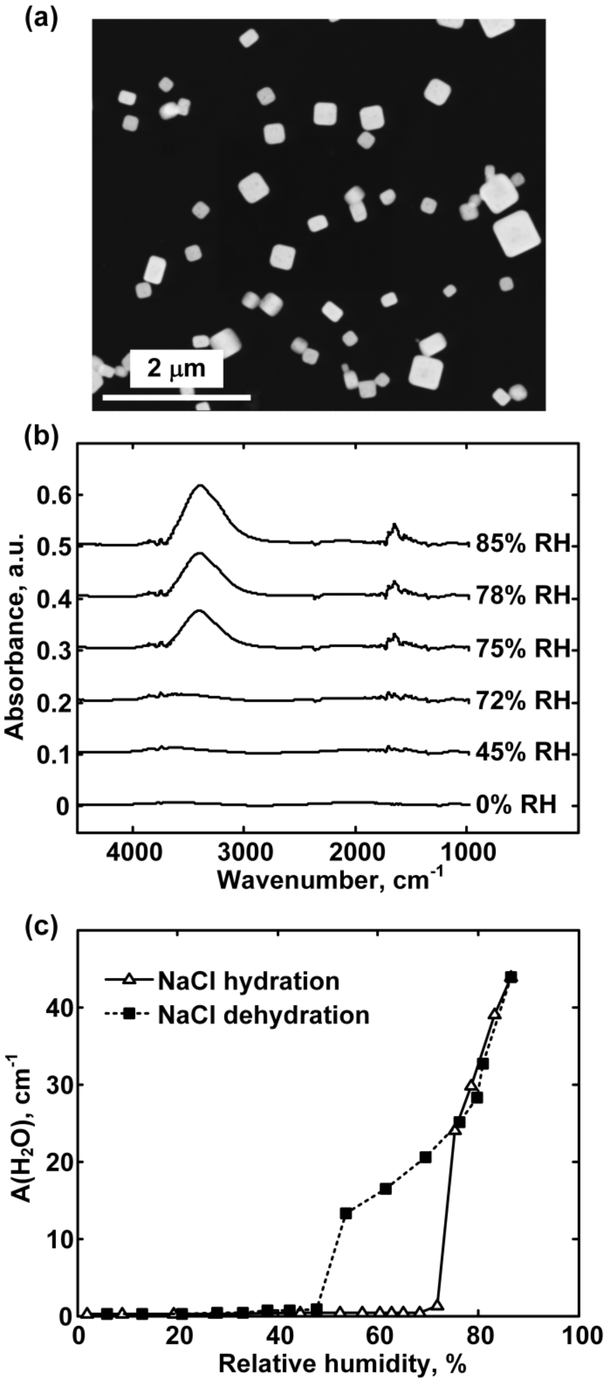

Figure 3.1(a) SEM images of NaCl particles showing consistent square shape of the crystals. (b) FTIR spectra of NaCl crystals with increasing RH showing appearance of broad –OH stretching band centered at ~3400 cm^{-1}. (c) Hydration and dehydration of NaCl particle quantified by plotting the peak area of the –OH stretching band as a function of RH.

As the RH is incrementally raised, absorption spectra were continuously recorded (only selected spectra are shown here). Condensed phase water remains undetectable until RH around 70% at which point the infrared feature of the water band begins to appear in the spectrum. As RH further increases, a considerable amount of water is taken up. It is seen that NaCl particles deliquesce at around 75% RH, resulting in an abrupt increase in the absorbance in the peak centered at 3400 and 1640 cm^{-1}. The swift change indicates that solid NaCl particles deliquesce nearly spontaneously to form saturated solution droplets. Then, the NaCl deliquesced droplets continue to grow with further increases in RH as indicated by-OH band growth and expansion. Infrared spectra of the NaCl droplets recorded in the dehydration cycle (not shown here) are similar to those in Figure 3.1b. Their variations are merely in the reversed order (not shown here). Upon decrease of RH and evaporation, the NaCl droplets gradually lose their water content and water bands in the FT-IR spectra diminish accordingly with an abrupt shrinkage in the absorbance during the efflorescence.

The change in water content in the particle throughout the complete hydration/dehydration cycle is shown in Figure 3.1c. The particle water content is expressed by plotting the integrated peak area (described above) as a function of RH. As RH increases and reaches around 75% during the hydration, a rapid water uptake spontaneously takes place to transform the NaCl particles into deliquesced droplets. With further increase in the RH, particle water content increases accordingly. In the dehydration path, water peak continuously decreases till 48% ERH is reached, when an abrupt release of water causes phase transition back to solid NaCl particles. The hygroscopic properties observed here are consistent with the literature.[125,174,175]

3.3.2 Hygroscopic properties of MA and GA

Water uptake of the pure malonic acid (MA) and glutaric acid (GA) particles were studied next. High resolution AFM images were acquired initially to characterize the morphology of the sample. Figure 3.2 shows AFM height image of dry MA and GA particles. Particle size has been measured to be 0.2-1.2 μm for both the samples. The particle morphology is consistent with reported work on MA and GA particles in the literature.[173,176]

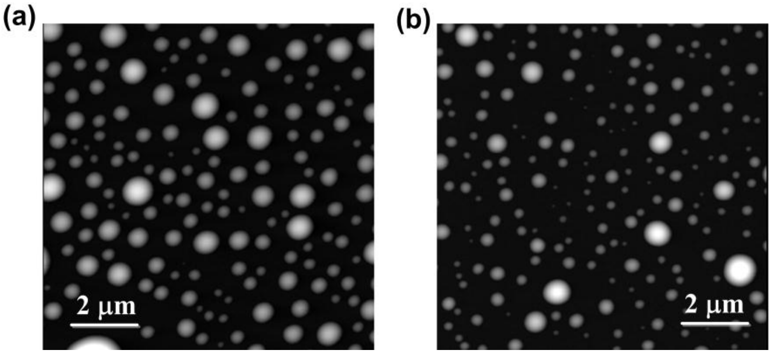

Figure 3.2 AFM height images of (a) glutaric and (b) malonic acid showing consistently spherical shaped particles of size ranging from 0.2-1.2 μm.

In the next step, MA and GA particles were subjected to micro-FTIR spectroscopy. FTIR spectra of these two dicarboxylic acids are shown in Figure 3.3. Initially, typical signatures due to the organic acids were observed in the beginning of the experiment at 2% RH, with nearly undetectable amount of water. All relevant transition due to MA and GA are verified with literature and reported in Table 3.1.[176-179] The transition centered at ~3000 cm^{-1} could interfere with the water peak at ~3400 cm^{-1}. Therefore, all the IR spectra have been subtracted from the initial (~2% RH) to remove spectral intensity contribution from organic acids towards particle water content measurements.

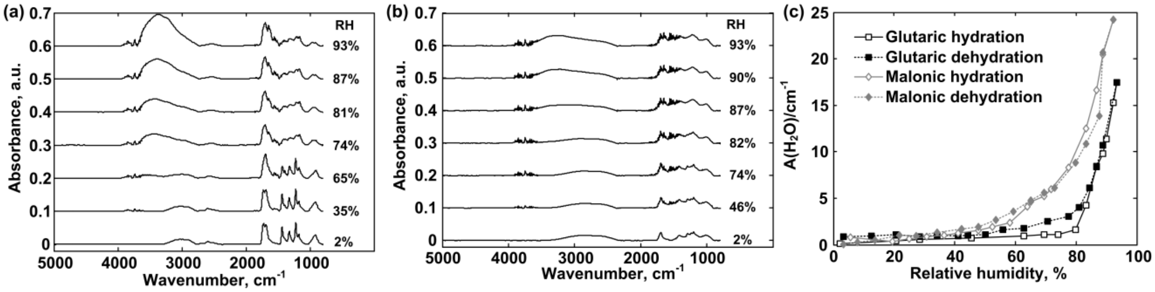

Figure 3.3 Changes in FTIR spectra of (a) malonic and (b) glutaric acid particles as a function of RH, showing gradual increase in -OH stretch in the spectral region of 2750-3660 cm^{-1} due to water uptake. (c) Hygroscopic properties of malonic and glutaric acid particles showing slow and continuous water uptake as a function of RH (Although a small deliquescence phase transition has been present for glutaric acid at ~80% RH).

Table 3.1 FTIR peak assignment of MA and GA

Compound	Absorption maxima, cm^{-1}	Assignment
Malonic acid[177-179]	1174	γ(CH$_2$), ω(CH$_2$)
	1223	γ(C-C)
	1323	γ(C-O)
	1431	υ(O-H), δ(CH$_2$)
	1722	υ(C=O)
Glutaric acid[176]	1200	γ(CH$_2$)
	1238	ω(CH$_2$), γ(C-C)
	1294	υ(C-O)
	1414	υ(O-H), δ(CH$_2$)
	1697	υ(C=O)

*Bands are as shown in Figure 3.3a, b. ν, stretching; ω, bending; γ, rocking.

With gradual increase in RH, particle water content increases and characteristic –OH stretch peak was observed centered at ~3400 cm^{-1}. The hygroscopic properties plot shown in Figure 3.3c has been generated in a similar manner as described above for NaCl particles. Unlike the NaCl particles, MA and GA don't show any sharp deliquescence or efflorescence phase transition, however. While MA particles showed continuous water uptake, GA particles had a relatively weak deliquescence transition at ~80% RH. Moreover, no significant hysteresis was observed either for both the samples. Finally, shape of the hygroscopic properties curve and absence of any sharp phase transition for dicarboxylic acid components was consistent with the literature. [127,131,173]

3.3.3 Morphology of internally mixed MA/NaCl and GA/NaCl particles

Internally mixed 3:1, 1:1 and 1:3 molar ratios of MA/NaCl and GA/NaCl samples were prepared from solution mixtures. The collected particles in MOUDI (Stage 7) were then subjected to computer controlled Scanning Electron Microscopy (CCSEM) to observe changes in morphology along with elemental analysis. In this section, we report changes in morphology of NaCl particles on internally mixing with organic dicarboxylic acids in various molar ratios prior to any water vapor exposure (Figure 3.4). For all the samples in this section the shape of the particles is significantly different compared to the NaCl particles reported in Figure 3.1a; whereas NaCl particles are rectangular in shape, the particles in the mixture samples generally tend to be more rounded. Moreover, a shuttle difference has been observed in morphology of MA/NaCl and GA/NaCl samples. Comparing Figure 3.4a and 3.4d, the morphology of the 1:3 molar ratio mixtures looks more rectangular shaped for GA/NaCl as compared to MA/NaCl; similar shape effects are observed for both 1:1 mixtures. Interesting inhomogeneous mixing states were observed for most of the samples, such as organic inclusion (both the 1:3 samples, Fig. 3.4a, d), core-shell structure (1:1 MA/NaCl, Fig. 3.4b), and inclusion of small sodium chloride crystals (3:1 GA/NaCl, Fig. 3.4f). Interestingly, 3:1 MA/NaCl (Fig 3.4c) sample was a homogeneous mixture, whereas the 1:1 GA/NaCl (Fig. 3.4e) had observable inhomogeneity in mixing for larger particles. Overall, MA affected the pure NaCl crystalline morphology to a greater extent compared to GA.

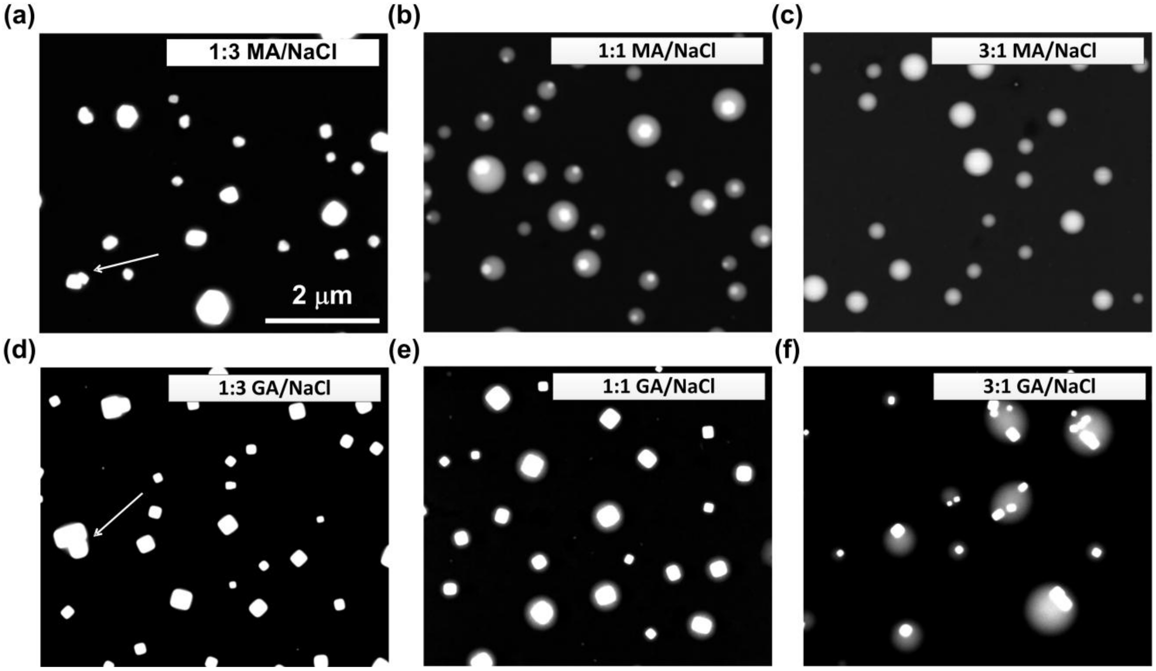

Figure 3.4 SEM micrograph showing morphology of MA/NaCl (a, b, c) and GA/NaCl (d, e, f) particles prepared from various solution molar ratios. The arrow in figure (a) and (d) shows example of organic inclusion in some particles.

3.3.4 Compositional analysis of MA/NaCl and GA/NaCl particles

Internally mixed MA/NaCl and GA/NaCl mixtures were prepared from the aqueous solution in respective molar fractions as described in the experimental section. Depending on the pKa of –COOH functional groups in MA and GA, we anticipated a possibility of formation of Na-malonate and Na-glutarate in the particles. Hence, all the samples were subjected to CCSEM elemental analysis, expecting a deviation from Cl/Na = 1, generating from potential evaporation of HCl. In addition, effect of size of the particle has also been observed as we have analyzed at least 1500 particles for each sample. Plot of Cl/Na ratio as a function of particle size is shown in Figure 3.5. Cl/Na ratio was ~10% lower than expected for particle size below 500 nm, which is likely a result of beam damage. Next series of samples analyzed were GA/NaCl mixtures. In this case, 1:3 and 1:1 molar ratio of GA/NaCl showed nearly similar ratio as NaCl, although careful observation reveals a slight decrease in Cl/Na ratio for 1:1 mixture. To the contrary, 3:1 GA/NaCl mixture had 20-25% Cl depletion. For the MA/NaCl series of mixtures, depletion of Cl was 5-10, 30-35 and 100% for 1:3, 1:1 and 3:1 mixtures respectively. Hence, Cl depletion confirms evaporation of HCl from the sample with the formation of Na-glutarate and Na-malonate. In the next step we will observe the effect of Cl depletion on the hygroscopic properties.

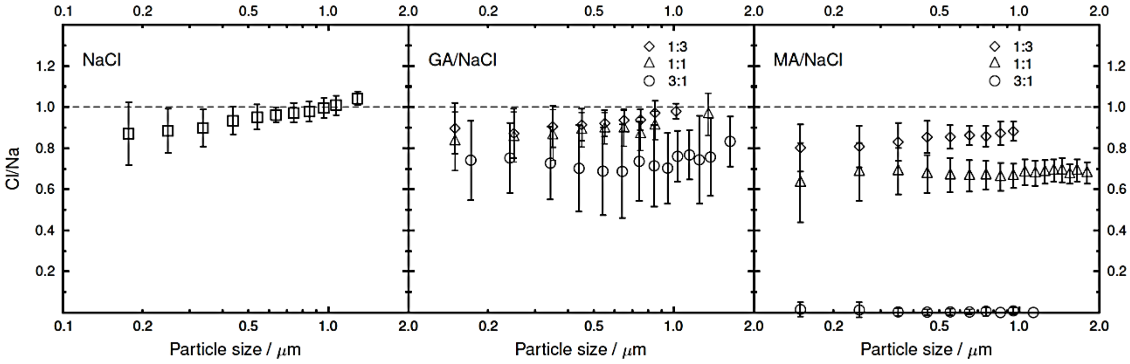

Figure 3.5 Cl/Na ratio is plotted as a function of particle size for NaCl, GA/NaCl and MA/NaCl particles in different molar ratios. Depletion of Cl has been observed with increasing organic acid fraction.

3.3.5 Effect of Cl depletion on hygroscopic properties

Na-malonate and Na-glutarate are expected show a distinctly different hygroscopic response as it has been previously reported for the similar salts of sulphonic acids by Liu *et al*.[171] Therefore, we expected hygroscopic properties of different samples in GA/NaCl and MA/NaCl to be significantly different from the NaCl particles. Figure 3.6 shows hygroscopic properties of all the internally mixed samples. In contrast to the hygroscopic properties of NaCl particles, the sharp deliquescence is completely missing for all the internally mixed samples (Figure 3.6a). Even with 25% MA inclusion (1:3 MA/NaCl), the deliquescence was weak and the hysteresis in the water uptake curve has been majorly affected. The chloride depletion for this sample was only 5-10%. Hence, formation of a small amount of Na-malonate resulted in significant effect on hygroscopic properties. With increasing amount of MA (1:1 and 3:1 MA/NaCl mixture), the water uptake curves merge with that of 100% malonic acid, showing continuous water uptake starting from ~50% RH. Similar effect has been observed for GA/NaCl internally mixed samples as well (Figure 3.6b). In this series of samples, 25% GA inclusion caused a diminished deliquescence along with absolutely no hysteresis in the water uptake curve. 50% and 75% of GA inclusion enhanced the effected and water uptake was continuous as a function of RH.

Comparing the changes in hygroscopic properties of the two series of mixtures (MA/NaCl and GA/NaCl), we observed that MA has affected the hygroscopic properties of NaCl more than GA. For example, hygroscopic properties plot looks slightly different for all the GA/NaCl fractions, but the water uptake curve merged with that of MA for 1:1 and 3:1 MA/NaCl mixture. This observation is consistent with the extent of Na salt formation observed in the previous section of CCSEM elemental analysis. Furthermore, greater extent of Na-malonate formation compared to Na-glutarate can be justified by the lower pKa (1) of MA, suggesting comparatively easier dissociation in solution.[180,181] To summarize, internally mixed organic acid and inorganic salt (NaCl) particle displayed completely different hygroscopic response as compared to inorganic counterpart.

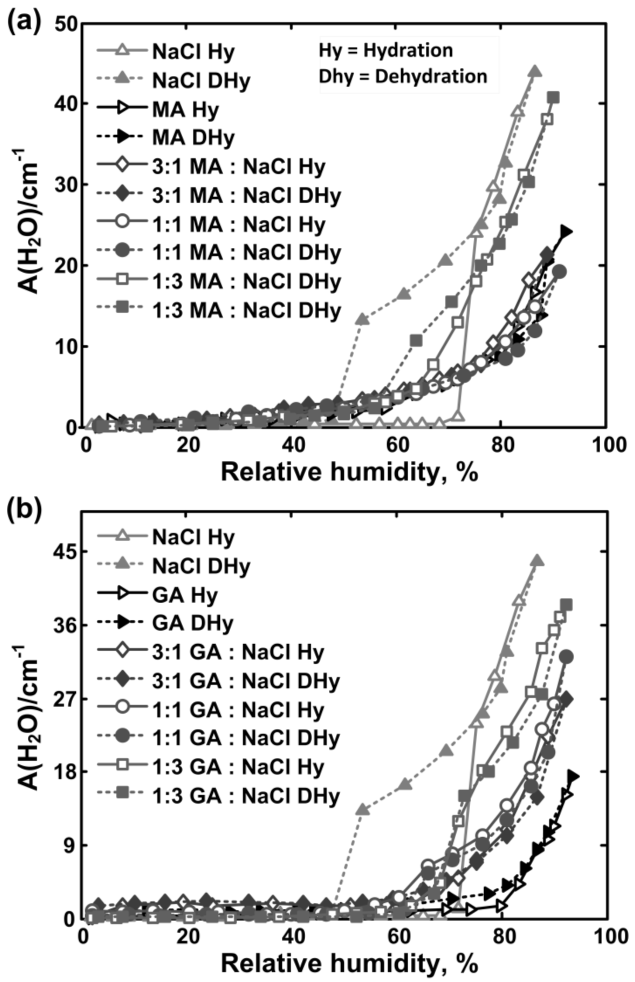

Figure 3.6 Hygroscopic properties of internally mixed (a) MA/NaCl and (b) GA/NaCl particles in different molar ratios, showing the effect of Cl depletion on water uptake.

3.4 Conclusions

Internal mixing of dicarboxylic acids with NaCl showed significant effect on the hygroscopic properties of NaCl. Sharp deliquescence and efflorescence phase transition of NaCl were absent in all the two components mixtures in different molar ratios, instead showing a slow and continuous water uptake as a function of RH. Similar effects on hygroscopic properties were observed with other internally mixed inorganic and organic compounds reported in the literature.[111,182] CCSEM elemental analysis showed Na-malonate and Na-glutarate formation, suggesting its implication to study effects of atmospheric particles, composed of inorganic salts and organic acids. The effect on hygroscopic properties will significantly influence the formation of cloud condensation nuclei (CCN) by the atmospheric particles with similar chemical components. Moreover, physical, optical and chemical properties can also be significantly different. For example, scattering and absorption of solar radiation, atmospheric transport etc. could be a result of observed salt formation. Hence, this study could be utilized to improve environmental models to characterize overall aerosol effects on earth climate.

CHAPTER 4

DIRECT QUANTIFICATION OF DENSITY AND ELEMENTAL COMPOSITION OF SUB-MICROMETER PARTICLES

4.1 Introduction

Precise knowledge of density and elemental composition of environmentally relevant submicron particles is necessary to predict their relevant environmental effects.[48,49,58,183-187] It has been observed that the density and chemical composition of materials have significant effects on physical properties of aerosols such as, light scattering efficiencies, hygroscopicity and CCN activity.[108,183,184,186] For example, a chemical closure study has been performed on the hygroscopicity of organic/inorganic mixed particles nebulized from water extracts of ambient aerosols collected in Sapporo, Japan and differences in hygroscopic properties has been found with various different chemical composition.[108] On the other hand, research on visibility due to scattering efficiency of solar radiation has been examined as a function of aerosol constituents.[185] Kinetics of various environmental oxidation and reduction processes was observed to be controlled by density and composition of aerosol.[49] Another study on the formation of secondary organic aerosol (SOA) showed that the solubility of organic compounds in aerosols depend largely on the amount of oxygen containing organic functional groups in the sample under examination.[48] All these different studies on both laboratory generated and field samples indicate that the density and chemical composition of airborne particles control most of their physical properties; hence direct quantification of density and elemental composition is necessary in order to examine various physicochemical properties of aerosols.

Particle density and elemental composition has been observed to control several properties of nanomaterials and hence prior knowledge of these parameters is required in various studies in nanotechnology.[188-190] For example, the frequency of Localized surface plasmon resonances (LSPRs), resulting from the interaction of light with metal nanoparticles depends exclusively on the particle size and composition.[190] Moreover, dependence of magnetic properties of metal nanoparticles on the composition has also been examined in recent years.[189] Therefore, it is evident that quantifying density and elemental composition of submicron and nanoparticles is essential in the context of not only environmental chemistry but also nanotechnology.

Density measurements of submicron particles have been performed before using combination of various different techniques. The first density quantification was performed to quantify the mean bulk density of dry atmospheric aerosol particles; however the procedure of measurement was slow and less accurate.[191] Later on, Differential Mobility Analyzer (DMA) was used to determine aerosol particle densities with specific assumptions about the shape of the particle.[192] On the other hand, relationship between electrical mobility and mass has been used to quantify ‘effective density’ of the aerosol particles.[193,194] Moreover, Aerosol Particle Mass Analyzer (APM)/Scanning Mobility Particle Spectrometer (SMPS) setup was used to examine the density evolution of SOA.[195] But, careful observation shows that most of these techniques make different assumption to determine either the mass or the diameter of the particles. In addition, it is well known that the physicochemical properties of fine particles can be different compared to the bulk and particle to particle variation may also occur as well.

Therefore, direct determination of density of submicron particles on a single particle basis is necessary in this scenario.

A handful of techniques has been reported in literature to quanitfy elemental composition of submicron particles. The composition of SOA was characterized by a high-resolution time-of-flight aerosol mass spectrometer in a continuous flow chamber.[196] Other methods such as Mass spectroscopy (MS) and combination of Scanning Electron Microscopy (SEM) and Energy Dispersive Spectrometry (EDS) has also been used for the same purpose for different environmental sample.[197,198] Hence, it is worthwhile to realize that determination of both density and elemental composition by directly quantifying the mass and the diameter of submicron particles using a single experiment will be an important milestone. Moreover, exploring particle to particle variation in density and elemental composition using the same method will also be an importance property to observe.

In this work, we report a new technique utilizing an unique combination of Scanning Transmission X-ray Microscopy (STXM)/Near Edge X-ray Absorption Fine Structure Spectroscopy (NEXAFS) and Atomic Force Microscopy (AFM) to directly quantify the density and elemental composition of sub-micrometer particles. Contribution of atomic densities towards overall particle density has been calculated directly from the experimental data. In this work, we report four different samples of submicron particles under investigation, namely, sodium nitrate ($NaNO_3$), mixture of malonic acid ($C_3H_4O_4$) and $NaNO_3$, fulvic acid, and a mixture of fulvic acid and $NaNO_3$. With the first two samples, the accuracy of our method has been verified and afterwards we report application of this method for more atmospherically relevant samples with unknown composition.

4.2 Experimental details

4.2.1 Materials and sample preparation

Particles of $NaNO_3$, mixture of malonic acid and $NaNO_3$, Fulvic acid, and Fulvic acid and $NaNO_3$ were generated using constant output atomizer (TSI, Inc., model 3076) from aqueous solutions prepared from reagent-plus-grade chemicals (99.99%+ purity, Aldrich). All solutions were prepared with deionized water (18 MΩ•cm). The solution concentration for the first two samples was 0.1 M. For the last two samples specific mass ratio has been used as fulvic acid has variable composition and the molecular formula in apparently unknown. The pure fulvic acid particles were generated from 250 mg/liter solution; whereas a mass ratio of fulvic acid : $NaNO_3 = 5 : 1$ was used for the corresponding mixture sample. The generated particles were dried down to ~30% RH in a diffusion dryer (TSI, Inc., model 3062) prior to sizing and substrate deposition using a micro-orifice uniform deposit impactor (MOUDI) (MSP, Inc., model 110). Particles were deposited on Si_3N_4 windows (Silson Ltd., England) mounted on the impaction plate of the seventh stage. The aerodynamic cutoff size of the seventh stage is 0.32 µm. All samples were prepared at room temperature and used within a couple of days after the preparation.

4.2.2 Scanning Transmission X-ray Microscopy (STXM)

Single energy images and oxygen Near Edge X-ray Absorption Fine Structure (NEXAFS) spectra were acquired using STXM instrument on beamline 5.3.2 of the

Advanced Light Source at Lawrence Berkeley National Laboratory (Berkeley, CA). For STXM measurements, the X-ray beam is focused with a custom made Fresnel zone plate onto the sample, and the transmitted light intensity is detected. The diffraction limited spot size at the sample was ~25 nm for these experiments. Images at a single energy are obtained by raster-scanning the sample at the focal plane of X-rays and collecting transmitted monochromatic light as a function of sample position. Spectra at each image pixel or a particular sample region are extracted from a collection of images recorded at multiple photon energies across the absorption edge. Dwell times used to acquire an image at single photon energy were typically 0.5 ms per pixel. To quantify the absorbance signal, the measured transmitted intensity (*I*) is converted to optical density (*OD*) using the Beer-Lambert's law described in previous chapter. Incident beam intensity is measured through the area of substrate free of particles. Particle spectrum is obtained by averaging the absorbance signal over the particle projection area on the substrate.

NEXAFS spectral features arise from electronic resonance transitions of core electrons specific to different bonding of elements (e.g. different functional groups) and involve both $1s \rightarrow \pi^*$ and/or $1s \rightarrow \sigma^*$ transitions. Peaks arising due to σ^* transitions are usually broader than for π^* transitions and superimposed on the photo-ionization continuum. Spectra from 1s electrons for C atoms are in the energy region of 280-320 eV; whereas the spectra from N and O atoms 1s electrons are in the energy region of 395-420 eV and 525-550 eV respectively. The pre-edge background arises from the combined absorption of other elements at that energy. The post-edge absorbance depends on the number of respective atoms. The total atomic absorbance is defined as the difference between the post-edge and pre-edge absorbance at 525 eV. The total atomic absorbance is directly proportional to the number of corresponding atoms inside a particle and can be used as a direct measure of concentration of the corresponding atom.[58] In the present study, the total atomic absorbance is used to quantify the density of C, N, and O atoms present in the particle.

4.2.3 Atomic force microscopy (AFM)

All AFM topographic height images were performed in AC mode (intermittent contact mode) using a commercial atomic force microscope (MFP3D, Asylum Research, Santa Barbara, CA). A single crystal silicon AFM probe (Mikromasch, San Jose, CA) with a typical tip radius of curvature of ∼10 nm and a nominal spring constant of 0.40 N/m was used for all experiments. All experiments were performed in air and at room temperature.

4.3 Result and discussion

4.3.1 Density and elemental composition using a combination of AFM and STXM

The substrate deposited particles exhibited approximately elliptical morphologies. With the knowledge about the morphology, we designed a method to quantify the density and elemental composition of the sub-micron sized particles using a combination of synchrotron-based STXM and AFM.[58] STXM provides spatially-resolved (~ 25 nm resolution) total atomic absorbances (OD) that can quantified using the Beer-Lambert's law:[58]

$$OD_i = \mu_i \rho_i h \ldots\ldots\ldots\ldots\ldots\ldots\ldots\ldots\ldots\ldots\ldots\ldots.(1)$$

where i is the atom type (*i.e.* C, N or O), OD_i is the total atomic absorbance in units of optical density (OD) in corresponding absorption edges, μ_i is the mass absorption coefficient for the corresponding atom, ρ_i is the atomic density of the particle, and h is the particle thickness. Since STXM essentially measures a product of density and thickness, a density determination required knowledge of thickness of the particles, which we obtained from the AFM height images. Moreover, by combining the AFM and STXM data, we can quantify atomic ratios on a single particle basis as well. The combination of the methods could also, in principle, be extended to other submicron particles of nanomaterials with known shape (*e.g.* biological samples). The similar approach has been adopted in our previous work to quantify the density of thixotropic hydrogel sample.[199] Herein, we show the extensive application of this approach in more quantitative manner for submicron particles of different compositions.

4.3.2 Density and elemental composition of $NaNO_3$ particles

To begin with, we have examined substrate deposited particles of pure sodium nitrate ($NaNO_3$). As described in the experimental section the particles are substrate deposited on Si_3N_4 membrane. Atomic Force Microscopy (AFM) images were acquired to determine the shape of the particles and subsequently quantify the thickness of the particle (Figure 4.1a). As expected, the particles had a half ellipsoid shape. The size of the particles varied from 0.3 to 1.2 µm. Afterwards, the same sample is used to obtain total atomic absorbance maps in N (420 eV- 395 eV) and O (550 eV – 525 eV) absorption edges in STXM. The total nitrogen and oxygen atomic absorbance maps are shown in Figure 4.1b and 4.1c respectively. The range of particle size was similar in STXM compared to what was measured by AFM.

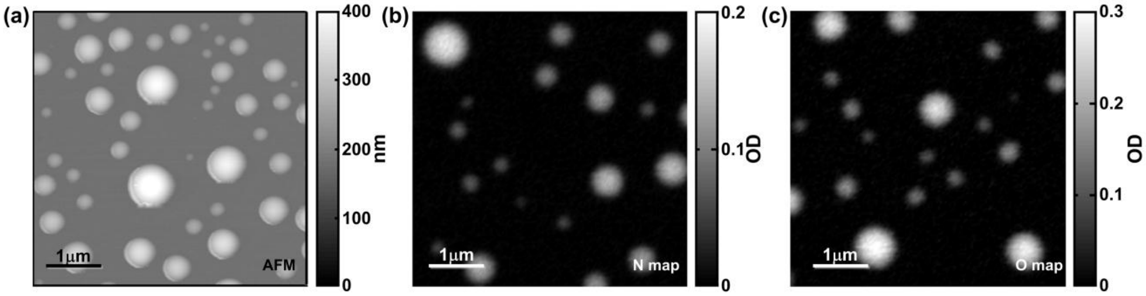

Figure 4.1 Morphology of $NaNO_3$ particles, showing (a) AFM height image (b) STXM nitrogen atomic absorbance map and (c) STXM oxygen atomic absorbance map.

After characterizing the particle size and morphology, the single particle NEXAFS spectra in both nitrogen and oxygen edge was used to chemically characterize the $NaNO_3$ sub-micron particles. The NEXAFS spectrum in N-edge is shown in Figure 4.2a showing two distinct transitions at 401.6 eV and 405.3 eV. The transition at 401.6 eV corresponds to π resonance of NO_2^- species resulting from slight decomposition of sodium nitrate.[200,201] The strong band at 405.3 eV corresponds to the σ* resonance of NO_3^-.[200,201] Moreover, the oxygen NEXAFS spectrum (Figure 4.2b) shows one sharp π resonance (1s→$2a_2''$) at 531.8 eV below the ionization threshold and two broader σ* transitions above it with maxima occurring at 538.1 eV and 543.1 eV, corresponding to $1s\rightarrow 3a'_1$ and 1s→$4e'$ resonances.[200]

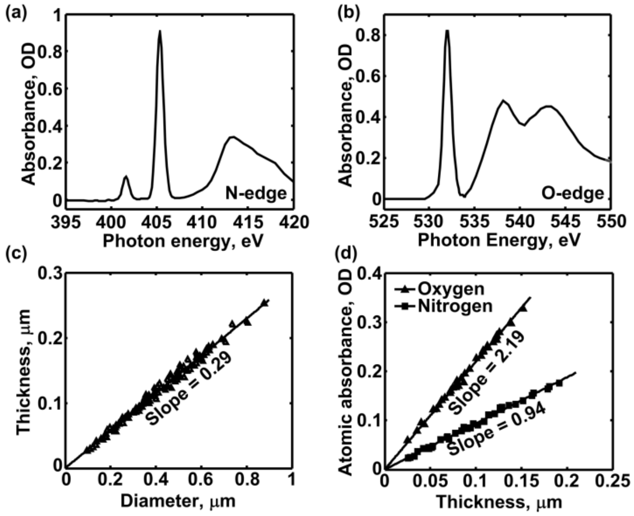

Figure 4.2 Density and elemental composition quantification of $NaNO_3$ particles, showing (a) N-edge and (b) O-edge NEXAFS spectra of $NaNO_3$ particles, (c) Correlation of particle thickness as a function of diameter calculated the AFM height image and (d) plot of atomic absorbance at different absorption edges (N, O) as a function of particle thickness to quantify the density and elemental composition of $NaNO_3$ particles.

In this section, the analysis to quantify atomic density and elemental composition will be described in detail. As discussed before, the basic approach is to use Lambert-Beer's law (eq. 1) and calculate the density directly when all the other parameters are known. Again, it is not possible to calculate the thickness of individual particles from STXM. Herein, we have two options to obtain the thickness. First, we can measure thickness of the particle using AFM height image and consequently obtain the STXM total atomic absorbance map to quantify optical density (OD) of the same particle. Optionally, we can analyze significant number of particles in AFM height image to obtain a correlation between the thickness and diameter of the particles, subsequently measuring the thickness of the particles in STXM total atomic absorbance map from the *thickness vs. diameter* correlation obtained from AFM height image. The latter is better than the former as it is difficult to locate the exactly same particle in both AFM and

STXM. Therefore, the first step was to calculate a correlation of *thickness vs. diameter* from the AFM height image (Figure 4.2c). A minimum of 100 particles have been analyzed to calculate *thickness vs. diameter* correlation for all the different samples reported in this work with very high R^2 value (≥0.98). Each of ~100 particles was analyzed individually in two arbitrary coordinates in order to obtain diameter and thickness in two different directions. Then, the geometric mean of measurements was used to graph thickness as a function of diameter. The slope of the linear fit with zero intercept (0.29 for $NaNO_3$ particles) was used in the next step of the calculation.

STXM atomic absorbance maps were then analyzed to obtain the cross sectional profile in both N- and O-edge through horizontal and vertical linescans across the particle. The cross sectional profile was then used to determine the maximum atomic absorbance approximately at the center of the profile in the corresponding absorption edges. Thickness of these particles was determined from *thickness vs. diameter* correlation discussed in the previous section. The details of these measurements can be found in one of our previous work.[31] Finally, the atomic absorbance was plotted as a function of thickness (Figure 4.2d). Individual atomic densities of N and O atoms were obtained by dividing the slope of *atomic absorbance vs. thickness* plot by mass absorption coefficients in corresponding absorption edges, calculated from the atomic scattering factors and determined to be 3.84×10^4 cm^2/g and 2.80×10^4 cm^2/g for N and O, respectively. Using this approach, the atomic densities of nitrogen and oxygen was calculated to be 0.34 ± 0.02 g/cc and 1.13 ± 0.03 g/cc for $NaNO_3$ particles. By scaling the N:O atomic density ratio with the atomic N and O weights, the atomic ratio of N and O atoms (N:O) was quantified to be 0.34:1, which is in excellent agreement with the molecular formula of $NaNO_3$. Assuming one sodium per nitrate ion in the sample, the total density of $NaNO_3$ in the particle has been calculated to be 2.02 ± 0.05 g/cc which is comparable with the bulk density of sodium nitrate (2.17 g/cc) (Sigma Aldrich). Hence, we have established a method to quantify density and elemental composition of sub-micrometer particles, consisting of one chemical component.

4.3.3 Studies on sub-micrometer particles of 1:1 molar mixture of Malonic acid and $NaNO_3$

In this section, we will discuss about the application of this method for homogeneously mixed sub-micrometer particles will two different chemical components. Herein, it is worthwhile to mention that quantification of total density and atomic ratio in the mixture may still need prior knowledge of the molecular formula. According to the environmental relevance of the mixture of organic and inorganic compounds in fine particles, we studied a homogeneous mixture of malonic acid ($C_3H_4O_4$) and $NaNO_3$. Herein, the sample has been prepared from a mixture of malonic acid and sodium nitrate from the bulk solution prepared in 1:1 molar ratio, although the molar ratio in the substrate deposited particles may be different than the bulk.

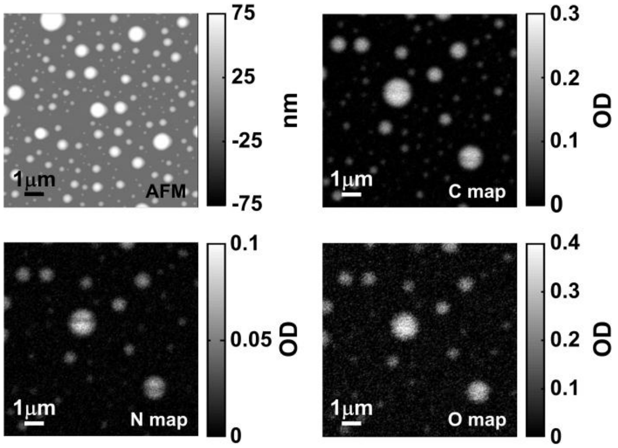

Figure 4.3 Morphology of mixture of malonic acid and $NaNO_3$ particles, showing (a) AFM height image, (b) STXM carbon atomic absorbance map, (c) STXM nitrogen atomic absorbance map, and (d) STXM oxygen atomic absorbance map.

As expected the particles are similar in shape as compared to the pure sodium nitrate particles. The AFM height image in Figure 4.3a shows a half ellipsoidal shape; whereas total C, N, and O atomic absorbance maps (Figure 4.3b-d) show the similar shape and the size of the particles again are comparable to the AFM height image. In this case, total absorbance map has been collected in all three different absorption edges (C, N, and O edge). Existence of both malonic acid and $NaNO_3$ in the sample has been confirmed from the total absorbance maps in all three absorption edges. Furthermore, homogeneous distribution of malonic acid and sodium nitrate in the sample has been observed in total atomic absorbance maps at all the three absorption edges.

The particle of malonic acid and sodium nitrate mixture has been characterized chemically using the NEXAFS spectra in all the three different absorption edges, namely, C, N, and O. Figure 4.4a-c shows the NEXAFS spectra in C, N, and O edges respectively. In C-edge NEXAFS spectrum, two sharp bands has been observed at 288.6

eV and 290.5 eV, corresponding to *COOH* π^* and CH_2 *4p* resonances that proves the existence of malonic acid in the sample.[202,203] On the other hand characteristic sodium nitrate transitions has been observed in the N-edge spectrum at 401.5 eV and 405.2 eV corresponding to NO_2^- π^* and NO_3^- σ^* resonances.[200,201] Moreover, O-edge spectrum also showed all the expected transitions for sodium nitrate as described in the previous section. Along with that one extra transition was observed at 535.1 eV, corresponding to –OH σ^* transition proves the existence of malonic acid.[204] The –COOH resonance in O-edge, which usually occurs at ~532.4 eV, was not resolved clearly in our case due to the presence of sodium nitrate in the sample, giving rise to a resonance at 531.8 eV, ultimately resulting in one cumulative transition with absorption maxima at 531.9 eV.[200,202] Furthermore, the σ^* features at higher energy of sodium nitrate was not clearly visible due to presence of malonic acid in the sample. Therefore, all the observation with C, N and O edge NEXAFS spectra confirmed the existence of both malonic acid and sodium nitrate in the particles.

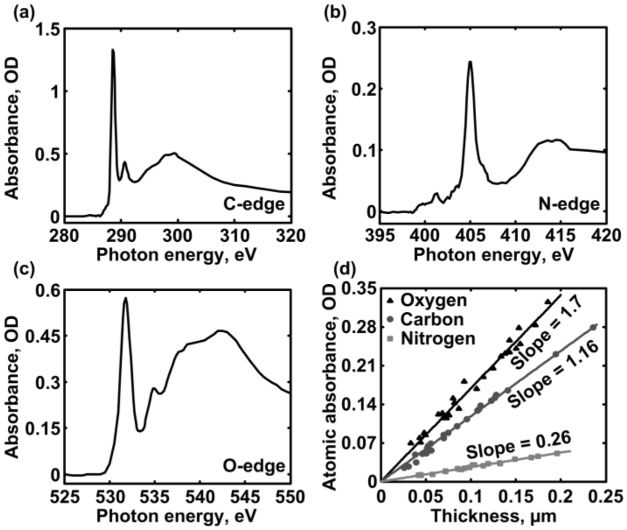

Figure 4.4 Density and elemental composition quantification of mixture of malonic acid and $NaNO_3$ particles, showing (a) C-edge, (b) N-edge, and (b) O-edge NEXAFS spectra of malonic acid + $NaNO_3$ particles and (d) plot of atomic absorbance at different absorption edges (C, N, O) as a function of particle thickness to quantify the density and elemental composition of malonic acid and $NaNO_3$ samples.

The density of C, N, and O atoms for malonic acid and sodium nitrate mixture sample has been quantified by using exactly same procedure as the previous sample. The correlation of *thickness vs. diameter* (Plot not shown here) yielded a slope of 0.15 which is significantly lower compared to 0.29 for pure $NaNO_3$ particles. This variation is understandable with the presence of less crystalline malonic acid with $NaNO_3$. Similar to the pure $NaNO_3$ particles, the atomic absorbance map measured in C, N, and O edges using STXM has been utilized to obtain the maximum atomic absorbance and the size of the particle. Afterwards, the slope of the AFM *Thickness vs. Diameter* was used to calculate the thickness of the particles analyzed using STXM. The final plot of atomic absorbance as a function of thickness is shown Figure 4.4d for quantification of atomic densities of C, N, and O. Dividing the slope of the linear fit by corresponding mass absorption co-efficient (μ) yielded the atomic densities, which are summarized in Table

4.1. Similar to pure sodium nitrate particles, the total density of the particle was found to be 1.45 ± 0.09 g/cc, considering one sodium per nitrate ion. It is worthwhile to mention here that the bulk density of pure malonic acid and sodium nitrate is 1.62 g/cc and 2.17 g/cc respectively (Sigma Aldrich). Significantly lower density of the mixture compared to the bulk densities of the individual components indicates porosity of material within the particles under examination. Finally, the atomic ratio was calculated to be C : N : O = 0.45 : 0.12 : 1 using exactly same method described for $NaNO_3$ particles. Due to occurrence of C atoms only in malonic acid ($C_3H_4O_4$) and N only in $NaNO_3$, we can cleverly utilize the atomic ratio of C : N to calculate the molar ratio of the actual compounds, namely, malonic acid and sodium nitrate within the particles by simple scaling of the C : N atomic ratio by the number of C and N atoms present in each malonic acid and $NaNO_3$ molecule respectively. Using this method, the molar ratio of malonic acid : $NaNO_3$ was calculated to be 1.25 : 1 which was significantly different from 1 : 1 solution molar ratio used during sample preparation. This information indicates that homogeneous mixing during the particle formation in the atomizer may occur in different molar ratio compared to the bulk molar ratio. To verify the accuracy of our method, we can calculate the expected amount of O atoms from the C:N molar ratio in the sample as we know the ratio of malonic acid and $NaNO_3$. In this way, C : N : O ratio was calculated to be 0.47 : 0.13 : 1, which is consistent with the observed C : N : O (0.45 : 0.12 : 1) ratio calculated from the atomic densities. Hence, we note that this method can accurately quantify the density, elemental composition, molar ratio of chemical compounds in binary mixtures.

4.3.4 Density and elemental composition of HUMIC acids

In the next step, we decided to observe more environmental aspect of this method by quantifying density of substrate deposited particles of unknown composition. In this part, Suwannee River Fulvic Acid (SRFA) particles were used as an environmentally relevant organic material.[205,206] Both SRFA[206] and a mixture of SRFA and $NaNO_3$ samples will be discussed using the same approach of quantifying density and elemental composition. A typical C-edge NEXAFS spectrum of SRFA is shown in Figure 4.5. Three typical π^* transitions were observed in the spectrum. The transitions at 285, 286.6, 288.6 and 290.6 eV were assigned to be 1s to π^* transitions due to the presence of unsaturated carbon (C=C), phenolic OH (Ph-OH), carboxylic acid (-COOH) and carbonyl (C=O) functional groups;[207] whereas the O K-edge spectra (not shown here) showed only –COOH transition centered at 532.4 eV. Hence, chemical constituents of fulvic acid were assigned from the NEXAFS spectra although exact chemical structure was unknown.

Figure 4.6a and 4.6c shows the C-edge total atomic absorbance map of pure SRFA and mixture of SRFA and $NaNO_3$ samples respectively. For both these samples, irregularity in particle shape was observed compared to the previous two samples consisting of malonic acid and $NaNO_3$. Therefore, special care has been taken while measuring particle diameter. Measurements were performed along the longest and shortest axis of every particle and then the geometric mean has been used in density and elemental composition calculation.

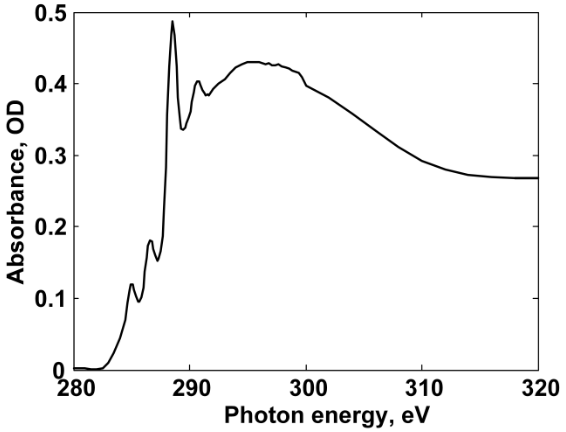

Figure 4.5 Fulvic acid C K-edge NEXAFS spectra

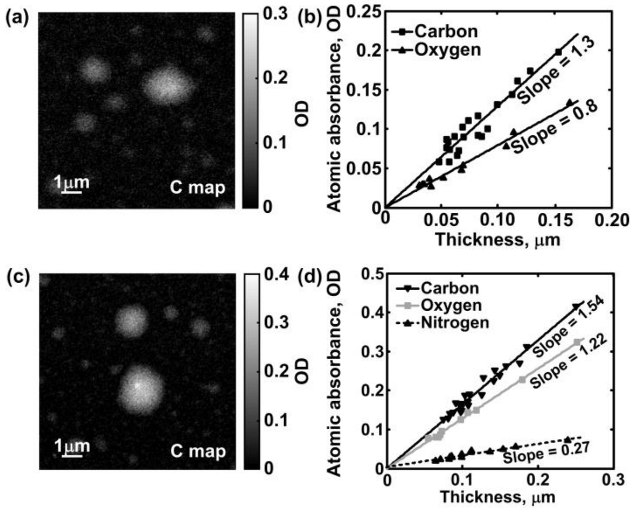

Figure 4.6 (a) STXM carbon atomic absorbance map of pure fulvic acid particles. (b) Plot of atomic absorbance at different absorption edges (C, N, O) as a function of particle thickness to quantify the density for pure fulvic acid particles. (c) STXM carbon atomic absorbance map of fulvic Acid and $NaNO_3$ particles. (d) Atomic absorbance as a function of particle thickness to quantify the density of mixture of fulvic acid and $NaNO_3$ particles.

The *thickness vs. diameter* correlation (not shown here) for both these samples yielded a slope of 0.13 and 0.09 for pure SRFA and mixture of SRFA and $NaNO_3$ samples respectively. Using the slope of these correlations and following the same approach as the previous two samples, atomic absorbance was plotted as a function of thickness to calculate the density and elemental composition (Figure 4.6b,d). Table 4.1 summarizes the density and elemental composition obtained from these plots. The atomic densities of C and O in SRFA were calculated to be 0.34 ± 0.04 and 0.41 ± 0.04 respectively.

The total density of fulvic acid in the sub-micrometer was calculated to be 0.75 ± 0.08 g/cc, which is in reasonable agreement with the reported values in the literature for similar materials such as HULIS or biomass burn aerosols.[58,183,208,209] Herein, it is worthwhile to mention that individual atomic densities of C, N, and O can be determined using this method. But, precise quantification of the density of a material needs some prior knowledge about the molecular formula. Moreover, the experimental atomic ratio in fulvic acid was observed to be C : O = 1.12 : 1 and it differed significantly compared to that predicted (C : O = 1.74 : 1) by the accepted molecular formula, $C_{33}H_{33}O_{19}$,[210] provided by International Humic Substances Society (IHSS). It has been reported that the elemental composition of SRFA may change significantly during particle generation from solution.[183] Moreover, it has also been reported that SRFA is considerably hygroscopic due to presence of very high number of –COOH and C=O group and hence, the particles may retain significant amount of water in the atmospheric relative humidity after sample preparation.[211] Therefore, presence of extra oxygen can be interpreted either due to presence of extra water or due to changes in elemental composition itself during sample preparation from solution.

Table 4.1 Summary of density and elemental composition data for different samples

Sample	**Density of C, g/cc**	**Density of N, g/cc**	**Density of O, g/cc**	**Total density, g/cc**	**Observed atomic ratio(C:N:O)** **[*Expected atomic ratio(C:N:O)*]**
$NaNO_3$	N/A	0.34 ± 0.02	1.13 ± 0.03	2.02 ± 0.05	0 : 0.34 : 1 [0 : *0.33 : 1*]
Malonic acid + $NaNO_3$	0.30 ± 0.03	0.09 ± 0.01	0.88 ± 0.05	1.45 ± 0.09	0.45 : 0.12 : 1 [*0.47 : 0.13 : 1*]
Fulvic acid	0.34 ± 0.04	N/A	0.41 ± 0.04	0.79 ± 0.08	1.12 : 0 : 1 [*1.74 : 0 : 1*]
Fulvic acid + $NaNO_3$	0.40 ± 0.03	0.09 ± 0.01	0.63 ± 0.03	1.30 ± 0.07	0.84 : 0.16 : 1 [*0.88 : 0.17 : 1*]

On the other hand, mixture of SRFA and $NaNO_3$ has been studied to extend the same concept further that we can successfully quantify the individual atomic density, total density and elemental composition in a two component mixture, involving an environmentally relevant organic acid of unknown molecular formula (SRFA) and an inorganic salt ($NaNO_3$). According to the literature, the atmospheric organic acid substances are low density compounds.[58] Therefore, studying this mixture will be interesting to observe the potential increase in the density due to addition of more crystalline inorganic material. STXM total atomic absorbance maps in all the three absorption edges (C, N and O) confirmed homogeneous mixing in the particles. Densities of C, N, and O obtained for this sample were 0.40 ± 0.03 g/cc, 0.09 ± 0.03 g/cc and 0.63 ± 0.03 g/cc respectively. Assuming the accepted molecular formula of fulvic acid and one sodium ion per nitrate ion, the total density observed for this sample was 1.30 ± 0.07 g/cc. Moreover, the experimentally observed atomic ratio C : N : O = 0.84 : 0.16 : 1 has been highly consistent with the expected atomic ratio of C : N : O = 0.88 : 0.17 : 1

calculated from the C : N ratio in the exactly similar method described in the previous section. Therefore, we observed a basic difference in elemental composition between the fulvic acid and fulvic acid/$NaNO_3$ mixture samples, indicating composition dependent changes in fulvic acid molecular formula.[210]

In our experiment, we have used *thickness vs. diameter* correlation to avoid the difficulty to observe the same particle in both AFM and STXM. It can be stated at this point that single particle studies with this approach is also possible by looking at the same particle in AFM and STXM. In addition, particles of irregular shape can also be studied for density and elemental composition quantification using the same approach of studying the same particle in both AFM and STXM. The ability to determine the density and elemental composition with irregular shape indicates that this approach is not only confined to the atmospheric particles with definite shapes but also it can be utilized to observe any micron or submicron sized particles on a single particle basis. Moreover, elemental composition can be verified only with STXM total atomic absorbance maps without any prior knowledge of the molecular formula.

4.4 Conclusion

In this work, we have successfully quantified the density and elemental composition of laboratory generated submicrometer particles, consisting of one or two chemical components. In the process, we have looked at pure inorganic salt particles and verified the method using the mixture of $NaNO_3$ and malonic acid samples. Moreover, the fact that this method enables us to determine the ratio of compounds in two component mixture, enables us to potential apply the same procedure to quantify chemical composition in environmental particles comprising of complex mixture of organic and inorganic compounds. Ability to determine elemental composition of samples of unknown molecular formula shows applicability in environmental chemistry to determine elemental composition of unknown samples. Moreover, study of spatial distribution of density and elemental composition of chemical compounds in heterogeneously mixed submicrometer particles is another important area of application of this approach. Therefore, we state that this fundamental method is important in both chemistry and environmental science perspective and has numerous potential implications for various chemical and atmospheric processes under investigation.

CHAPTER 5

SPATIALLY RESOLVED ELEMENTAL COMPOSITION AND DENSITY OF HETEROGENEOUSLY MIXED SUBMICROMETER PARTICLES

5.1 Introduction

Atmospheric aerosol particles play pivotal role in absorption and scattering of solar radiation, cloud condensation nuclei (CCN) formation, reducing visibility etc., and can in turn affect human health.[212-216] These physicochemical properties of the aerosols directly vary with the density, chemical composition of individual particles and spatial distribution of chemical species within particle as well.[98,183,216] Therefore, these effects have been studied for number of different atmospheric and atmospherically relevant laboratory generated samples.[217] Moreover, atmospheric particles with organic coating have been found to influence aerosols physical, optical and chemical properties.[218,219] Several studies have shown that the knowledge of this mixing in atmospheric aerosols is very important for the environmental modeling to predict a particle's environmental fate.[220] For instance, *Lesins et al.* studied the difference in optical properties such as single scattering albedo, asymmetry parameter and extinction between internally and externally mixed sample of black carbon and ammonium sulphate and observed more than 25% difference for dry sample and 50% difference for wet sample.[216] Furthermore, it is observed that prior knowledge of mixing state in aerosol particles is not only useful to understand their optical and physical properties but also to obtain information about aging of the particles.[221-223]

The effect of density and chemical composition of aerosol particles has a great interest in terms of predicting and justifying environmental processes. For example, *Cruz et al.* reported water uptake of ammonium sulphate and glutaric acid aerosol particles that was significantly enhanced with increasing the organic fraction.[215] In the last decade, the effect of aerosol constituents and their spatial distribution on scattering efficiency of solar radiation has also been demonstrated.[216] Furthermore, the particle density has been determined to be an important parameter in predicting the aerosol life cycle and its transport in the atmosphere.[183] Therefore, quantification of density, elemental composition and spatially resolved chemical mapping on a single particle basis is necessary to entirely predict the effect of aerosol particles on the atmosphere with a desired accuracy.

Combination of scanning electron microscopy and energy dispersive X-Ray (SEM/EDX) has been employed to study aerosol morphology and chemical composition, however, these techniques has potential risk of radiation damage to the sample.[172,224] In addition, chemical composition of particle ensembles has been determined using infrared (IR) and micro Raman spectroscopy, although these techniques lack in ability to quantify density.[125,225] Alternatively, density of submicron particles has been quantified using various techniques such as Differential Mobility Analyzer (DMA), Aerosol Particle Mass Analyzer (APM)/Scanning Mobility Particle Spectrometer (SMPS) setup which are incapable of providing chemical information.[192,195] Therefore, a method, capable of quantifying density, elemental compositions and spatially resolved chemical information together will be ideal to characterize the overall effect of aerosols on different atmospheric processes.

In this study, a unique combination of atomic force microscopy (AFM) and scanning transmission X-ray microscopy (STXM) has been employed to explore mixing state in laboratory generated mixture of glutaric acid and sodium nitrate aerosol particles. The mixture of these two chemical components showed heterogeneous mixing in all the individual submicron particles and hence was ideal for this study. AFM phase images revealed core-shell type of mixing within the particles and STXM images confirmed that the structure has inorganic core and organic shell. Statistically relevant numbers of particles have been analyzed for relative carbon, nitrogen and oxygen content and further data analysis using Beer's law yielded the density and elemental composition of particles on a spatially resolved manner.

5.2 Experimental details: Materials and sample preparation

Particles of mixture of glutaric acid and $NaNO_3$ were generated using constant output atomizer (TSI, Inc., model 3076) from aqueous solutions prepared from reagent-plus-grade chemicals (99.99% purity, Aldrich). All solutions were prepared with deionized water (18 MΩ•cm). The solution concentration for the both of the chemicals was 0.1 M. The generated particles were dried down to ~30% RH in a diffusion dryer (TSI, Inc., model 3062) prior to sizing and substrate deposition using a micro-orifice uniform deposit impactor (MOUDI) (MSP, Inc., model 110). Particles were deposited on Si_3N_4 windows (Silson Ltd., England) mounted on the impaction plate of the seventh stage. The aerodynamic cutoff size of the seventh stage is 0.56 µm. All samples were prepared at room temperature and used within a couple of days after the preparation. Experimental details for STXM and AFM experiments are exactly similar to the density and elemental composition quantification described in Chapter 4. Therefore, please refer to Chapter 4 for the experimental details.

5.3. Result and discussion

5.3.1 AFM images of the particles

Substrate deposited sub-micrometer sized particles of 1:1 molar mixture of glutaric acid and $NaNO_3$ were subjected to atomic force microscopy (AFM) to quantify the thickness and size along with study on particle morphology. Initially, the particle morphology has been examined using AFM height and phase images (Figure 5.1). The particles were perfectly rounded in shape and the size distribution was found to be in the range of ~0.2-1.3 μm from the height image (Figure 5.1a). On the other hand, AFM phase images were acquired to understand the distribution of glutaric acid and $NaNO_3$ in the particle. In the phase imaging, phase lag between the oscillation frequency of cantilever and driver is measured, which can be used to spatially characterize variations in composition, adhesion, friction, and viscoelasticity of the sample.[226-229] Therefore, phase image can spatially distinguish two different chemical components in a particle. The phase image (Figure 5.1b) for our 1:1 glutaric acid and $NaNO_3$ shows sharp discrimination between two components in the center and side of the particle, indicating heterogeneous mixing. Herein, we define the center as core and side of the particle as shell. AFM phase image can only distinguish different type of chemical species but cannot identify chemical substances; hence it is not possible to comment on which compound constitutes the core and which compound constitutes the shell at this point using the AFM phase image.

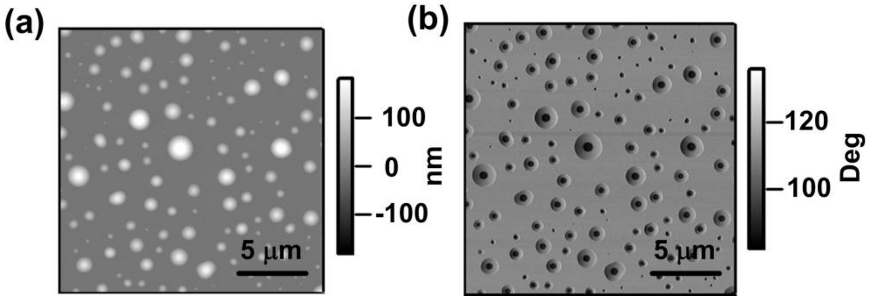

Figure 5.1(a) AFM height image showing morphology of 1:1 mixture of Glutaric acid and $NaNO_3$ particles, (b) AFM Phase indicates presence of two different compound on the surface of each particle in the core and the shell.

5.3.2 NEXAFS spectra and STXM maps

The core-shell structure of the particle prompted us to analyze and compare the NEXAFS spectra obtained from the core of the particles with the spectra obtained from shell. Spectra obtained in C and N-edge for both the core and shell of the particles was similar, owing to the fact that glutaric acid and $NaNO_3$ are the lone source of carbon and nitrogen respectively. Noticeably, a considerable difference in the intensity of N and C containing functional groups has been observed for the core and the shell respectively. Hence, C and N-edge NEXAFS spectra obtained has been averaged over the whole particle and shown in Figure 5.2a, 2b. In C-edge spectra, two resonance transition occurring at 288.54 eV and 290.33 eV were observed, which has been assigned to COOH π^* and CH_2 4p resonance transition respectively (Figure 5.2a).[202,203] In addition, nitrogen NEXAFS shows signature of nitrite and nitrate π^* transitions at 401.66 eV and 405.36 eV respectively (Figure 5.2b).[200,201] Oxygen NEXAFS spectra, averaged over whole particle (core & shell) is shown in Figure 5.2c. In O-edge, π^* transition due to nitrate and –COOH group occurs at 531.8 and 532.2 eV.[200,202] Considering the broadening and spectral resolution, it was not possible to separate the two above mentioned transition. Characteristic broad σ* transitions centered at 538.2 eV and 543.1 eV, corresponding to $1s \rightarrow 3a'_1$ and $1s \rightarrow 4e'$ resonance were observed in the core O edge spectra of the core.[200] The vertical lines in the NEXAFS spectra represent the resonance transition energies used to obtain STXM maps (Figure 5.2a-c). As mentioned earlier in the experimental section, the difference between post and pre edge absorbance signal is proportional to the number of atoms present in the sample. Since, the post edge signals were very low, resonance transition energies at 288. 6 eV (C), 405.3 eV (N) and, 531.8 eV (O) were used to obtain STXM map instead of post edge. Subsequently, the OD obtained from these maps was scaled to the post edge for the quantification of the density and chemical composition which will be discussed in the next section. STXM maps obtained from resonance transition energy and pre edge, for carbon, nitrogen, and oxygen are shown in Figure 5.2d-f respectively. As expected, we observed core-shell structure in STXM maps as well. In these maps, the brighter region corresponds to higher atomic absorbance, indicating relatively major occurrence of a particular atom in the brighter region of the particle. To illustrate, N and O atoms had majority of occurrences in the core of the particle; whereas C atoms were preferably found in the shell. Therefore, predominant occurrence of $NaNO_3$ in the core and glutaric acid in the shell has been confirmed using STXM chemical map as glutaric acid and $NaNO_3$ is the only origin of C and N atoms within the particle.

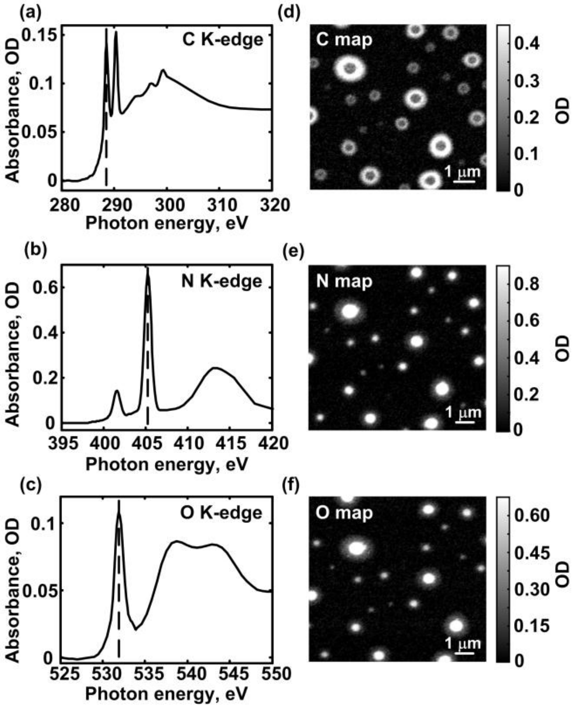

Figure 5.2 NEXAFS spectra averaged over whole particle showing (a) C K-edge, (b) N K-edge and (c) O K-edge. The dashed line in each spectrum shows the transition energy used to obtain the STXM absorption maps, which has been shown in Fig. (d), (e) and (f) for C, N and O edge respectively.

5.3.3 Spatially resolved density and elemental composition

The spatial quantification of density and chemical composition utilizing the AFM height images and STXM maps will be discussed in this section. The approach was to utilize Beer-Lambert's law (Eqn. 1) and plot absorbance at a particular absorption edge as a function of particle thickness and calculate the density from the slope.

$$OD_i = \mu_i \rho_i d \ldots\ldots\ldots\ldots\ldots\ldots\ldots\ldots\ldots\ldots\ldots\ldots\ldots\ldots (1)$$

where *i* is the atom type (*i.e.* C, N or O), OD_i is the total atomic absorbance in units of optical density (*OD*), μ_i is the mass absorption coefficient of the corresponding atom, ρ_i is the density of i^{th} component in the particle, and *d* is the particle thickness. In case of heterogeneous mixing of multiple chemical components, OD at a specific region in the particle at a particular absorption edge will provide the local density of that particular element (e.g. C, N, and O). The OD at different absorption edges (C, N, O) has been measured from the corresponding STXM map. These maps also provide the size of the particle fairly accurately, but particle thickness could not be measured from STXM map. On the other hand, AFM height images (Figure 5.1a) can be used to measure the size and thickness. In this scenario, two possible approaches could be utilized to obtain the particle thickness for the subsequent density quantification. In a direct approach, we can obtain the particle thickness using AFM and then do STXM experiment on the same particle region in order to generate STXM map of the same particle. Alternatively, analyze statistically relevant number of particles and obtain a correlation between the *size vs. thickness* from AFM height images and calculate the thickness of particle by multiplying the size of the particle (from STXM map) with the slope of this correlation. In this way, the laborious part of the experiment to locate the same exact particle measured using AFM could be avoided without affecting the accuracy of the result. Hence, we used the second approach for our work. The approach of combining AFM and STXM measurements could also, in principle, be extended to other submicron particles with regular shape such as spherical or ellipsoidal. The same approach of quantifying the density and elemental composition has been previously reported by our group for thixotropic hydrogel sample.[199] Moreover, recently we have employed similar approach on several laboratory generated particles for the same. Herein, we show how this approach could be extended to examine the mixing state in heterogeneously mixed particles and quantify density and elemental composition in a spatially resolved manner.

The STXM maps in different absorption edges (Figure 5.2) have been used to get an absorbance profile as a function of distance across each particle. A representative shape of the profile obtained from STXM map in C-edge is shown in Figure 5.3a. This profile shows the distribution of carbon containing species, glutaric acid, across the particle. Point 1 in the profile is the exact center of the particle and point 2 represents the region of maximum occurrence of glutaric acid. Hence, local density and chemical composition calculated at point 1 and 2 in the absorbance profile would represent the core and the shell respectively. In order to do that, the thickness of the particle at both the points needs to be measured first. Hence, the distance between the two points of maximum of occurrence of glutaric acid, defined as *core width*, is plotted as a function of size of the particle. The slope of the graph is then multiplied with the size of the particles in AFM height image to calculate the thickness at point 2 (shell, maximum occurrence of glutaric acid) for each particle as shown in Figure 5.3c. Measured thickness at point 1 and 2 is then plotted as a function of size of the particle obtained from the AFM height image (Figure 5.3d). The slope of these two correlations enables us to determine the thickness of the particles studied in STXM absorbance map in both core (point 1) and shell (point 2).

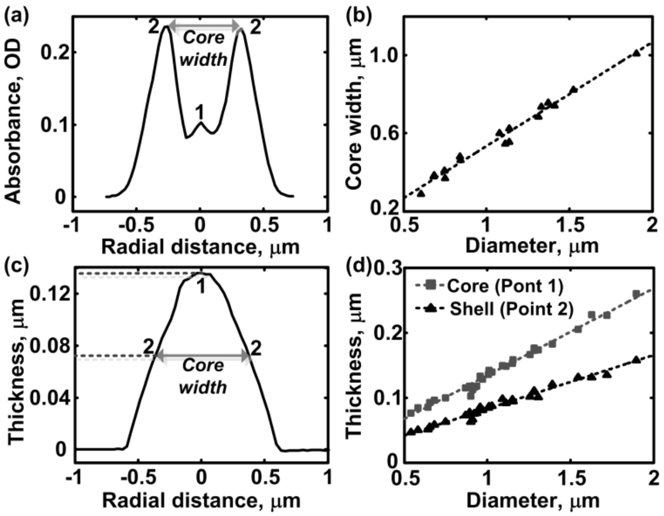

Figure 5.3(a) Spectral profile through the middle of a representative particle in the STXM absorbance map shows maximum occurrence of C at point 2 (Shell) whereas point 1 (Core) is the center of the particle. The distance between the two maximum occurrence points has been defined as core width. (b) Core width, calculated from absorbance maps, is plotted as a function of the diameter of the particle. (c) AFM height profile of similar sized particle. The thickness of point 2 is determined using the slope of the plot in (b). (d) Correlation of thickness as a function of diameter of the particle.

In the final step of this analysis, the thickness of particles studied in STXM absorbance maps (Figure 5.2d-f) has been calculated by multiplying the slope of the correlations shown in Figure 5.3d with the respective size of the particle, followed by a plot of absorbance as a function of both core and shell thickness of the particle (Figure 5.4a, b) for all the absorption edges (C, N, O). According to Eqn. 1, dividing the slope of these graphs by the corresponding mass absorption coefficient, calculated from the atomic scattering factors and determined to be 3.84 x 10^4 and 2.80 x 10^4 and 1.96 x 10^4 cm^2/g for C, N and O, enables us to calculate the atomic density of respective elements. These atomic densities are reported in Table 5.1. Moreover, the molecular formula of the compounds ($NaNO_3$ and glutaric acid) is utilized to calculate total density of the all the materials present in both core and shell. The total density for the core and shell was found to be 1.17 ± 0.08 and 1.28 ± 0.1 g/cc respectively. Hence, the core and shell has nearly similar density with the standard deviations taken into consideration. The bulk density of pure $NaNO_3$ and Glutaric acid is 2.17 and 1.62 g/cc respectively (Sigma Aldrich). Interestingly, the combination of these two compounds creates a heterogeneous mixture with a considerably less density, indicating these particles being porous in nature.

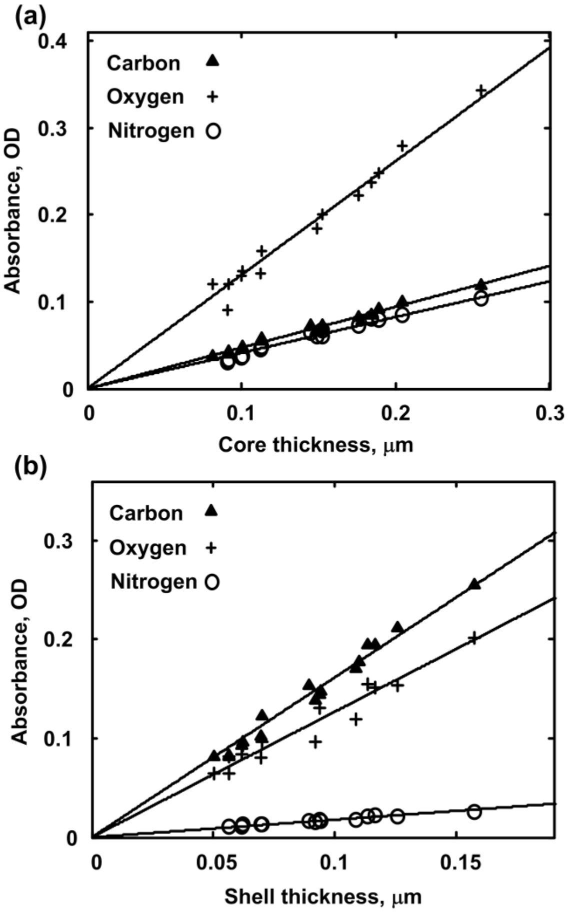

Figure 5.4 Plot of absorbance as a function of (a) core and (b) shell thickness for all the absorption edges, used to calculate the density and elemental composition from the slope of the plots.

Moreover, the elemental composition of the particles has been calculated for both core and shell of the particle by dividing the individual atomic densities by corresponding atomic weight. The experimental chemical composition was found to be 1:1:3.8 and 1:0.13:1.2 (C : N : O) for the core and the shell respectively (Table 5.1). Again, the occurrence of C and N atoms in only glutaric acid and $NaNO_3$ enables us to verify the experimentally determined elemental composition by calculating the expected amount of O atom for a known amount of C and N atoms. These calculated elemental compositions have been in really good coordination with the experimentally determined compositions as shown in Table 5.1. The presence of a little excess oxygen in the core of the particle could be either attributed to presence of water present in the particle core as they have been formed from solution mixture or simply the error in the data analysis.

Table 5.1 Summary of densities and atomic ratios in core and shell of the particle

Region	**C density (g/cc)**	**N density (g/cc)**	**O density (g/cc)**	**Total density (g/cc)**	**Atomic ratio C:N:O**	**$C_5O_4H_8$:$NaNO_3$**
Core	0.12 ± 0 .01	0.14 ± 0.01	0.66 ± 0.06	1.17 ± 0.08	1:1:4 (1:1:3.8)*	1:5
Shell	0.42 ± 0.03	0.06 ± 0.005	0.65 ± 0.06	1.28 ± 0.1	1:0.13:1.2 (1:0.13:1.2)*	1:0.65

Asterisk (*) shows the expected atomic ratios calculated from C/N ratio

5.4 Conclusion

This unique approach can be utilized to calculate the spatial distribution of compounds in a particle of multicomponent heterogeneous mixture. More specifically, this approach allows us to quantify local elemental composition and density within a particle. Hence, this method will be important to analyze the effect of mixing on different physical properties such as scattering of solar radiation, cloud condensation etc. for complex atmospheric aerosol particles. Moreover, this method could be extended to micrometer or sub-micrometer sized crystals or other multicomponent substances to quantify spatially resolved density and elemental composition.

CHAPTER 6

SPECTROSCOPIC EVIDENCE OF KETO-ENOL TAUTOMERISM IN DELIQUESCED MALONIC ACID PARTICLES

6.1 Introduction

Organic compounds are ubiquitous in the atmosphere.[230-232] They have been found in various sources such as fog and rain water, ice water, gas phase, and aerosols.[233-240] In particular, organic aerosols (OA) play vital role in different atmospheric reactions and physicochemical processes along with the direct and indirect effects on the Earth's climate.[113,230,231,241,242] Carboxylic acids and low-molecular weight dicarboxylic acids such as oxalic, malonic, glutaric, succinic acid, are abundant in atmospheric OA.[243] Due to their high polarity, dicarboxylic acids are readily soluble in water and show efficient deliquescence and water uptake properties, thus can strongly alter the hygroscopic properties of other inorganic aerosols in a mixed state.[128,225,244,245] More importantly, changes in chemical structure or composition due to water uptake can potentially impact atmospheric chemistry and reactivity of deliquesced OA particles.[111,112]

Malonic acid has been reported as an abundant component of atmospheric OA.[246] In fact, it is the second most abundant dicarboxylic acid in the atmosphere, ubiquitous over oceans and urban areas.[246] Malonic acid is the subject to keto-enol tautomerism (Figure 6.1), whereas the keto form dominates equilibrium in aqueous solutions. The upper limit for the keto-enol equilibrium constant of malonic acid has been estimated as 10^{-4}.[247] Therefore, concentration of the enol form of malonic acid in micro droplets of fog and cloud is negligible. However, recent theoretical study by Yamabe *et al*[248] showed that tautomerization may proceed through a complex intramolecular transition state involving a malonic acid and six water molecules, as opposed to a direct unimolecular mechanism of the keto-to-enol proton shift. Therefore, the keto-enol equilibrium of malonic acid might be different for highly concentrated deliquesced particles where such an intramolecular, concerted mechanism can be effective. To the best of our knowledge, the aspect of keto-enol tautomerization in submicron deliquesced malonic acid particles has never been studied before, and this is the subject of the present work.

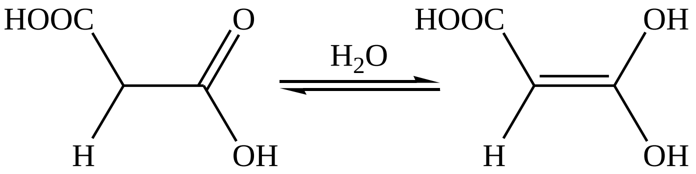

Figure 6.1 Keto-enol tautomerism of malonic acid in the presence of water vapor.

In this study, we apply Scanning Transmission X-ray Microscopy coupled with Near Edge X-ray Absorption Fine Structure Spectroscopy (STXM/NEXAFS), and optical microscopy combined with Fourier Transform Infrared Spectroscopy (micro-FTIR) to study at different relative humidity (RH) the hygroscopic behavior and chemical transformations of malonic acid particles deposited on a substrate. Changes in the carbon and oxygen K-edge NEXAFS and FTIR spectra were used to quantitatively determine the equilibrium water-to-solute ratio as a function of RH. We report spectroscopic evidence of substantial keto-enol tautomerism in deliquesced malonic acid particles, with equilibrium shifted towards the enol product as RH increases. We determine the equilibrium constants of the keto-enol tautomerization based on quantitative analysis of

NEXAFS spectra acquired at different RH from the same individual particle of malonic acid.

6.2 Experimental details

All the experimental details including the sample preparation is exactly same as Chapter 2 and Chapter 3. Please refer to experimental section of Chapter 2 for the details of STXM experiments and Chapter 3 for the details about micro-FTIR experiments.

6.3 Result and discussion

6.3.1 STXM image of malonic acid particles

Malonic acid particles were exposed to increasing relative humidity (RH) to explore their hygroscopic and chemical properties. In STXM/NEXAFS experiments, individual particles with different sizes have been studied and showed similar results. Figure 6.1a, b show the total oxygen maps of the same particle at the lowest (~2%) and highest (90%) RH. The oxygen maps are obtained by subtracting the preedge optical density (OD) image from the postedge OD image. The initial size of the particle at ~2% RH was 2.3 μm^2. With the increasing exposure to water vapor, the particle started to take up water and grew in size to 2.9 μm^2 at 90% RH. The maximum absorbance value in the oxygen map (Figure 6.1) that corresponds to an approximate center of the particle has increased from 0.33 to 0.65 OD between RH of ~2% and 90%, respectively.

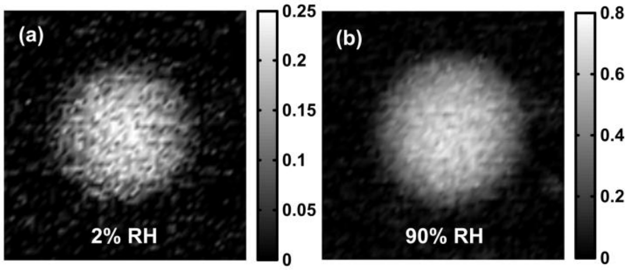

Figure 6.2 Total oxygen maps (scan size is 4 μm x 4μm) of a representative malonic acid particle at ~2% RH (a) and 90% RH (b).

6.3.2 Hygroscopic properties of malonic acid

Total oxygen maps acquired at different RH are used to quantify the mass of water and water-to-solute ratio (WSR) on a single particle basis. Detailed description of the method to quantify mass of water using STXM on a single particle basis has been reported elsewhere,[31] and thus will be described only briefly here. To determine the mass of water quantitatively on a single particle basis, we employ an averaged cross-sectional analysis of the *O* maps recorded at different RH over the particle. In order to relate the cross-sectional measurements to the *O* mass analysis, two assumptions are used: particle shape is a half-ellipsoid and the density of water inside the particle is homogeneously distributed within the particle. Based on the equation of a standard axis-aligned half-ellipsoid in an xyz-Cartesian coordinate system and using the assumptions above, the mass of *O* atoms within a particle can be calculated using the following equation:[31]

$$m_O = \frac{4}{9}\frac{\Delta x \Delta y \langle OD_{max} \rangle}{\mu} \dots\dots\dots\dots\dots\dots\dots\dots\dots\dots\dots\dots\dots\dots\dots\dots (1)$$

where m_O is the mass of water, Δx and Δy are the two full widths at half maximum (FWHM) recorded from the averaged horizontal and vertical cross-sectional profiles of a total *O* map at a particular RH value. The horizontal and vertical cross-sections are measured along the two main axis of the particle that lies within a substrate plane. $\langle OD_{max} \rangle$ is the maximum averaged total O absorbance in units of optical density and μ is the difference in mass absorption coefficients for atomic O between 550 eV and 525 eV. The difference in mass absorption coefficients is calculated from the atomic scattering factors and found to be 1.96×10^4 cm^2/g.[31] If particles have O atoms in their molecular formula, as in the case of malonic acid, then the O absorbance maps and Eq. 1 can be used to determine the initial amount of the solute, hence allowing us to quantify WSR for an individual submicrometer particle as a function of RH. We previously demonstrated the accuracy of this approach for sodium nitrate particles with excellent literature agreement for the plots of the WSR as a function of RH.[31]

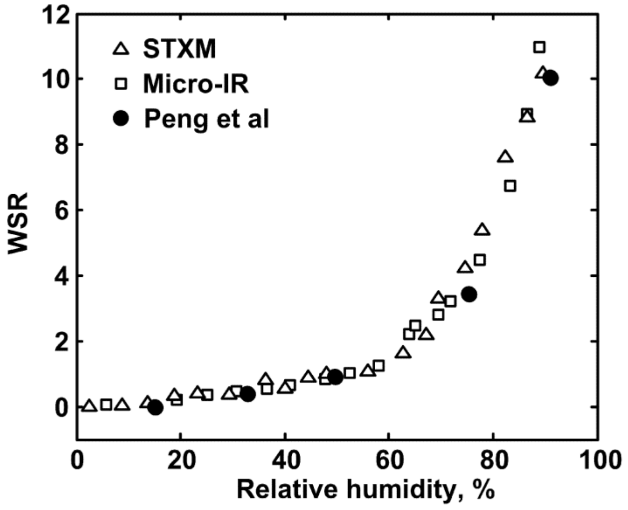

Figure 6.3 Plot of the water-to-solute (WSR) as a function of RH for malonic acid obtained from our STXM (△) and micro-FTIR (□) data sets, as well as the literature result from Peng et al.[127]

Using the cross-sectional analysis and Eq. 1 described above, determined WSR values of the malonic acid particle are plotted as function of RH (Figure 6.2, triangles).

Here, WSR value of approximately 3 at ~2% RH was subtracted to enable the comparison with the micro-FTIR and literature data sets. The non-zero WSR value indicates the particle was not fully dehydrated and retained water even at such low humidity. Complementary analysis by micro-FTIR spectroscopy has been also performed over identical sample of malonic acid particles. Figure 6.3a shows the FTIR spectra of malonic acid particles recorded at different RH. Detailed IR spectra for the region of 810-1800 cm^{-1} and assignments of the specific vibration modes are shown in Figure 6.3b with the peak assignment summarized Table 6.1. Different modes for CH_2, *COOH* and *OH* functional groups are assigned according to the literature.[177-179,249,250] Two well-defined bands that correspond to the free $C{=}O$ stretching (1730 cm^{-1}) and $C{=}O$ associated with intermolecular hydrogen bonds (1690 cm^{-1}) are also observed in the spectrum.[249] Upon an increase in RH, peaks broadening and red shifts of malonic acid bands are observed, typical for particle hydration experiments.[125,171] Condensed-phase water starts to appear at ~70% RH without a sharp deliquescence phase transition, followed by a continuous water uptake at higher RH. The integrated peak area (between 3660 to 2750 cm^{-1}) of the hydroxyl stretching band (peak maximum ~3400 cm^{-1}) of the FTIR spectra is used to calculate WSR according to the literature.[171] The equation used to calculate the WSR is as follows

$$WSR_{FTIR} = \frac{n_{water}}{n_{malonic}} = \frac{\bar{\sigma}(malonic) \times \bar{A}(OH)}{\bar{A}(malonic) \times \bar{\sigma}(OH)} \ldots\ldots\ldots\ldots\ldots\ldots\ldots\ldots\ldots\ldots\ldots\ldots\ldots (2)$$

where n_{water} and $n_{malonic}$ are the number of water and malonic acid molecules, respectively. $\bar{A}(OH)$ and $\bar{A}(malonic)$ are the experimental integrated absorbances of malonic acid particles for $\nu(H_2O)$ band (3660-2750 cm^{-1}) and $\nu(COOH)$ band (1200-1500 cm^{-1}), respectively. An attenuated total reflectance Fourier transform infrared (ATR-

FTIR) spectroscopy (Thermo Scientific; Nicolet 470/670/870) was utilized to study aqueous solutions of malonic acid of known concentrations to determine the absorption cross section for the $COOH$ group in malonic acid of $\bar{\sigma}(malonic)$ = 3.8 × 10^{-17} cm•molecule^{-1}.[171] The absorption cross-section for ν(H_2O) band was taken as $\bar{\sigma}(OH)$ = 1.07 × 10^{-16} cm•molecule^{-1}.[251] To remove an initial water contribution to the WSR values, the FTIR spectrum at ~2% RH has been subtracted from the spectra at higher humidity. Hence, the relative WSR results are reported, similar to the STXM data set above, which facilitates their direct comparison. Figure 6.2 shows the WSR plot determined using micro-FTIR results as a function of RH (squares), which is essentially identical to the hygroscopic growth curve determined by STXM. In addition, results from particle levitation experiment of Peng *et al*[127] are also shown in Figure 6.2 (filled circles). As can be seen, all three data sets very closely follow each other. The observed overlap is significant as it validates our single particle STXM measurements against hydration growth values obtained in other experimental techniques.

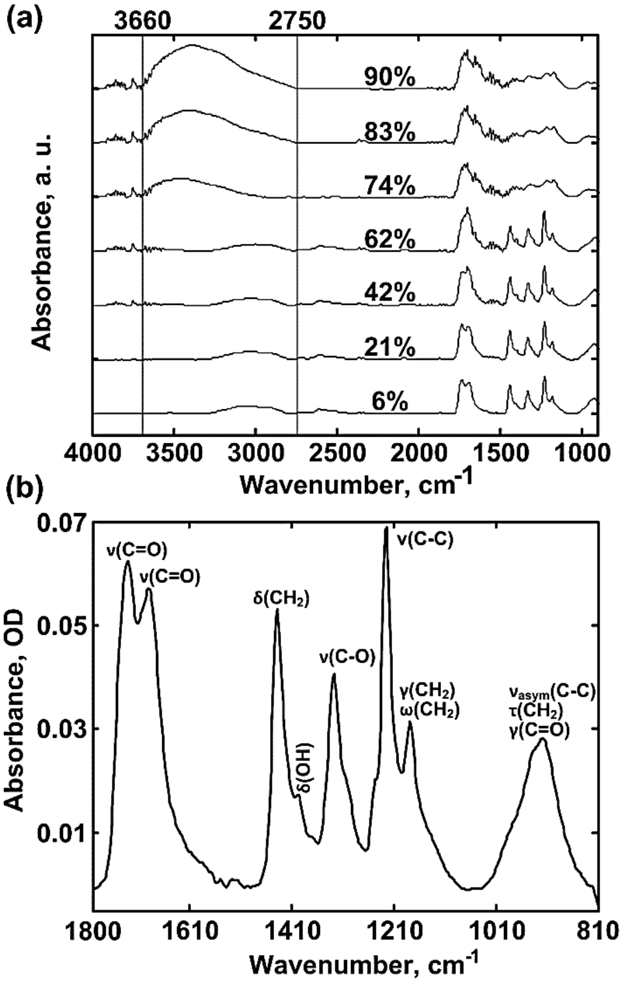

Figure 6.4(a) FTIR spectra of malonic acid particles as a function of RH, showing an increase in the hydroxyl stretch band as RH increases. Two vertical lines at 3660 and 2750 cm^{-1} indicate the integration range used to quantify the hydroxyl peak area for the WSR calculation. (b) Detailed FTIR spectrum of malonic acid particles at ~2% RH within the region of 810-1800 cm^{-1}. Numbers correspond to specific vibration modes with the assignment summarized in Table 6.1.

Table 6.1 Main infrared bands and assignment for malonic acid particles at ~2% RH.

Band (cm^{-1})*	**Assignment****	**References**
925	ν_{asym}(C-C) + τ(CH_2) + γ(C=O)	177,179
1175	γ(CH_2) + ω(CH_2)	179
1225	ν (C-C)	179
1320	ν(C-O)	177,178
1400	δ(OH)	177-179
1445	δ(CH_2)	177
1690	ν(C=O)	177,249
1730	ν(C=O)	177,178,250

*Bands are as shown in Fig. 3b; **ν - stretching, δ - bending, τ – torsion, γ – rocking.

6.3.3 Changes in IR spectra of malonic acid particles

The micro-FTIR data set provides qualitative information that supports the equilibrium of the tautomerism reaction (Figure 6.1) in the deliquesced malonic acid particles is shifting towards the enol form as RH increases. The RH-dependent changes in the malonic acid bands during hydration experiment can be identified by subtracting the spectrum at ~2% RH from spectra at the higher RH. Obtained difference spectra for several selected RH are shown in Figure 6.4. The positive change in the absorbance of a particular band is indicative of an increase in the corresponding number of functional groups and *vice versa*. A clear decrease in the signal of IR bands characteristic of the keto form is evident from the data. Specifically, the negative peaks $\tau(CH_2)$ at 940 cm^{-1}, $\gamma(CH_2)$ + $\omega(CH_2)$ at 1175 cm^{-1} and $\delta(CH_2)$ at 1445 cm^{-1} in the difference spectra indicate diminishing of the methylene ($–CH_2$-) groups.[177,249] Negative peak $\nu(C\text{-}C)$ at 1225 cm^{-1} is due to the decrease in the carbon-carbon single bond, while negative peaks $\nu(C{=}O)$ at 1690 cm^{-1} and 1730 cm^{-1} correspond to the decrease in the number of *COOH* groups.[177-

[179,249,250] All these changes are consistent with the keto-enol equilibrium shifting towards the enol form as RH increases. Series of positive peaks in the region of 1620-1680 cm^{-1} can be attributed to an increase in the number of *C=C* groups[252] in enol as humidity increases, consistent with the expected equilibrium shift. However, we note the observed increase is not quantitative due to the presence of rotational fine structure of water[253] in the same region that would also give a positive signal as humidity increases.

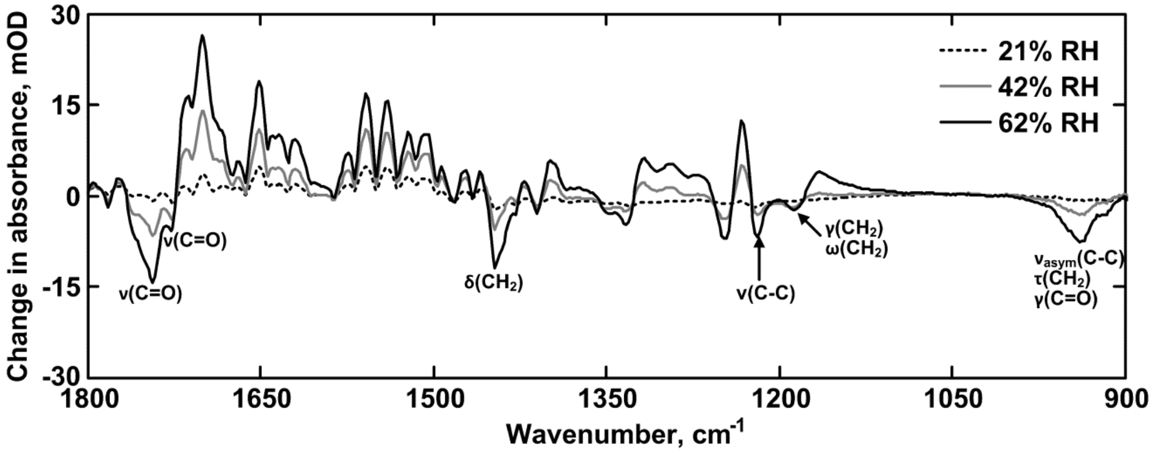

Figure 6.5 Difference FTIR spectra of malonic acid particles at three selected RH (21, 42, 62%) obtained by subtracting the spectrum at ~2% RH from every spectra. Numbers correspond to specific vibration modes with the assignment summarized in Table 6.1.

6.3.4 Solution phase FTIR spectra of supersaturated malonic acid

Solubility of malonic acid in water is ~0.21 in the unit of mole fraction which corresponds to ~3.8 WSR at 25°C.[204] Therefore, we were interested in examining the similar tautomerism reaction in solution phase at concentrations comparable to WSRs in the particulate state described in the previous section. Accordingly, malonic acid solutions of 1M, 4.3M, 12M, 15.5M concentrations have been prepared, corresponding to 55.5, 12.9, 4.6, and 3.6 WSR respectively. The ATR-FTIR spectra of these samples are shown in Figure 6.5. All the specific transitions due malonic acid have been observed in all four different concentrations except one transition at ~1620 cm^{-1}. This peak was attributed to the formation of $C=C$ due to formation of enol in the keto-enol tautomerism reaction as the peak for $C=C$ transition occurs traditionally in between 1620-1680 cm^{-1} for unsaturated carboxylic acids.[252,254] This transition have been found for the solutions of 12.9, 4.6 and 3.6 WSRs; whereas it was absent for the solution with 55.5 WSR, supporting same keto-enol tautomerism reaction for the highly concentrated solutions. Moreover, ratio of the intensity of $C=C$ transition to $COOH$ transition (~1720 cm^{-1}) will be a direct indication of the efficiency of the keto-enol tautomerism reaction. The peak ratio reported in Figure 6.5 indicates that the reaction shifts most towards the product at 12.9 solution WSR, which in turn corresponds to 90% RH in the particulate state. This result further verifies the existence of the tautomerism reaction. Therefore, quantifying equilibrium constant at different WSRs would directly provide us the measure of equilibrium shift towards the product in the tautomerism reaction. As FTIR data is not quantitative enough to measure the equilibrium shift in the tautomerism reaction in deliquesced malonic acid particles, we present STXM/NEXAFS results that not only support these observations but can also be used to quantify the keto-enol equilibrium constant and how it changes as a function of RH in the next section of this report.

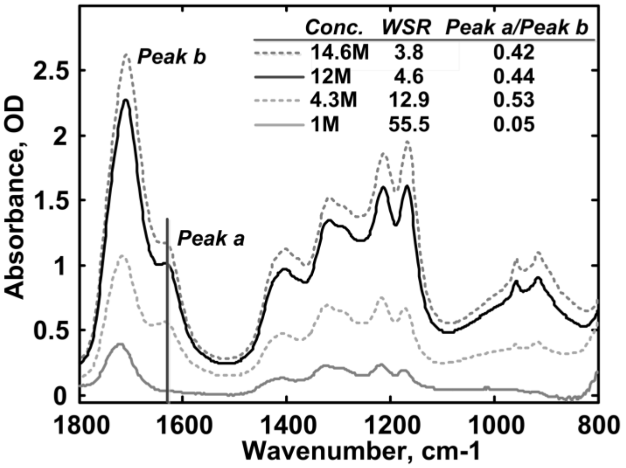

Figure 6.6 Solution phase ATR-FTIR spectra of malonic acid at similar concentrations as particulate state WSRs. *Peak a* (~1620 cm^{-1}), assigned to *–C=C-* resonance, has been observed in comparable solution phase concentrations as particulate state WSRs. *Peak b* (~1720 cm^{-1}) was assigned to be *–COOH* resonance. Therefore, ratio of *peak a/peak b* at a particular concentration will be a measure of the tautomerism reaction towards the enol form.

6.3.5 RH dependent NEXAFS spectra showing the existence of keto-enol tautomerism

To determine the chemical changes in the deliquesced malonic acid particles, near edge X-ray absorption fine structure spectra (NEXAFS) at carbon (280-320 eV) and oxygen (525-550 eV) K-edge were measured. Figure 6.6 shows carbon (a) and oxygen (b) K-edge NEXAFS at three selected RH for the single particle shown in Figure 6.1. For all spectra, the corresponding constant pre-edge absorbance was subtracted to facilitate the comparison. Several conclusions are apparent from these data. First, the total carbon absorbance (320 - 280 eV) remains unchanged as humidity increases. The absence of a change is expected since the number of malonic acid molecules inside the particle should remain constant. On the other hand, the total oxygen absorbance (550 – 525 eV) clearly increases with an increase in RH, which is due to continuous water uptake by the malonic acid particle. Additional spectroscopic insights can be obtained by closely examining the peak intensities of different functional groups. Prior to adding water vapor (~2% RH), single particle *C* edge spectrum (Figure 6.6a) shows two distinct transitions at 288.6 and 290.4 eV that correspond to *COOH* π^* and CH_2 *4p* resonances, respectively.[202,203] *O* edge spectrum (Figure 6.6b) also shows well defined *COOH* π^* resonance at 532.5 eV and a broad σ^* resonance around 540 eV.[202] Comparison of the spectra at ~2%, 50% and 90% at both *C* and *O* K-edges shows a decrease in the absorbance of *COOH* group (288.6 eV in *C* edge and 532.5 eV in *O* edge) and CH_2 (290.4 eV) resonance with increasing RH. Moreover, a peak at 285.1 eV and shoulder at 287.3 eV clearly increase with increasing RH. These peaks are assigned to *C=C* and *C-OH* resonances, respectively.[202,255] The observed chemical changes, similar to the micro-FTIR data set, are consistent with the keto-enol tautomerism of malonic acid (Figure 6.1), and indicate substantial shift of the equilibrium towards the enol product formed in deliquesced particles at higher RH.

6.3.6 Calculation of RH dependent equilibrium constant

Prior to quantifying the equilibrium constant for the tautomerism reaction using the STXM/NEXAFS data, the possibility of X-ray damage during STXM measurements that can lead to the observed chemical changes needs to be discussed. We have several arguments that suggest the changes observed are not due to the radiation damage. First, STXM/NEXAFS results are consistent with the independent micro-FTIR data presented above, which is not affected by the radiation damage. Second, STXM experiments were repeated under various extents of X-ray exposure and similar *C* and *O* K-edge spectra were observed. We note a report by Wang *et al*,[256] where continuous X-ray exposure of a thin polymeric film resulted in the chemical changes similar to those observed here.

However, the radiation dose used in the present work was calculated to be ~1000 times lower than the dose used in the work by Wang *et al* to observe the chemical changes within a polymer film. Thus, the combined evidence presented strongly support the observed changes in the *C* and *O* K-edge NEXAFS spectra do not originate from the X-ray damage.

To determine the equilibrium constant of keto-enol tautomerization, we use changes in the intensity of the *COOH* peak at both *C* and *O* edges and *C*=*C* peak at *C* edge recorded at three different RH (~2%, 50% and 90%). The number of particular functional groups is directly proportional to the corresponding peak intensity in the NEXAFS spectrum with the coefficient of proportionality that includes the mass absorption coefficient for this transition.[50,58] Since the mass absorption coefficients for the *COOH* and *C*=*C* transitions are not available, we instead utilize available literature values for the oscillator strength of corresponding resonances because both coefficients are directly proportional to each other.[257] The oscillator strength of *COOH* resonance for the keto and enol forms of malonic acid are assumed to be the same as for the *COOH* transition of acetic and acrylic acids, respectively. The basis for this assumption is structural similarity of these compounds to two forms of malonic acid. Based on the available literature values,[203] the oscillator strength of the *COOH* transition in the *C* K-edge is $E_{keto}^{C}(COOH)$ = 8.8 x 10^{-2} eV^{-1} for the keto form and $E_{enol}^{C}(COOH)$ = 6.3 x 10^{-2} eV^{-1} for the enol form. The oscillator strength of the *COOH* transition at the *O* K-edge is $E_{keto}^{O}(COOH)$ = 2.3 x 10^{-2} eV^{-1} and $E_{enol}^{O}(COOH)$ = 1.5 x 10^{-2} eV^{-1} for the keto and enol forms of malonic acid, respectively.

The initial number of malonic acid molecules inside the particle that includes both the keto and enol forms is defined as n_{tot}, while the number of molecules in the enol form at a particular RH is Δn_{RH}. Then, the number of molecules in the keto form at the corresponding RH is (n_{tot} - Δn_{RH}). Based on the Beer-Lambert's law, the *COOH* absorbance at a particular RH ($A_{RH}^{C}(COOH)$) is directly proportional to the number of *COOH* groups that originate from the keto and enol forms of the malonic acid. Therefore, by multiplying the number of *COOH* groups of both the enol and keto forms with the corresponding oscillator strength, and taking into account two *COOH* groups per single molecule in the keto form and one *COOH* group for the enol form, the *COOH* absorbance at a particular RH can be expressed by the following equation:

$$A_{RH}^{C}(\mathrm{COOH}) = \chi[2(\mathrm{n_{tot}} - \Delta\mathrm{n_{RH}})E_{keto}^{C}(COOH) + \Delta\mathrm{n_{RH}}E_{enol}^{C}(COOH)] \text{……….}(3)$$

where χ is humidity-independent constant that accounts for the size of the particle and includes the coefficient of proportionality between the oscillator strength and mass absorption coefficient.

Next, by dividing Eq. 3 for ~2% RH by that at either 50% or 90% RH, we obtain:

$$\frac{A_{2\%}^{C}(\mathrm{COOH})}{A_{RH}^{C}(\mathrm{COOH})} = \frac{[2(\mathrm{n_{tot}}-\Delta\mathrm{n_{2\%}})E_{keto}^{C}(COOH)+\Delta\mathrm{n_{2\%}}E_{enol}^{C}(COOH)]}{[2(\mathrm{n_{tot}}-\Delta\mathrm{n_{RH}})E_{keto}^{C}(COOH)+\Delta\mathrm{n_{RH}}E_{enol}^{C}(COOH)]} \text{…………}(4)$$

The number of the enol-form malonic acid molecules at 50% or 90% RH (Δn_{RH}) is directly proportional to the absorbance of the *C=C* peak, their ratio to that at 2% RH is

$$\frac{\Delta n_{2\%}}{\Delta n_{RH}} = \frac{A_{2\%}(C=C)}{A_{RH}(C=C)} \text{………………}(5)$$

To simplify further derivations, the following new parameters are defined:

$$\alpha^{C} = \frac{E_{keto}^{C}(COOH)}{E_{enol}^{C}(COOH)};\ \beta_{RH} = \frac{n_{tot}}{\Delta n_{RH}};\ \gamma_{RH} = \frac{\Delta n_{2\%}}{\Delta n_{RH}};\ \delta_{RH}^{C} = \frac{A_{2\%}^{C}(\mathrm{COOH})}{A_{RH}^{C}(\mathrm{COOH})} \text{…………………..}(6)$$

Then, after writing Eq. 3 for 2%, 50% and 90% RH, both sides of the equation for 50% and 90% RH were divided by the corresponding sides of the equation at 2% and, after a few derivations, the parameter β_{RH} can be expressed as:

$$\beta(\alpha,\delta,\gamma) = \frac{n_{tot}}{\Delta n_{RH}} = \frac{\left(1-\frac{1}{2\alpha}\right)(\delta-\gamma)}{(\delta-1)}\beta_{RH} = \frac{\left(1-\frac{1}{2\alpha^{C}}\right)(\delta_{RH}^{C}-\gamma_{RH})}{(\delta_{RH}^{C}-1)} \ldots\ldots\ldots\ldots\ldots\ldots\ldots (7)$$

Finally, the equilibrium constant can be described in terms of the parameter β_{RH} as:

$$K_{RH} = \frac{\Delta n_{RH}}{n_{tot}-\Delta n_{RH}} = \frac{1}{\beta_{RH}-1} \ldots\ldots\ldots\ldots\ldots\ldots\ldots\ldots (8)$$

Using Eq. 7 and experimental results for the absorbances of the *C=C* and *COOH* transitions at the *C* K-edge, we determine β_{RH} values at 50% and 90% RH. Substitution of the corresponding β_{RH} values in Eq. 8 provides the keto-enol equilibrium constant at these two RH. The equilibrium constant at 2% RH can be obtained by combining Eq. 6 at ether 50% or 90% RH and the corresponding γ_{RH} parameter, resulting in

$$K_{2\%} = \frac{1}{\frac{\beta_{RH}}{\gamma_{RH}}-1} \ldots\ldots\ldots\ldots\ldots\ldots\ldots (9)$$

Hence, by using determined β_{RH} and γ_{RH} values at 50% or 90% RH, the same value for the equilibrium constant at ~2% RH is expected and was indeed observed, as shown below. Additionally, since we can also quantify the number of *COOH* functional groups using the *COOH* π^* resonance at 532.5 eV at the *O* K-edge, derivations similar to above can be performed to obtain the equilibrium constant at 2%, 50% and 90% RH using the measured absorbances of the *C=C* and *COOH* transitions at the *C* and *O* K-edges, respectively. Specifically, Eq. 3-9 will be identical to above with the exception of replacing the superscript “*C*” with “*O*” to reflect different oscillator strength of the *COOH* transition at the *O* K-edge relative to that at the *C* K-edge.

Two independent sets of the keto-enol tautomerism reaction equilibrium constants at 2%, 50% and 90% RH determined using the measured NEXAFS absorbances for: 1) the *C=C* and *COOH* transitions at the *C* K-edge, and 2) the *C=C* at the *C* K-edge and *COOH* at the *O* K-edge are summarized in Table 6.2. We note that while both sets of equilibrium constants are fairly similar to each other, the constants determined from the *C=C* and *COOH* absorbances in the *C* K-edge are systematically lower than that from both *C* and *O* K-edges. The deviation is due to the systematic overestimation of the number of *COOH* groups based on the absorbance measurements of the *COOH* resonance (288.6 eV) in the *C* K-edge spectra, which is close to the ionization potential of carbon (~290 eV, K-edge).[244] The ionization step provides an additional absorbance value at the 288.6 eV which results in overestimation of the number of *COOH* groups, which in turn leads to the observed systematic deviation between the two independent sets of equilibrium constants. Since the *COOH* resonance at the *O* K-edge (532.5 eV) is sufficiently far away from the ionization potential of oxygen (~537.5 eV),[258] its contribution to the measured absorbance of *COOH* transition at this edge is negligible. Therefore, the equilibrium constants determined using the combination of both *C* and *O* K-edge spectra (left column in Table 6.2) are more accurate than those determined using only *C* K-edge data (right column in Table 6.2).

Table 6.2 Equilibrium constants at different RH determined from absorbance of COOH transition from both C and O K-edge NEXAFS spectra and C=C absorbance from C K-edge NEXAFS spectra.

RH	Equilibrium constants determined using O edge COOH and C edge C=C	Equilibrium constant determined using C edge COOH and C edge C=C
~2%	0.18 ± 0.03	0.15 ± 0.03
50	1.1 ± 0.15	1 ± 0.20
90	2.3 ± 0.4	2.2 ± 0.4

The equilibrium constants of 0.18 ± 0.03, 1.1 ± 0.15 and 2.3 ± 0.4 were determined for ~2%, 50% and 90% RH, respectively (Table 6.2, left column). These results provide a clear evidence for the substantial keto-enol tautomerism in deliquesced malonic acid particles, significantly larger than the equilibrium constant of $\sim10^{-4}$ typical of aqueous solutions of malonic acid of usual concentration (e.g 1M).[247] Additionally, the equilibrium is shifted towards the enol product as RH increases. We note the equilibrium constant of a fully dehydrated malonic acid is expected to be less than 10^{-4}.[247] However, as was discussed above using STXM data, the particle at ~2% RH still retained some amount of water (~3 WSR), hence nonzero value of equilibrium constant is observed.

The keto and enol forms of malonic acid show different stability in gaseous and liquid phase. The enol form is predominant in the gas phase whereas the equilibrium shifts towards the keto form in dilute solution as the solvent polarity increases leading to the stabilization of the keto form.[248] However, experiments with the solution of very high concentrations, which falls in the range of the WSRs for the particulate state, showed the existence of C=C group and hence prove the existence of the same tautomerism reaction. Similarly, our results also indicate a substantial shift towards the enol form for the deliquesced malonic acid particles, clearly proving that the origin of the observed shift lies in the limited number of water molecules per malonic acid molecule. According to the theoretical work by Yamabe *et al*,[248] an intramolecular mechanism of keto-enol tautomerism is predicted with limited number of water molecules around a single malonic acid molecule, consistent with our results. Additionally, the activation energy of the transition state for the keto-enol tautomerism was predicted to be the lowest when single malonic acid molecule is hydrogen-bonded to six water molecules,[248] which in turn corresponds to the WSR of 6. The fact that the range of WSR is between 3 to 14 supports the theoretical calculation by Yamabe *et al*.[248] At this point one can expect to have a maximum equilibrium constant at WSR of 6. But, that would only be possible if we would have had a proper deliquescence phase transition like usual inorganic aerosol particles; instead we observed continuous uptake of water for malonic acid. Therefore, we can reasonably expect a slight increase in the equilibrium constant on going from 50% to 90% RH, which is also evident from the solution phase measurements (Figure 6.5). Furthermore, as discussed previously, the difference IR spectra in Figure 6.4 show a decrease in the peaks at 1730 and 1690 cm^{-1} that correspond to free and hydrogen bonded ν(CO) bands, respectively. This observation provides additional evidence that supports the intramolecular keto-enol tautomerization mechanism in deliquesced malonic acid particles.

6.3.7 Environmental implication

The effect of shifted equilibrium towards the enol form in the deliquesced particles as described here is novel, and likely is not unique only for malonic acid. Similar intermolecular mechanisms and elevated concentrations of enol tautomers may be relevant to a range of carboxyl and carbonyl containing species present in atmospheric

OA particles. In fact, we have observed with our initial experiments that similar effect exists for Fulvic acid and biomass burn tarballs. Enols are important intermediates in aqueous chemistry leading to formation of low volatility SOA products through reactions of acid catalyzed esterification, hemiacetal formation, aldol condensation, and organosulfates (sulfur esters) formation.[259] These reactions are considered to have secondary importance in cloud and fog droplets, while reactions of OH radicals with dissolved organics tend to be faster and produce more low volatility SOA products. However, in highly concentrated deliquesced particles reactions through enol intermediates may be a major source of multifunctional, high-molecular weight humic-like substances. Since the keto-enol tautomerization is very fast and both forms are effectively equilibrated, the rates of the products formation will be proportional to concentration of the enols which might be unexpectedly high at aerosol relevant concentrations. At present, formation of SOA is underestimated[260] by major atmospheric chemistry models as compared to field measurements. Our results indicate that elevated concentrations of enols in deliquesced particles may be of substantial importance for improving the modeling predictions.

6.4 Conclusion

In this work we report the hygroscopic and chemical properties of fine malonic acid particles. Significant changes in the chemical structure of malonic acid particles have been observed as a function of relative humidity and also verified with bulk solutions of similar WSRs. Specifically, methods of NEXAFS and FTIR spectroscopy have been used to identify and quantify the formation of enol tautomer of malonic acid (1,1-dihydroxy propenoic acid) with increasing relative humidity. NEXAFS spectra at different RH were used to calculate the equilibrium constant of the tautomerism reaction at three different relative humidity and found to be in the order of ~10^{-1} which is approximately four orders of magnitude higher than that observed in the bulk dilute solutions. Thus, the existence of the enol form malonic acid in atmospherically relevant particles is established and relevant effects of this finding to the atmospheric SOA chemistry are proposed. Our results suggest that the keto-enol tautomerization equilibrium at aerosol relevant concentrations may be substantially different from that reported for the unsaturated aqueous solutions. This finding warrants further studies on the keto-enol equilibrium of other organic acids present in deliquesced OA particles.

CHAPTER 7

TUNING MECHANICAL PROPERTIES OF ORGANIC CO-CRYSTALS IN NANOSCALE

7.1 Introduction

7.1.1 Organic materials in device applications

Silicon based devices such as chips,[261,262] display technology[263,264] and microcircuits[265,266] have been used since last half of 20th century. Integrated circuits, built up from many silicon devices (such as transistors and diodes) on a single chip, control everything from cars to telephones.[267] The thirst for cheaper electronic memory, and faster and more powerful processors, is still not satisfied. It has been predicted that 2012 will see silicon based devices reaching its fundamental physical limit.[268] Therefore, lot of energy and research has been put forward to find an alternative. One of the most promising materials is organic materials. It has been reported that flexibility and light weight of organic materials has a significant advantage over silicon in terms of designing solar cells.[269,270] The cost effectiveness of organic materials is another factor in building micro devices.[271] Moreover, optical light emitting diode (OLED) display is significantly brighter and thinner with wider viewing angle compared to other displays.[272] Hence, organic materials are considered to be an alternative in recent past.

7.1.2 Structure property relationship and solid state reactivity

Complete understanding of structure and property relationship of organic solids is necessary for rational design of organic devices.[64,273] For example, understanding of physical and intermolecular phenomenon in the context of crystal engineering is essential in order to design molecular electronics.[274] Solid state reactivity of organic solids has been particularly of interest especially that undergoes single-crystal-to-single-crystal (SCSC) reaction.[79,275] Potential applications of these materials are currently realized in pharmaceutical and materials science,[82,276,277] supramolecular synthesis[81] and other organic devices.[85,86] However, the rarity of materials undergoing SCSC reaction has limited these applications. Changes in molecular structure on solid state photoreaction invariably results in accumulation of stress and strain that causes the crystals to crack.[278] Therefore, it's important to explore the relationship of solid state reactivity and the structure of organic solids.

Li *et al* reported design of thermally stable photoresponsive fluorescent switch system on the basis of [2 + 2] cycloaddition-cycloreversion involving diarylethylene and tetraarylcyclobutane and demonstrated its application in two-dimensional (2D) and three-dimensional (3D) optical data storage.[279] Several similar studies has shown designing data storage device utilizing reversible solid state photoreactivity.[80,85] In addition, several other literature reports show successful application of solid state photoreactivity in photoactivated molecular switches,[86] and nanoscale photomechanical actuators.[94]

Recent literature reports showed that a SCSC reaction becomes possible in nanocrystals even if the macro-dimensional crystals of same material do not display SCSC photoreactivity.[94,280,281] Therefore, miniaturization of crystals to nano dimension leads to development of functional nanomaterials and this property can be attributed to the large surface-to-volume ratio of the nanocrystals leading to efficient stress and strain relaxation.[94] Hence, the mechanical properties of the nanocrystals could be different compared to the macro counterpart as mechanical property is inherently related to stress and strain. Therefore, quantifying mechanical properties of nanomaterials is important to the context of both science and device application purposes. Moreover, measurement of mechanical property will help in determining the allowable operating limit of these materials in device applications.[282]

7.1.3 Mechanical properties of macro and nano organic cocrystals in a single crystal transformation

Our group has previously reported quantification of mechanical properties of nano-dimensional cocrystals involving 5-CN-resorcinol and trans-1,2-bis(4-pyridyl)ethylene (4,4'-bpe).[64] These cocrystals undergo hardening on SCSC transformation. AFM nanoindentation technique has been used to quantify the mechanical properties. It has been observed that nanometer sized cocrystals became 40% harder on photoreaction.

Similar type of cocrystals can easily be synthesized by just changing the template (5-CN-resorcinol in this case), while keeping the same reactant (4,4'-bpe) to undergo [2+2] solid state photo induced transformation.[81] Herein, we wanted to observe the effect of the template in mechanical properties of the nano-dimensional cocrystals. Therefore, we report mechanical changes involved in a series of cocrystals involving 4,4'-bpe and 4,6-di-halo-resorcinol (halo = Cl, Br, I). In this study, we investigated changes in mechanical properties of the unreacted cocrystals on changing the template. The effect of reactivity on mechanical properties has also been explored.

7.2 Experimental details

The nanococrystals were obtained by precipitation combined with sonochemistry. Solutions were filtered through a Millex syringe filter (PVDF, 0.2 μm, 13 mm) directly into cool hexanes (ca. 0 °C, 225 mL) while exposed to low-intensity ultrasonic radiation (ultrasonic cleaning bath Branson 2510R-DTM, frequency: 42 kHz, 6 % at 100 W). The resulting suspension was sonicated for 1–2 min, filtered, and dried at room temperature.

Nanometer-sized crystalline samples were suspended in hexanes at 0.25 mg mL^{-1} and then deposited on a freshly cleaved atomically flat mica substrate (*V–I* grade, SPI Supplies, Westchester, PA). All AFM studies were conducted using a molecular force probe 3D AFM (Asylum Research, Santa Barbara, CA). AFM height images and nanoindentation measurements were collected at room temperature using silicon probes (MikroMasch, San Jose, CA, CSC37) with a nominal spring constant of 0.35 N m^{-1} and a typical tip radius of curvature of 10 nm. Force–displacement curves were recorded in an organic solvent (*n*-tetradecane, Fluka). The force curves data were used to estimate the Young's modulus of a crystal by using a rearranged form of the Hertzian model.[64,283-286] The substrate-induced effects on the measured Young's modulus values were negligible here as the height of a nanocrystal (ranging from 50 to 400 nm) is more than one order of magnitude larger than typical indentation depth of 3.5 nm.

Diffraction data were measured on a Nonius Kappa CCD single-crystal X-ray diffractometer at room temperature (25 °C) using Mo$K_\alpha$radiation (λ=0.71073 Å). Structure solution and refinement were accomplished using SHELXS-97 and SHELXL-97, respectively.[287] All non-hydrogen atoms were refined anisotropically. Hydrogen atoms associated with carbon atoms were refined in geometrically constrained positions. Hydrogen atoms associated with oxygen atoms were calculated in an optimal hydrogen bonding geometry.

7.3 Result and discussion

7.3.1 Cocrystals under investigation

In this work we have studied mechanical properties of nano cocrystals of 2(4,6-di-halo-res)·2(4,4'-bpe) (where 2,4-di-halo-res refers to the 2,4-di-haloresorcinols, 4,4'-bpe=trans-1,2-bis(4-pyridyl)-ethylene). These nanomaterials undergo [2+2] solid state photodimerization in a SCSC manner resulting in a cyclobutane ring (Figure 7.1).[79,81] Our primary goal was to observe mechanical changes involved in both structural changes in substituted resorcinol template and the photoreaction. Hence, we used resorcinol template substituted with halogen groups as shown in Figure 7.1. Mechanical properties was quantified using AFM nano indentation technique and the unreacted samples showed a decrease in Young's modulus and photoreactivity with increasing size of the side chain halogen group (Cl, Br and I) in the template. Moreover, photoreaction induced a significant decrease of Young's modulus.

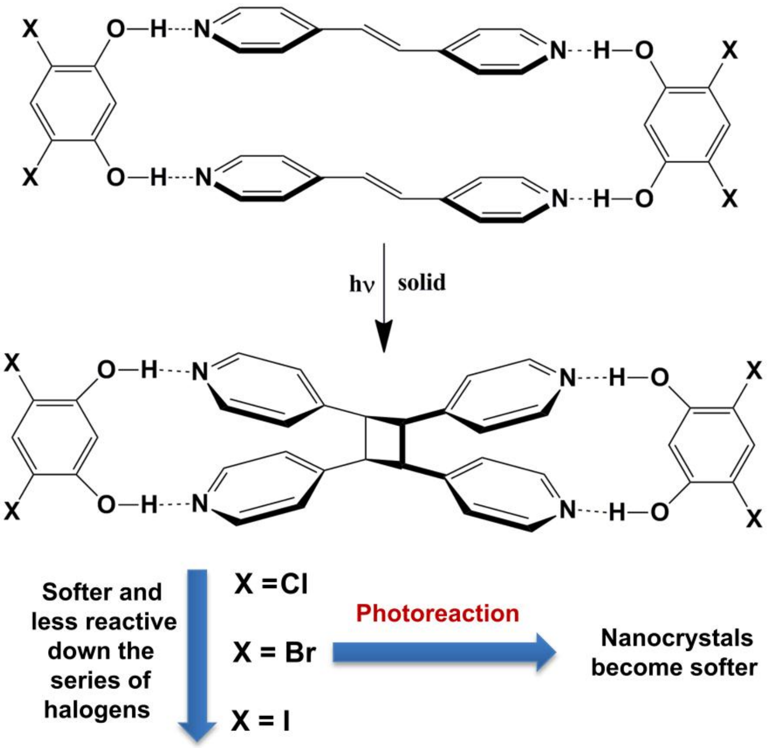

Figure 7.1 Photoreaction of cocrystals of 2(2,4-di-halo-res)·2(4,4’-bpe) is shown in the figure. The mechanical properties of cocrystals involving Cl, Br and I in the side chain of the template has been measured before and after the [2+2] photocycloaddition. The nano-cocrystals became softer and less reactive down the halogen series. Moreover, photoreaction resulted in softening of the cocrystals as well.

7.3.2 Morphology of the nano cocrystals

AFM and SEM micrograph of the cocrystals were obtained initially to monitor the change in their morphology due to photoreaction. Figure 7.2 shows representative AFM and SEM images of 2(4,6-di-Cl-res)·2(4,4’-bpe) crystals both before (Figure 7.2a,b) and after (Figure 7.2c,d) the photoreaction. AFM images of the single nanocrystals did not show any cracking or fragmentation upon photo-exposure; whereas any cracking or amorphous behavior was absent in the SEM image of an ensemble of crystals. Images obtained at different sample regions both before and after the photoreaction showed no cracking. Hence, this observation indicates that the photo induced cycloaddition reaction have occurred in a SCSC manner.[64] The general morphology of the unreacted cocrystals was similar for the other two samples with 4,6-di-Br-res and 4,6-di-I-res as template. Moreover, cocrystals with 4,6-di-Cl-res template have fully reacted on a UV exposure for approximately a week, whereas the reactivity decreased to 60% and 0% when 4,6-di-Br-res and 4,6-di-I-res were used as template. It is also worthwhile to mention that no noticeable change in the crystal morphology has been observed for these two samples upon UV exposure and hence they are not shown here. Crystal size of 0.3-1.5 μm was observed from AFM height images. The height of the crystals typically varied from 80 to 300 nm.

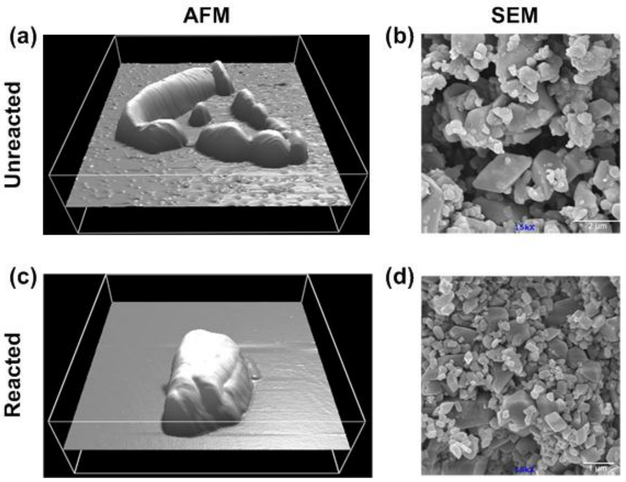

Figure 7.2 AFM and SEM images of unreacted (a, b) and photoreacted (c, d) cocrystals of 2(4,6-di-Cl-res)·2(4,4’-bpe) (where 2,4-di-halo-res refers to the 4,6-di-haloresorcinols, 4,4’-bpe=trans-1,2-bis(4-pyridyl)-ethylene).

7.3.3 Structural effect on SCSC reactivity

Single-crystal X-ray diffraction study of the millimeter sized cocrystals, performed prior to UV exposure showed the self-assembly of resorcinol templates and 4,4'-bpe through four O-H…N hydrogen bonds. Powder X-ray diffraction studies confirmed the structure of the solid. UV exposure resulted in complete conversion to the photoproduct using 4,6-di-Cl-res as the template, whereas the reaction goes to 60% completion using 4,6-di-Br-res as template. The 2(4,6-di-I-res).2(4,4'-bpe) cocrystal does not respond to UV exposure. The structural changes occurred during photodimerization reaction of 2(4,6-di-Cl-res)·2(4,4'-bpe) cocrystal are shown in Figure 7.3. Extent of photodimerization in all the three samples were controlled by the orientation of the 4,4'-bpe molecules (π overlap) and the distance between the two C=C bonds in the assembly. The distance between two reactive C=C bond in a single assembly was measured to be 3.82, 4.06 and 4.27 Å when using 4,6-di-Cl-res, 4,6-di-Br-res, 4,6-di-I-res as templates respectively. Whereas the geometry of the two 4,4'-bpe molecules were consistently face-to-face, the increasing C=C bond separation in a single assembly decreased the extent of photoreactivity. According to other reports, this C=C bond separation needs to be ≤ 4.2 Å for a solid state photoreaction to be occur.[288] Therefore, absence of photoreactivity in 2(4,6-di-I-res)·2(4,4'-bpe) cocrystals is consistent with the literature. Noticeably, AFM images showed retention of overall morphology, indicating SCSC photoreaction. X-ray analysis of 2(4,6-di-I-res)·2(4,4'-bpe) cocrystal confirmed SCSC photoreactivity and the X-ray parameters are reported in Table 7.1. The β angle changed from 99° to 95.8° to account for the tilt in the overall structure due to formation of 4,4'-tpcb while all the other parameters remaining quite similar after the photoreaction. This analysis has only been done for the 2(4,6-di-Cl-res)·2(4,4’-bpe) cocrystal as the photoreaction involving the other two samples does not go to the completion. In the next step, we wanted to investigate mechanical changes in all the three different unreacted cocrystals. In the last section, mechanical changes due to photoreaction have been investigated using AFM nanoindentation technique and structure property relationship is inferred.

Table 7.1 X-ray crystallographic data for unreacted and reacted cocrystals of 2(4,6-di-Cl-res)·2(4,4’-bpe).

Space group	**Unreacted**	**reacted**
a [Å]	8.5903 (10)	8.4640 (9)
b [Å]	11.8358 (13)	11.7179 (13)
c [Å]	16.7227 (18)	16.5438 (17)
α [°]	90	90
β [°]	99.037 (5)	95.85 (5)
γ [°]	90	90
V [Å^3]	1679.14 (3)	1632.27 (3)

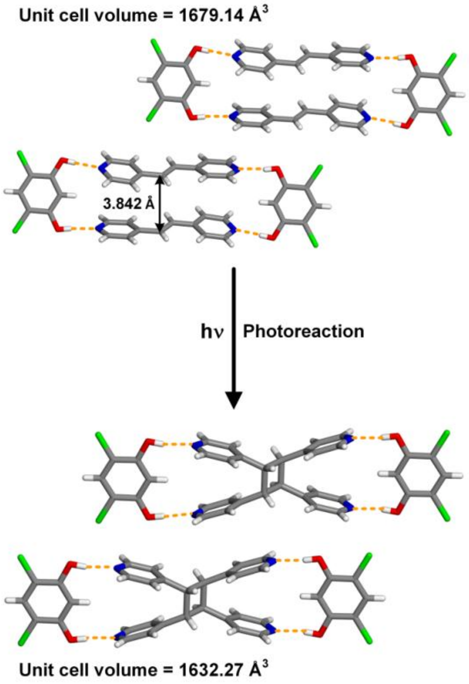

Figure 7.3 SCSC reactivity of 2(4,6-di-Cl-res)·2(4,4’-bpe) to form 2(4,6-di-Cl-res)·2(4,4’-tpcb).

7.3.4 AFM nanoindentation technique

Use of AFM nanoindentation technique to measure hardness of nanomaterials like thin film and polymers has been previously discussed in literature.[289,290] Hence, we will discuss briefly about the nanoindentation measurement in this report. In a typical indentation study an indenter of specific geometry is applied to the surface of inspection with a slowly increasing loading force.[291] The dependence of loading force on indentation is controlled by the shape of the indenter. For example, the loading force is proportional to the square of indentation, h^2 for a conical indenter; whereas the load is proportional to h and $h^{3/2}$ for cylindrical and spherical indenter respectively.[291] In our experiment we assume our indenter to be spherical. For a spherical indenter, the Young’s modulus is calculated from the force-displacement curve using a rearranged form of Hartzian model (eq. 7.1).[283-286]

$$F^{2/3} = C - \left[\frac{4}{3}\frac{ER^{1/2}}{(1-\sigma^2}\right]^{2/3} \Delta \ldots\ldots\ldots\ldots\ldots\ldots\ldots.7.1$$

where F is the loading force and R is the probe's radius of curvature. Δ and σ in the equation represent tip sample separation (indentation) and Poisson's ratio respectively. Hence, linear fit of $F^{2/3}$ *vs.* Δ plot, Young's modulus E can be quantified from the slope.

7.3.5 Young's modulus of unreacted cocrystals

Mechanical properties of unreacted cocrystals of 4,4'-bpe and 4,6-di-halo-res (halo = Cl, Br, I) were quantified using AFM nanoindentation technique. Initially, the nanocrystals were imaged and repeated force-displacement curves (20 force-displacement curves at every crystal spot) were collected in at least 10 different spots in each crystal to determine the local stiffness. This measurement has been repeated for at least 10 different crystals in each sample. Using the Hertzian model described in the previous section, Young's moduli have been quantified from all the force displacement curves recorded.

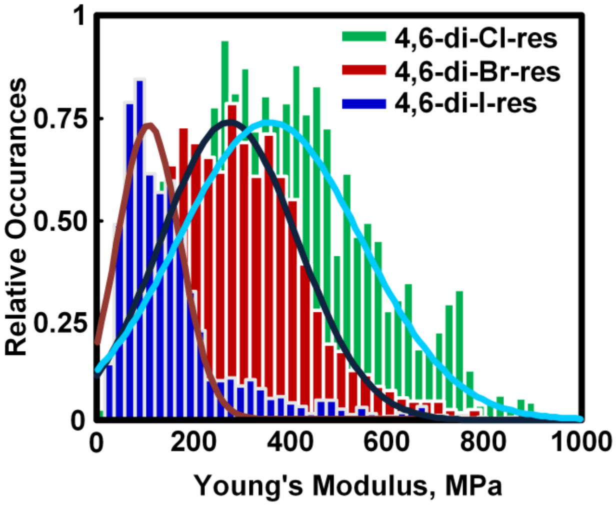

Figure 7.4 Histograms of the Young’s modulus values for 2(4,6-di-halo-res)·2(4,4’-bpe), where halo = Cl, Br, I.

All the Young’s modulus values collected for every sample was plotted in a histogram and shown in Figure 7.4. Gaussian fitting of the histogram yielded the average values of Young’s modulus for each sample.[64] The average Young’s modulus values were reported in Table 7.2. With the increasing size of the halogen in the template, average Young’s modulus was decreasing consistently. The decrease was recorded to be ~25% by changing the template from 4,6-di-Cl-res to 4,6-di-Br-res, whereas ~70% decrease was observed on using 4,6-di-I-res instead of 4,6-di-Cl-res as template. This observation shows a direct evidence of the effect of structural changes on the mechanical properties. Ultimately, this discovery is important to design functional materials with desired mechanical properties.

7.3.6 Mechanical changes on photoreaction

In previous section we observed dependence of mechanical properties on the structural changes in the unreacted cocrystals. Herein, the solid state photoreactivity has allowed us to examine the correlation of mechanical properties with the extent of reactivity. Hence, the unreacted nanocrystals were subjected to UV radiation and the progress of the reaction was constantly monitored using NMR spectroscopy. While 4,6-di-Cl-res based cocrystals has been completely converted to the photoproduct, 4,6-di-Br-res counterpart has stopped at ~60% conversion. In the next step, mechanical properties were measured for these photoproducts. It is worthwhile to mention that the photoproduct of 2(4,6-di-Br-res)·2(4,4’-bpe) cocrystals were not separated from remaining unreacted material in the sample. Hence, the mechanical properties represents the mixture of ~60% reacted and ~40% unreacted sample in this case.

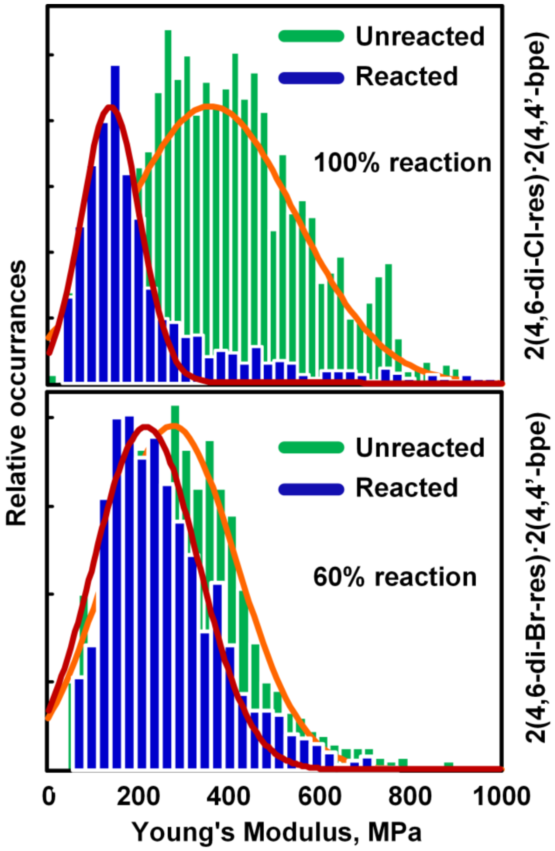

Figure 7.5 Histogram of Young's modulus of 2(4,6-di-Cl-res)·2(4,4'-bpe) and 2(4,6-di-Br-res)·2(4,4'-bpe) before and after the photoreaction.

Table 7.2 The Young's modulus values for different cocrystals reported with standard deviation.

	Unreacted		**Reacted**		
Cocrystal	**YM, MPa**	**# crystals**	**% reacted**	**YM, MPa**	**# crystals**
2(4,6-di-Cl-res)·2(4,4'-bpe)	360 ± 80	16	100	140 ± 30	25
2(4,6-di-Br-res)·2(4,4'-bpe)	275 ± 70	10	60	220 ± 70	18
2(4,6-di-I-res)·2(4,4'-bpe)	105 ± 35	24	0	125 ± 45(100 h of exposure)	13

The values of Young’s modulus determined for all the reacted and unreacted cocrystals were comparable with our previous work with similar type of cocrystals[64] and other reported values for protein crystals and macromolecules.[283,292] The cocrystals were observed to become softer on photoreaction. Extent of softening due to photoreaction and solid state photoreactivity decreased gradually with the increase in the size of the halogen in template side chain. Hence, finding the correlation of mechanical properties with the reactivity opens a new door to study structure-mechanical properties relationship of nanocrystals of different kinds. Ultimately, we want to reach a point where we can predict reactivity with the knowledge of the mechanical properties of a nanocrystalline material. Another important observation that cocrystals provide ample flexibility in terms of mechanical properties and reactivity of the materials can be utilized to design novel functional nanomaterials with controlled stiffness.

7.4 Conclusions

In conclusions, AFM nanoindentation has been used to study template dependent changes in mechanical properties of nanocrystals that undergo a SCSC photodimerization. Substitution of halogen functional group in the template affected the effective distance between two reactive C=C groups in the assembly. This substitution has significantly affected the extent of solid state reactivity and mechanical properties of the unreacted cocrystals. Herein, it should be realized that this type of substitution in the template will easily provide a better control in mechanical properties of functional nanomaterials, potentially usable for device application. Photoreaction caused softening of the nanocrystals in contrast to hardening observed in our previous work with nanometer sized cocrystals of 2(5-CN-res).2(4,4’-bpe).[64] Therefore, we state that the trend in mechanical properties as a function of photoreactivity is highly material specific and several other reactive nanocrystals need to be studied to structurally justify hardening and softening behavior due to photoreaction. Moreover, changes in the halogen group inherited noticeable difference in the changes in mechanical properties due to photoreaction (60% decrease for 4,6-di-Cl-res as template compared to only 20% for 4,6-di-Br-res) of the photoproduct. We expect these observation and future work on quantifying mechanical properties of several other nanocrystalline materials will ultimately enable us to completely understand the correlation of mechanical properties, solid state reactivity and structural changes in nanocrystals.

CHAPTER 8

PHOTOPATTERNING OF A TWO-COMPONENT SMALL-MOLECULE THIN FILM DERIVED FROM REACTIVE HYDROGEN-BONDED CO-CRYSTALS

8.1 Introduction

Thin films of organic molecules are of great interest as materials for organic light-emitting diodes (OLEDs), transistors (OTFTs), memory devices, and sensors.[293-298] Whereas methods to control the compositions and bulk properties of organic thin films typically rely on conventional covalent synthesis to form and modify molecules that comprise a film,[299,300] supramolecular approaches wherein the fabrication and properties of a film are governed by assembly processes involving two or more molecular components have received less attention.[301,302] A recent supramolecular assembly approach to thin films has involved combining block copolymers with small molecules *via* hydrogen bonds, which has controlled surface porosity and patterning.[303] A related study on combining, or blending, two block copolymers *via* hydrogen bonds has also been employed to form nanoporous films with addressable arrays.[304] A supramolecular approach to thin films is attractive not only owing to an ease with which organic functionality can be incorporated and tuned into a film *via* component substitution, but also offers access to properties of a film that may, otherwise, not be accessible from an individual component.

8.2 Design and photoreactivity of the thin film and its potential application

Here, we report a supramolecular approach to form and achieve control of optical patterning of an organic thin film based exclusively on small molecules. The design of the thin film is based on directing [2+2] photodimerizations in two-component organic solids, or co-crystals.[305] The use of co-crystals to assemble olefins in solids to undergo photodimerization,[81,306] as well as control other bulk physical properties (e.g. porosity, optical),[307] is gaining much attention. In particular, we have demonstrated that co-crystallization of resorcinol (res), and derivatives (e.g. phloroglucinol or phgl), with pyridyl-functionalized olefins (e.g. 4,4'-bpe) affords zero dimensional (0D), or discrete, hydrogen-bonded supramolecular assemblies wherein stacked carbon-carbon double (C=C) bonds are preorganized for photoreaction (Figure 8.1).[81,305,308,309] During experiments to study chemicophysical properties of our co-crystals, we have discovered that, despite relatively small changes to molecular structure,[81] there exist significant differences in solubilities of the solids before and after photoreaction. Given that differential solubilities in chemical reactions are exploited to pattern thin films, we turned to determine whether the co-crystals can be used as starting points to develop reactive thin-film materials.[310,311] Reactive two-component films of poly(4-vinylpyridine) and polydiacetylenes have afforded films that generate microstructures by photolithography.[303] Hydrogen bonds stabilized the diacetylenes within the condensed environment. Moreover, to our knowledge, the only example of a thin film involving a co-crystal is the ferroelectric (phenazine)·(chloranilic acid).[312] We demonstrate that long-chain alkylation of a hydrogen-bond-donor component in the form of hex-phgl influences component deposition to generate a highly-uniform film that supports optical patterning of well-defined microstructures (Figure 8.1).[313] In particular, a decrease in solubility following the cycloaddition is exploited wherein a masked area of the unreacted film is removed post reaction via dissolution and, thereby, serves as a negative photoresist.

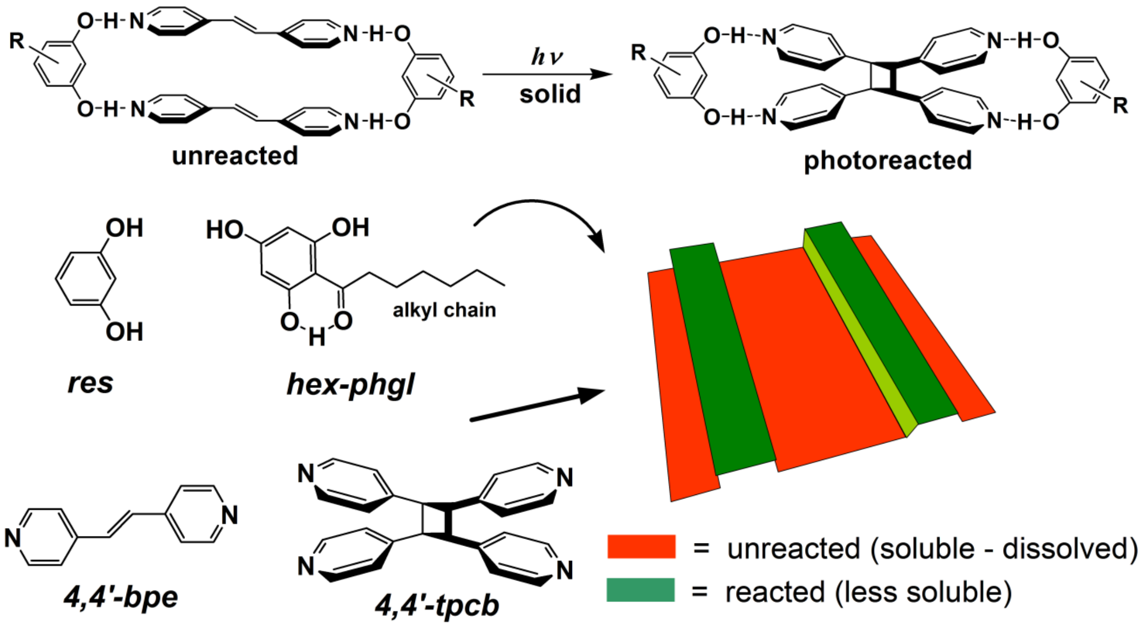

Figure 8.1 Co-crystals for reactive thin films involving res, hex-phgl, and 4,4'-bpe. Modified hex-phgl achieves thin film. Spatial exposure to UV light enables lithography (orange = unreacted; green = reacted)

In our initial studies, we attempted to generate a thin film of the parent co-crystal 2(res)·2(4,4'-bpe). Solubility experiments in acetonitrile and related polar organic solvents revealed the solid prior to photoreaction to be moderately soluble (1.92 mg/mL). The cycloaddition, however, afforded a material that was markedly less soluble (0.08 mg/mL). Moreover, the co-crystal effectively underwent a 24-fold decrease in solubility upon photoreaction. Whereas changes in solubility based on [2+2] photodimerizations have been reported for polymers,[304,314] we are unaware of an example involving small molecules in the crystalline state.

8.3 Method optimization

To prepare a thin film of 2(res)·2(4,4’-bpe), we performed slow solvent evaporation and spin coating experiments on glass as a substrate. Both methods, however, afforded particles of sizes and morphologies that did not support a film. Solvent evaporation generated various interesting structures but none of them resulted in thin film with reasonable roughness (Figure 8.2). AFM images from spin coating (1 min, 1000 rpm) revealed particles *ca* 2 to 5 μm in diameter that were spatially separated on the order of 10 μm (Figure 8.3a). Several attempts to form thin films by varying solvent and spin coating rate invariably afforded larger particles. Hence, this observation indicates necessity of optimizing chemical components along with the procedure optimization, such as spin coating conditions.

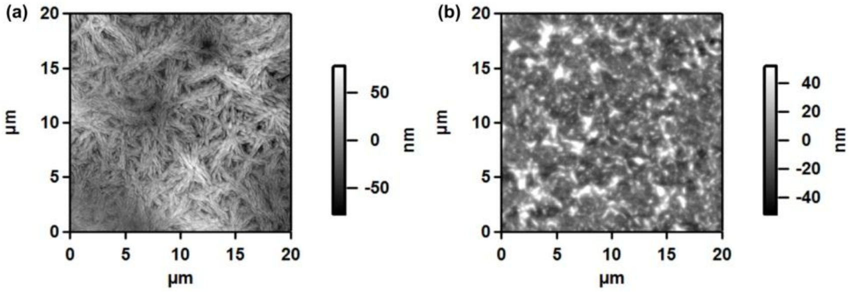

Figure 8.2 Morphology of thin film trials with (a) res and 4,4’-bpe dissolved in iPrOH at 12 mg/ml with spin coating speed of 1000 rpm for 1 minute and (b) res and 4,4’-bpe dissolved in 1:1 mixture of di-Cl benzene and iPrOH and the morphology is obtained by slow evaporation.

For the components of 2(res)·2(4,4’-bpe) to be more amendable to form a uniform thin film, we turned to selectively vary one of the small-molecule components. In particular, we expected that attachment of a long alkyl chain to the backbone of a res could improve molecular ordering by promoting inter-chain van der Waals forces.[314] An alkyl chain substitution along the hydrogen-bond-donor would not only support the formation of a thin film but also enable the molecular structure of 4,4’-bpe to remain intact and, thus, the intended reactivity to be retained in the condensed environment.[313,315]

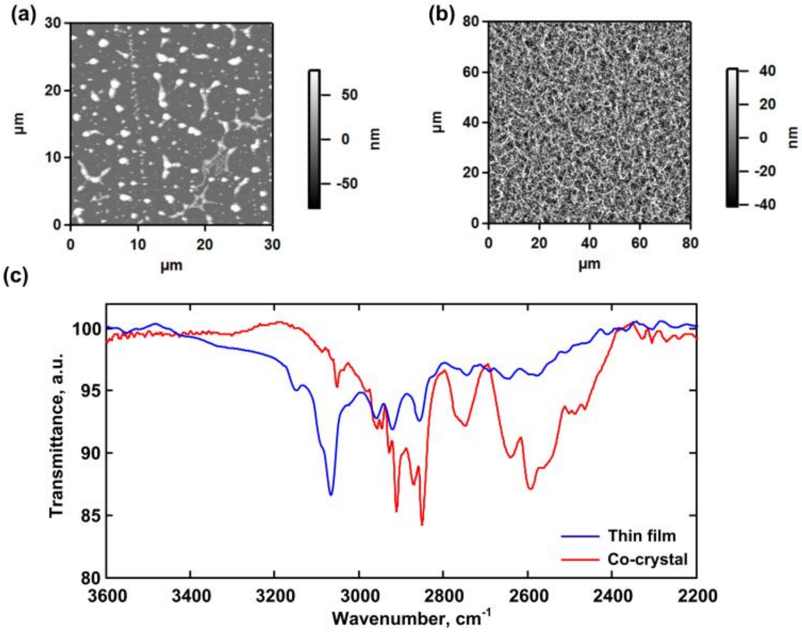

Figure 8.3(a) AFM height image of res and 4,4’-bpe from spin coating showing micro-particles, (b) uniform film involving hex-phgl, (c) ATR-IR spectra of thin film and co-crystal of 2(hex-phgl)·2(4,4’-bpe).

Following several trials with various hydrogen-bond-donors, chain-substituted hex-phgl and 4,4’-bpe were determined to yield a uniform film. The phgl organizes 4,4’-bpe in the bulk solid 2(hex-phgl)·2(4,4’-bpe) for a photodimerization to give 4,4’-tpcb.[309]

To form a film, a solution of hex-phgl and 4,4'-bpe (total concentration of 9 mg/ml, 1:1 molar ratio) in isopropanol and 1,3-dichlorobenzene (50:50 *v/v*) was spin coated onto glass. In contrast to res and 4,4'-bpe, the spin coating produced a thin film of a highly-uniform morphology. AFM images revealed a film of *ca* 20 nm roughness within an 80 μm x 80 μm sample region (Figure 8.3b). Uniform films with thicknesses between 70 and 80 nm could be routinely prepared. An IR spectrum of the film deposited on an ATR crystal supported the components to assemble *via* hydrogen bonds (Figure 8.3c). In particular, a broad peak with several subsidiary minima in reflectance intensity was present in the range of 2200-3200 cm^{-1} of both the thin film and bulk co-crystals which is consistent with (phenol)O-H···N(pyridine) forces.[316] Similar peaks were not present in samples of pure individual components.

8.4 Characterization of solid state reactivity of the thin film

Reactivity properties of the thin film were next studied. Two films of similar thickness were spin coated onto glass. One film was exposed to ultraviolet (UV) light for a period of *ca* 20 h. Importantly, a sharp contrast in dissolution was determined when each film was suspended in a mixture of pentane and ether (2:1 *v/v*). Whereas the film not exposed to the UV light dissolved within seconds, greater than half of the exposed film remained after 90 s of washing (Figure 8.4). A significant decrease in solubility of the film was, thus, realized following exposure to the UV light.

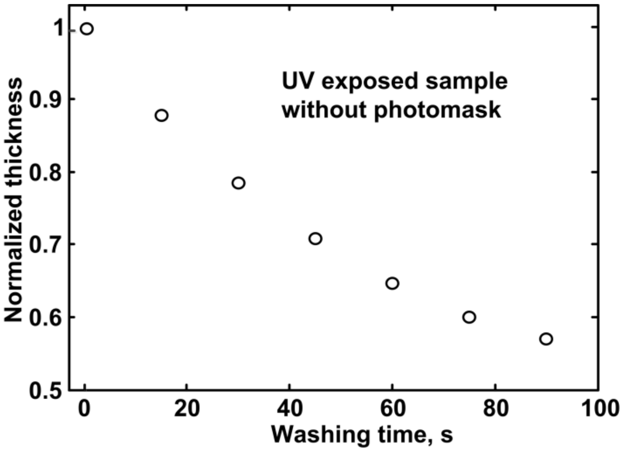

Figure 8.4 Graph showing changes in thickness of the photoreacted thin film normalized to the initial thickness plotted as a function of washing time in a mixture of pentane and ether (2:1 *v*/*v*).

We attribute the decrease in solubility to a photodimerization of 4,4'-bpe that generates 4,4'-tpcb. The extent of photoreaction has been characterized using three different spectroscopic techniques, such as, ^{1}H NMR, Mass spectroscopy and STXM. Initially, mass spectrometry performed on samples of 4 unreacted thin films (Figure 8.5) and 4 reacted films (Figure 8.6). The samples were dissolved in methanol to form a stock solution. From the stock solution 30 μL was diluted with 1:1 water: acetonitrile with an additional 0.1 % formic acid solution. The peak at 183 au in the mass spectrum of the unreacted thin film is consistent with a monoprotonated 4,4'-bpe molecule. The peak at 239 au is consistent with the monoprotonated hex-phgl. After irradiation, a new peak at 365 au appears in the spectrum, consistent with a monoprotonated 4,4' tpcb. The appearance of the peak demonstrates a photodimerization occurs in the thin film upon exposure to UV light. The base peak after reaction at 183 au is likely due to unreacted 4,4'-bpe and/or diprotonated tpcb, which have equal mass to charge ratios.

Figure 8.5 ESI mass spectrum of films containing 4,4′-bpe and hex-phgl before UV exposure.

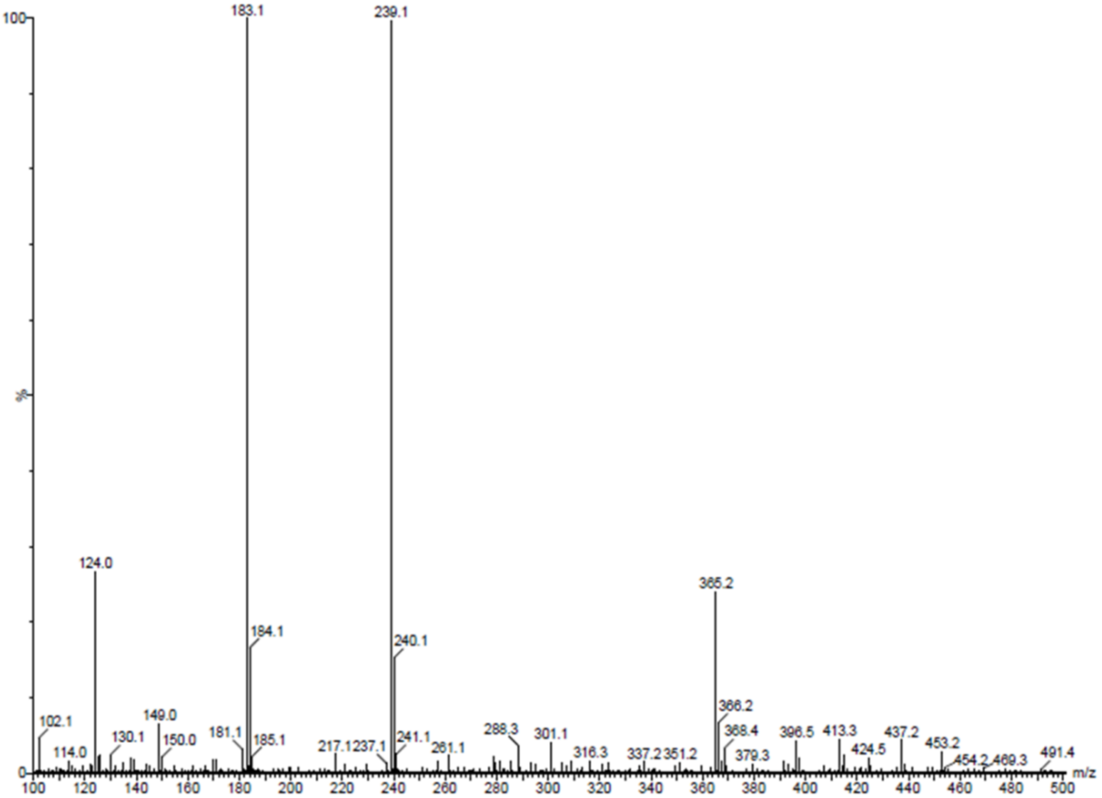

Figure 8.6 ESI mass spectrum of films of 4,4′-bpe and hex-phgl after 20 hours of UV exposure.

To collect a ^{1}H NMR spectrum, 80 thin films were exposed to UV irradiation for 20 hours (Figure 8.7). The reacted thin films were concentrated into a single sample by dissolving each thin film in ethanol and combing the samples. From our previously reported result we know the peak at 4.7 ppm is from the cyclobutane moiety of the photoproduct. The peaks at 8.6 and 8.3 ppm are from the α-hydrogens on the pyridines. The ratio of these peaks suggests approximately a 50% photoreaction in the thin films.

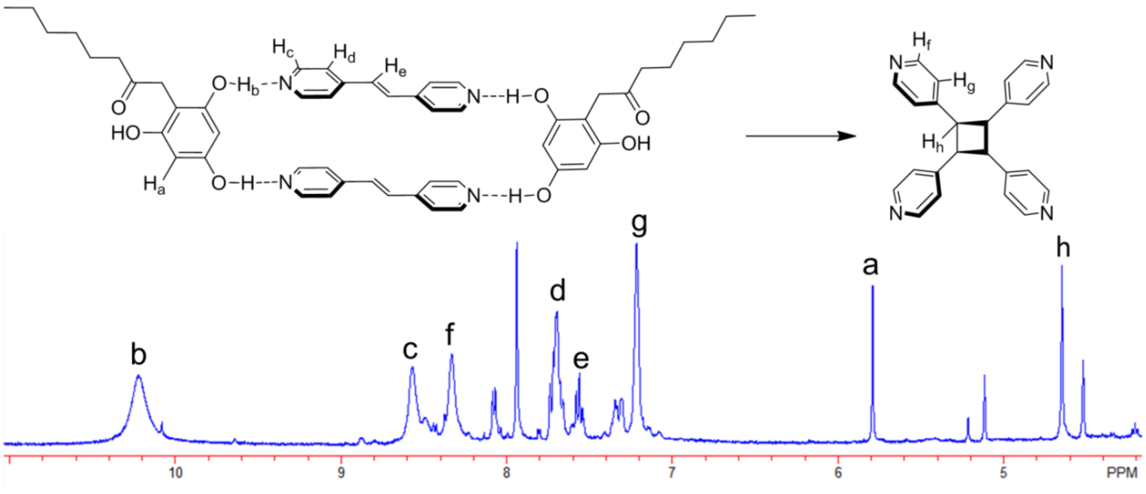

Figure 8.7 ^{1}H-NMR spectrum of (4,4'-bpe)·(hex-phgl) after UV irradiation

A direct characterization of the reactivity of the film using scanning transmission X-ray microscopy (STXM)[31,58,135,173,199] and near edge X-ray absorption fine structure (NEXAFS) spectroscopy[317] was consistent with a photodimerization of 4,4'-bpe (Figure 8.9).[144] For these experiments, thin films were prepared on a Si_3N_4 membrane (Silson Ltd., England) and exposed to UV radiation. STXM images of the unreacted and reacted films revealed morphologies nearly similar to those imaged using AFM (Figure 8.8). Two signatures for unreacted C=C bonds were present in the C K-edge NEXAFS spectra at 284.6 eV and 285.8 eV, with the former being assigned to 1s$\rightarrow\pi^*$ transitions for the olefinic C=C bond.[318,319] A comparison of the C K-edge spectra of the reacted and unreacted films revealed a relative decrease in the C=C bond of 4,4'-bpe (284.6 eV) upon exposure to the UV light, which is consistent with cyclobutane formation (Figure 8.8a).[81] Moreover, the absorbance for two C=C transitions (aromatic and non-aromatic) needs to be separated in order to quantify the extent of photodimerization reaction accurately. A Gaussian fit has been applied to the two transitions for aromatic and non-aromatic C=C with the peak maxima and normalized absorption reported in Table 8.1, and the width of the peaks has been obtained for the unreacted thin film. Same peak width and peak maxima for both the transitions are used to fit the spectra of reacted thin film and the normalized absorbance for both the transitions is obtained. Provided that the width of both the peaks are held constant for unreacted and reacted thin film, the extant of photoreaction can be obtained directly from the change in normalized absorbance of the non-aromatic C=C at ~284.6 eV. The value for extent of reaction was observed to be ~ 50% using this method and was consistent with the NMR data.[58]

Table 8.1 Gaussian fit parameters for thin film NEXAFS spectra (Figure 8.8b)

Gaussian Peaks	Parameters	Unreacted thin film	Reacted thin film
Peak 1: Non aromatic C=C	Normalized absorption	0.6718	0.3262
	Peak maxima, eV	284.52	284.52
	Width, eV	0.5226	0.5226
Peak 2: Aromatic C=C	Normalized absorption	1.23	1.4854
	Peak maxima, eV	285.8	285.8
	Width, eV	0.5662	0.5662

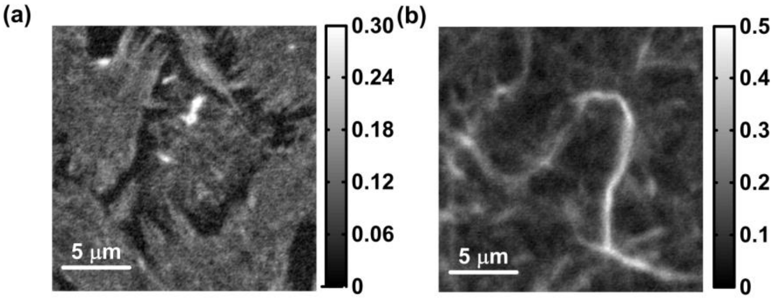

Figure 8.8 STXM images of 2(hex-phgl)·2(4,4'-bpe) prepared on a Si_3N_4 membrane (a) before and (b) after the UV exposure. The NEXAFS spectra were collected on the same region of this thin film.

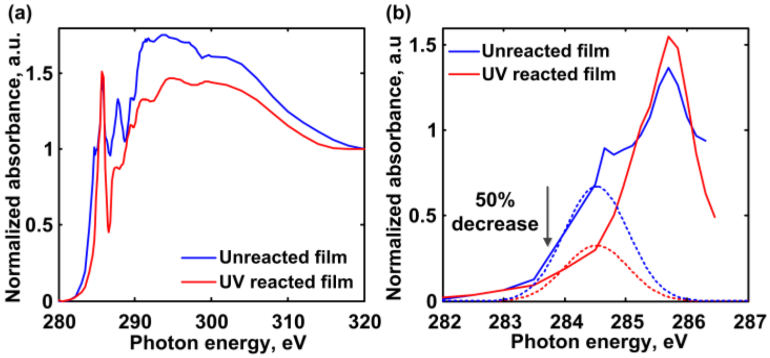

Figure 8.9(a) C K-edge NEXAFS spectra of the thin film prepared on Si_3N_4 window using the same conditions. (b) Narrower energy range of the C K-edge spectra showing two different transitions for aromatic and nonaromatic C=C at 285.8 and 284.6 eV. The coupled Gaussians fit (dotted line) of the spectra performed to calculate extent of reaction, ca 50%, which is consistent with the result obtained using NMR.

8.5 Photolithography on the thin film

The reactive film was next used for photolithography. In the experiment, a surplus chrome waveguide photomask was used to project a grating pattern of alternating 4 μm bars onto the film surface. The mask was placed directly onto the film, with the UV light source being positioned above the surface. Following exposure to UV radiation (15 min), the film was developed with a mixture of pentane and ether (2:1 *v/v*). The film has been washed stepwise and AFM height image is obtain in every 15 seconds of washing. From AFM height imaging, each wash resulted in gradual removal of unreacted solid, which is consistent with the small-molecule components functioning as a negative photoresist (Figure 8.10).[320,321] The darker and brighter regions correspond to unreacted and reacted material, respectively. Complete removal of unexposed solid was achieved in as little as 60 s.

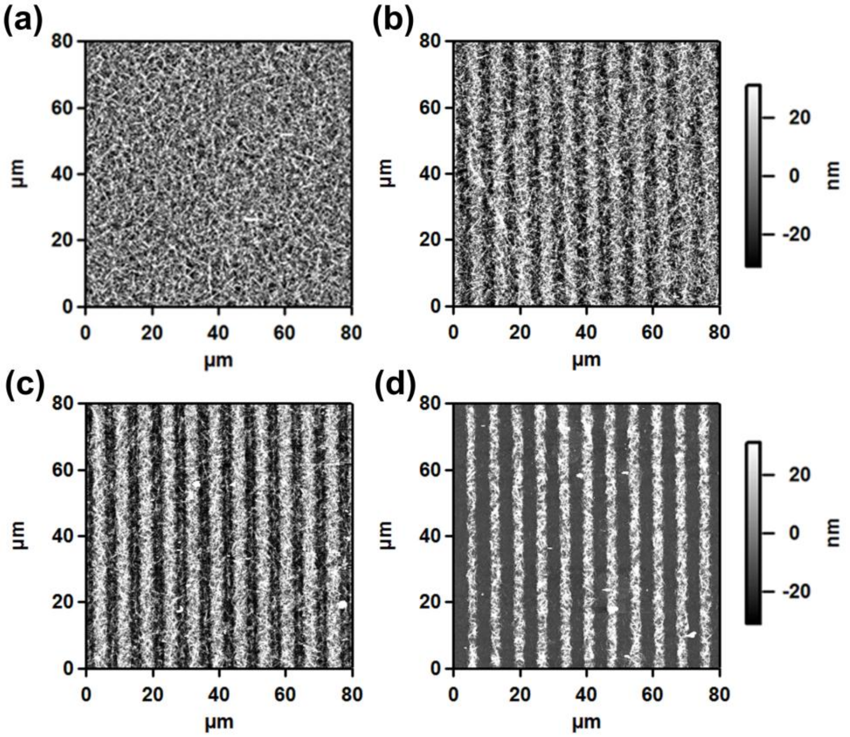

Figure 8.10 AFM images of micron stripes from photoresist of the two-component thin film based on hex-phgl and 4,4’-bpe (area: 80 µm x 80 µm). Washing times: (a) 0 s, (b) 30 s, (c) 45 s, and (d) 60 s.

Thicknesses of the films were next quantified from cross-sectional analyses of the patterns using the AFM scratch method.[322] Prior to photoreaction, the films exhibited thicknesses on the order of 70 nm. Increasing washing times resulted in decreasing thicknesses while height variation between the exposed and unexposed regions increased (Figure 8.11). Following 60 s of washing, the width of the vertical stripes was 4.5 µm while the unexposed material was completely removed reaching the glass substrate (Figure 8.11a). Height differentials between crests and troughs stripes varied from 30-35 nm could be readily imaged (Figure 8.11b). The sharp features of the film confirm applicability of the co-crystal as an efficient photoresist. Given the modularity of the approach, varied combinations of small molecules are expected attractive for thin-film formation.

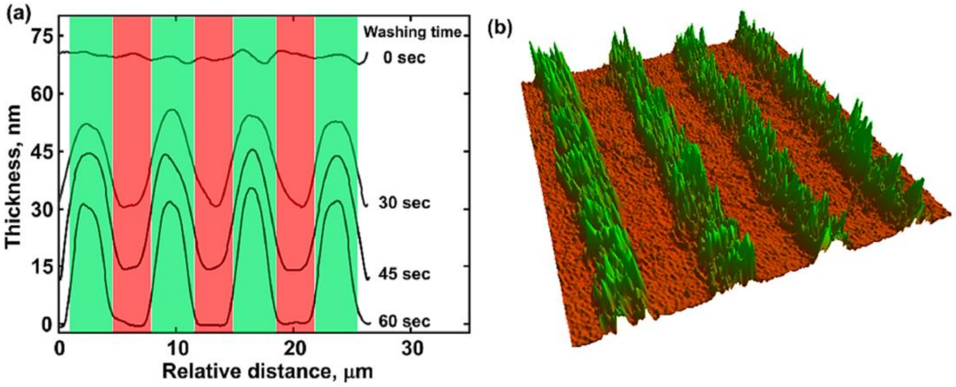

Figure 8.11 Cross-sectional height profiles of thin film 2(hex-phgl)·2(4,4'-bpe) exposed to UV light at different washings: (a) direct measurements and (b) AFM image. Orange = exposed and dissolved area; Green = reacted area.

8.6 Conclusion

In conclusion, we have reported a reactive organic thin film based on a co-crystal that involves two small-molecule components. The film has been developed for photolithography wherein the product of an intermolecular [2+2] photodimerization exhibits a significant decrease in solubility. We envisage that different combinations of small-molecule components may be developed to prepare reactive films with tunable physical and chemical properties.

CHAPTER 9

SUMMARY AND FUTURE WORK

9.1 Summary

The effect of atmospheric particles on earth climate is controlled by their hygroscopic properties, density, elemental composition etc. Therefore, we have designed several new methodologies to quantify these properties on a single particle basis. Hygroscopic properties of atmospherically relevant inorganic particles, such as, NaCl, NaBr and NaI have been quantified using STXM. A unique model combining Beer's law and the formula of the ellipsoid (Particle shape assumed to be an ellipsoid) has been developed to calculate mass of water in a single particle basis. We anticipate the approach will be especially useful for quantitative studies of the spatially resolved hygroscopic properties of aerosols with complex chemical mixture. Moreover, atmospheric aerosols are often found to be a complex mixture of organic and inorganic chemical species. Therefore, we have studied the effect of organic acids on the hygroscopic properties of NaCl. Interestingly, the hygroscopic properties of the two component mixture samples are not a simple linear combination of the hygroscopic properties of the single chemical components. Hence, we have shown that the environmental effects of particles consisting of NaCl and organic acids will be significantly different from that of the pure NaCl particles.

The density and chemical composition of these submicrometer particles are another two parameters which need to be quantified to completely understand and predict the atmospheric effects of the aerosol particles. A unique combination of AFM and STXM resulted in a model capable of quantifying the density and elemental composition of unknown samples. Moreover, the lower density of all the samples compared to the bulk density suggests porosity of the particles. This method can potentially improve the prediction of density and composition dependent atmospheric effects significantly.

Moreover, atmospheric fate of any aerosols particles depends on the RH. Depending on the RH, the particles can go through various chemical transformations, resulting in altercation of the atmospheric effects. Herein, we studied a keto-enol tautomerism reaction occurring in deliquesced malonic acid particle, which is completely absent in the bulk solutions. Using absorbance of different peaks in NEXAFS spectra, we have developed a method to calculate the equilibrium constant of the tautomerism reaction. The equilibrium constant was observed to be RH dependent. This observation in deliquesced malonic acid particles suggests the existence of unique characteristic of materials in submicrometer particles, which is otherwise not observed in the bulk. Moreover, this particular observation will be significantly useful to study the total concentration of Secondary Organic Aerosols (SOA) and their corresponding atmospheric effects.

In the latter half of the work, mechanical properties and device application potential of organic nano-cocrystals are studied. Organic nanocrystals capable of undergoing solid state photochemical changes in a single-crystal-to-single-crystal (SCSC) manner have been particularly important in fabricating molecular switches, data storage devices etc. Mechanical properties of these nanomaterials may control its SCSC reactivity. In addition, investigation of mechanical stiffness is important to define allowable limit of stiffness towards device application. Therefore, we studied mechanical properties of series organic nano cocrystals primarily consisting of trans-1,2-bis(4-

pyridyl)ethylene and substituted resorcinol using AFM nanoindentation technique. Dependence of mechanical properties and SCSC reactivity on the size of halogen in the resorcinol structure is observed in this work. Moreover, photolithography on the thin film of these organic cocrystals has been performed to demonstrate its applicability as a photoresist.

9.2 Future directions

We have demonstrated novel use of chemical and mechanical microscopic techniques to quantify several physicochemical properties of nanomaterials. Different future directions involving understanding of physical properties of different nanomaterials are proposed in the following section.

9.2.1 Composition dependent hygroscopic properties of environmental particles

All of our work on quantification of hygroscopic properties involved laboratory generated particles. The atmospheric particles generated from various source such as biomass burn, phreatomagmatic eruptions etc. consist of complex mixture of organic and inorganic materials and often show compositional difference on a particle to particle basis. In this context, the quantification of elemental composition on a single particle basis utilizing NEXAFS spectra will be important to predict the environmental effects of each of the particle. Subsequent quantification of hygroscopic properties on a single particle basis will then allow us to observe the effect of each of the chemical component on the hygroscopic properties. Moreover, NEXAFS and micro-FTIR spectroscopy will also be utilized to examine possible chemical changes as a function of RH.

Mixing state of these particles is another interesting property to observe. The mixing of chemical component could be different on a particle to particle basis. Therefore, single particle studies are required to explore the mixing state. Hence, principle component analysis in STXM will be used for chemical mapping of these samples. Then, using the NEXAFS spectra of different sample region, the spatially resolved elemental composition will be quantified. Moreover, evolution of different sample region as function of RH will be observed to correlate the composition dependence of hygroscopic properties.

Ultimately, we anticipate the proposed studies will significantly improve the large uncertainty in overall negative radiative forcing by atmospheric aerosols. All the studies reported in this work involve laboratory generated particles. Therefore, we want to implement our novel methods in quantifying physicochemical properties of fine particles towards the field samples in the next step.

9.2.2 Structure-property relationship of nanometer dimensional cocrystals

Mechanical properties of nanomaterials may control their solid state SCSC reactivity. It is obvious that reactivity of the cocrystals depend on the structure of the material under investigation. We believe mechanical properties of these materials can also be a controlling factor in SCSC reactivity. Therefore, we are performing measurement of mechanical properties on several nanometer dimensional cocrystals in order to understand structure and mechanical property relationship. In all the Young’s modulus measurement performed in our research involved 4,4’-bpe as the reactive center in the cocrystals. In future, we will study similar mechanical changes in photoreactive materials involving several other reactive molecules listed in Scheme 9.1. These materials can form cocrystals with resorcinol template. The reactivity and mechanical changes on photoreaction will be measured for these cocrystals. Moreover, some of these molecules (e.g., 1,4-bpeb, 1,4-bpbd, and 1,6-bpht) have multiple reactive centers. Therefore, it would be interesting to study mechanical changes due to photoreaction in each reactive center. In addition, template dependent mechanical properties of these materials will also be explored. These studies will ultimately improve our understanding on molecular structure and mechanical properties relationship.

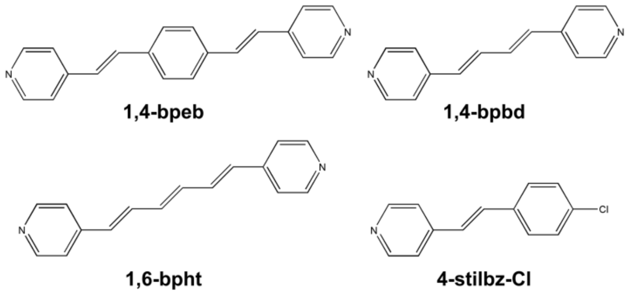

Figure 9.1 Materials capable of undergoing solid state photoreaction in a cocrystals with resorcinol template.

6.2.3 Conductive thin film and its device application

We have already demonstrated that cocrystal assembly of substituted resorcinol and 4,4’-bpe can be used to fabricate a thin film. Photolithography on the thin film showed its potential application as a photoresists. In our previous work, we have observed electrical conductivity in several other nanometer dimensional cocrystals. Hence, we will attempt to form thin film of these materials in future. Photolithography on these thin films can potentially form conductive nanowires. Moreover, we hope to demonstrate the use of these thin films in field effect transistors (FETs).

BIBLIOGRAPHY

(1) Ollila, A. V. E. *Energ Environ-Uk* **2012**, *23*, 781.

(2) Karakurt, I.; Aydin, G.; Aydiner, K. *Renew Energ* **2012**, *39*, 40.

(3) Merrild, H.; Christensen, T. H. *Waste Manage Res* **2009**, *27*, 781.

(4) Jeffrey, S. G.; Nancy, A. M.; John, E. F. In *Understanding Greenhouse Gas Emissions from Agricultural Management*; American Chemical Society: 2011; Vol. 1072, p 275.

(5) Held, I. M.; Soden, B. J. *Annu Rev Energ Env* **2000**, *25*, 441.

(6) Sulbaek Andersen, M. P.; Waterland, R. L.; Sander, S. P.; Nielsen, O. J.; Wallington, T. J. *Journal of Photochemistry and Photobiology A: Chemistry* **2012**, *233*, 50.

(7) Le Treut, H.; Somerville, R. *Climate Change 2007: The Physical Science Basis* **2007**.

(8) Péré, J. C.; Colette, A.; Dubuisson, P.; Bessagnet, B.; Mallet, M.; Pont, V. *Atmos Environ* **2012**, *62*, 451.

(9) Choobari, O. A.; Zawar-Reza, P.; Sturman, A. *J Geophys Res-Atmos* **2012**, *117*.

(10) Alizadeh Choobari, O.; Zawar-Reza, P.; Sturman, A. *Atmos Environ* **2012**, *61*, 294.

(11) Zhao, C.; Liu, X.; Leung, L. R. *Atmos Chem Phys* **2012**, *12*, 3717.

(12) You, Y.; Renbaum-Wolff, L.; Carreras-Sospedra, M.; Hanna, S. J.; Hiranuma, N.; Kamal, S.; Smith, M. L.; Zhang, X. L.; Weber, R. J.; Shilling, J. E.; Dabdub, D.; Martin, S. T.; Bertram, A. K. *P Natl Acad Sci USA* **2012**, *109*, 13188.

(13) Flores, J. M.; Bar-Or, R. Z.; Bluvshtein, N.; Abo-Riziq, A.; Kostinski, A.; Borrmann, S.; Koren, I.; Koren, I.; Rudich, Y. *Atmos Chem Phys* **2012**, *12*, 5511.

(14) Zhang, Q.; Meng, J.; Quan, J.; Gao, Y.; Zhao, D.; Chen, P.; He, H. *Atmos Chem Phys* **2012**, *12*, 3783.

(15) Yang, F.; Xue, H.; Deng, Z.; Zhao, C.; Zhang, Q. *Atmos Chem Phys* **2012**, *12*, 5399.

(16) Ringuet, J.; Albinet, A.; Leoz-Garziandia, E.; Budzinski, H.; Villenave, E. *Atmos Environ* **2012**, *61*, 15.

(17) Cheng, M. T.; Tsai, Y. I. *Sci Total Environ* **2000**, *263*, 101.

(18) Fiore, A. M.; Naik, V.; Spracklen, D. V.; Steiner, A.; Unger, N.; Prather, M.; Bergmann, D.; Cameron-Smith, P. J.; Cionni, I.; Collins, W. J.; Dalsoren, S.; Eyring, V.; Folberth, G. A.; Ginoux, P.; Horowitz, L. W.; Josse, B.; Lamarque, J. F.; MacKenzie, I. A.; Nagashima, T.; O'Connor, F. M.; Righi, M.; Rumbold, S. T.; Shindell, D. T.; Skeie, R. B.; Sudo, K.; Szopa, S.; Takemura, T.; Zeng, G. *Chem Soc Rev* **2012**, *41*, 6663.

(19) Bruhl, C.; Lelieveld, J.; Crutzen, P. J.; Tost, H. *Atmos Chem Phys* **2012**, *12*, 1239.

(20) Wilcox, E. M. *Atmos Chem Phys* **2012**, *12*, 139.

(21) Stock, M.; Cheng, Y. F.; Birmili, W.; Massling, A.; Wehner, B.; Muller, T.; Leinert, S.; Kalivitis, N.; Mihalopoulos, N.; Wiedensohler, A. *Atmos Chem Phys* **2011**, *11*, 4251.

(22) Skeie, R. B.; Berntsen, T. K.; Myhre, G.; Tanaka, K.; Kvalevag, M. M.; Hoyle, C. R. *Atmos Chem Phys* **2011**, *11*, 11827.

(23) Bauer, S. E.; Menon, S.; Koch, D.; Bond, T. C.; Tsigaridis, K. *Atmos Chem Phys* **2010**, *10*, 7439.

(24) Carbone, C.; Decesari, S.; Mircea, M.; Giulianelli, L.; Finessi, E.; Rinaldi, M.; Fuzzi, S.; Marinoni, A.; Duchi, R.; Perrino, C.; Sargolini, T.; Vardè, M.; Sprovieri, F.; Gobbi, G. P.; Angelini, F.; Facchini, M. C. *Atmos Environ* **2010**, *44*, 5269.

(25) Ma, X.; Yu, F.; Luo, G. *Atmos Chem Phys* **2012**, *12*, 5563.

(26) Leibensperger, E. M.; Mickley, L. J.; Jacob, D. J.; Chen, W. T.; Seinfeld, J. H.; Nenes, A.; Adams, P. J.; Streets, D. G.; Kumar, N.; Rind, D. *Atmos Chem Phys* **2012**, *12*, 3333.

(27) Carpenter, L. J.; Archer, S. D.; Beale, R. *Chem Soc Rev* **2012**, *41*, 6473.

(28) Andreae, M. O.; Jones, C. D.; Cox, P. M. *Nature* **2005**, *435*, 1187.

(29) Borsos, T.; Rimnacova, D.; Zdimal, V.; Smolik, J.; Wagner, Z.; Weidinger, T.; Burkart, J.; Steiner, G.; Reischl, G.; Hitzenberger, R.; Schwarz, J.; Salma, I. *Sci Total Environ* **2012**, *433*, 418.

(30) Hu, D.; Chen, J.; Ye, X.; Li, L.; Yang, X. *Atmos Environ* **2011**, *45*, 2349.

(31) Ghorai, S.; Tivanski, A. V. *Anal Chem* **2010**, *82*, 9289.

(32) Ferrero, L.; Mocnik, G.; Ferrini, B. S.; Perrone, M. G.; Sangiorgi, G.; Bolzacchini, E. *Sci Total Environ* **2011**, *409*, 2824.

(33) Moore, R. H.; Cerully, K.; Bahreini, R.; Brock, C. A.; Middlebrook, A. M.; Nenes, A. *J Geophys Res-Atmos* **2012**, *117*.

(34) Posfai, M.; Buseck, P. R. *Annu Rev Earth Pl Sc* **2010**, *38*, 17.

(35) Haddrell, A. E.; Davies, J. F.; Yabushita, A.; Reid, J. P. *The Journal of Physical Chemistry A* **2012**, *116*, 9941.

(36) Dockery, D. W.; Pope, C. A. *Annu Rev Publ Health* **1994**, *15*, 107.

(37) Ramanathan, V.; Carmichael, G. *Nat Geosci* **2008**, *1*, 221.

(38) Andreae, M. O.; Rosenfeld, D. *Earth-Sci Rev* **2008**, *89*, 13.

(39) Koehler, K. A.; DeMott, P. J.; Kreidenweis, S. M.; Popovicheva, O. B.; Petters, M. D.; Carrico, C. M.; Kireeva, E. D.; Khokhlova, T. D.; Shonija, N. K. *Phys Chem Chem Phys* **2009**, *11*, 7906.

(40) Lammel, G.; Novakov, T. *Atmos Environ* **1995**, *29*, 813.

(41) Dusek, U.; Reischl, G. P.; Hitzenberger, R. *Environ Sci Technol* **2006**, *40*, 1223.

(42) Bahadur, R.; Russell, L. M.; Jacobson, M. Z.; Prather, K.; Nenes, A.; Adams, P.; Seinfeld, J. H. *J Geophys Res-Atmos* **2012**, *117*.

(43) Sorooshian, A.; Csavina, J.; Shingler, T.; Dey, S.; Brechtel, F. J.; Sáez, A. E.; Betterton, E. A. *Environ Sci Technol* **2012**, *46*, 9473.

(44) Byron, P. R.; Davis, S. S.; Bubb, M. D.; Cooper, P. *Pestic Sci* **1977**, *8*, 521.

(45) Heyder, J.; Gebhart, J.; Rudolf, G.; Schiller, C. F.; Stahlhofen, W. *J Aerosol Sci* **1986**, *17*, 811.

(46) Martin, S. T. *Chem Rev* **2000**, *100*, 3403.

(47) Turšič, J.; Podkrajšek, B.; Grgić, I.; Ctyroky, P.; Berner, A.; Dusek, U.; Hitzenberger, R. *Chemosphere* **2006**, *63*, 1193.

(48) Pang, Y.; Turpin, B. J.; Gundel, L. A. *Aerosol Sci Tech* **2006**, *40*, 128.

(49) Bizjak, M.; Grgic, I.; Hudnik, V. *Chemosphere* **1999**, *38*, 1233.

(50) Stohr, J. *NEXAFS Spectroscopy*; Springer-Verlag: New York, 1991.

(51) Cody, G. D.; Ade, H.; Wirick, S.; Mitchell, G. D.; Davis, A. *Org Geochem* **1998**, *28*, 441.

(52) Lee, V.; Dennis, R. V.; Schultz, B. J.; Jaye, C.; Fischer, D. A.; Banerjee, S. *J Phys Chem C* **2012**, *116*, 20591.

(53) Saito, S. L. *Theor Chem Acc* **2006**, *115*, 281.

(54) Smith, A. P.; Laurer, J. H.; Ade, H. W.; Smith, S. D.; Ashraf, A.; Spontak, R. J. *Macromolecules* **1997**, *30*, 663.

(55) Harald, A.; Urquhart, S. G. 2002, p 285.

(56) Wang, J.; Hitchcock, A. P.; Karunakaran, C.; Prange, A.; Harkness, T.; Lu, Y.; Obst, M.; Hormes, J. *Aip Conf Proc* **2011**, *1365*, 215.

(57) Hitchcock, A. P.; Johansson, G. A.; Mitchell, G. E.; Keefe, M. H.; Tyliszcak, T. *Appl Phys a-Mater* **2008**, *92*, 447.

(58) Tivanski, A. V.; Hopkins, R. J.; Tyliszczak, T.; Gilles, M. K. *J Phys Chem A* **2007**, *111*, 5448.

(59) Malliaras, G. G. *Biochimica et Biophysica Acta (BBA) - General Subjects*.

(60) Shinar, J. *Nat Mater* **2012**, *11*, 663.

(61) Li, R. J.; Hu, W. P.; Liu, Y. Q.; Zhu, D. B. *Accounts Chem Res* **2010**, *43*, 529.

(62) Gao, J. H.; Li, R. J.; Li, L. Q.; Meng, Q.; Jiang, H.; Li, H. X.; Hu, W. P. *Adv Mater* **2007**, *19*, 3008.

(63) Kwon, E.; Chung, H. R.; Araki, Y.; Kasai, H.; Oikawa, H.; Ito, O.; Nakanishi, H. *Chem Phys Lett* **2007**, *441*, 106.

(64) Karunatilaka, C.; Bucar, D. K.; Ditzler, L. R.; Friscic, T.; Swenson, D. C.; MacGillivray, L. R.; Tivanski, A. V. *Angew Chem Int Edit* **2011**, *50*, 8642.

(65) Natali, D.; Caironi, M. *Adv Mater* **2012**, *24*, 1357.

(66) Bobbert, P. A.; Sharma, A.; Mathijssen, S. G. J.; Kemerink, M.; de Leeuw, D. M. *Adv Mater* **2012**, *24*, 1146.

(67) Sokolov, A. N.; Tee, B. C. K.; Bettinger, C. J.; Tok, J. B. H.; Bao, Z. N. *Accounts Chem Res* **2012**, *45*, 361.

(68) Farinola, G. M.; Ragni, R. *Chem Soc Rev* **2011**, *40*, 3467.

(69) Yook, K. S.; Lee, J. Y. *Adv Mater* **2012**, *24*, 3169.

(70) Kalyani, N. T.; Dhoble, S. J. *Renew Sust Energ Rev* **2012**, *16*, 2696.

(71) DeFranco, J. A.; Schmidt, B. S.; Lipson, M.; Malliaras, G. G. *Org Electron* **2006**, *7*, 22.

(72) Reichmanis, E.; Nalamasu, O.; Houlihan, F. M. *Accounts Chem Res* **1999**, *32*, 659.

(73) Lim, Y. F.; Lee, J. K.; Zakhidov, A. A.; DeFranco, J. A.; Fong, H. H.; Taylor, P. G.; Ober, C. K.; Malliaras, G. G. *J Mater Chem* **2009**, *19*, 5394.

(74) Dal Zilio, S.; Tvingstedt, K.; Inganas, O.; Tormen, M. *Microelectron Eng* **2009**, *86*, 1150.

(75) Lewis, J.; Zhang, J.; Jiang, X. M. *J Renew Sustain Ener* **2009**, *1*.

(76) Maltsev, E. I.; Lypenko, D. A.; Bobinkin, V. V.; Tameev, A. R.; Kirillov, S. V.; Shapiro, B. I.; Schoo, H. F. M.; Vannikov, A. V. *Appl Phys Lett* **2002**, *81*, 3088.

(77) Kwon, E.; Chung, H. R.; Kasai, H.; Oikawa, H.; Nakanishi, H. *Mol Cryst Liq Cryst* **2012**, *566*, 147.

(78) Philippot, C.; Dubois, F.; Maurin, M.; Boury, B.; Prat, A.; Ibanez, A. *J Mater Chem* **2012**, *22*, 11370.

(79) Friscic, T.; MacGillivray, L. R. *Z Kristallogr* **2005**, *220*, 351.

(80) Garcia-Garibay, M. A. *Angewandte Chemie International Edition* **2007**, *46*, 8945.

(81) Macgillivray, L. R.; Papaefstathiou, G. S.; Friscic, T.; Hamilton, T. D.; Bucar, D. K.; Chu, Q.; Varshney, D. B.; Georgiev, I. G. *Accounts Chem Res* **2008**, *41*, 280.

(82) Shan, N.; Zaworotko, M. J. *Drug Discov Today* **2008**, *13*, 440.

(83) MacGillivray, L. R.; Reid, J. L.; Ripmeester, J. A. *J Am Chem Soc* **2000**, *122*, 7817.

(84) Toh, N. L.; Nagarathinam, M.; Vittal, J. J. *Angew Chem Int Edit* **2005**, *44*, 2237.

(85) Kawata, S.; Kawata, Y. *Chem Rev* **2000**, *100*, 1777.

(86) Feringa, B. L.; van Delden, R. A.; Koumura, N.; Geertsema, E. M. *Chem Rev* **2000**, *100*, 1789.

(87) Hickey, M. B.; Peterson, M. L.; Scoppettuolo, L. A.; Morrisette, S. L.; Vetter, A.; Guzmán, H.; Remenar, J. F.; Zhang, Z.; Tawa, M. D.; Haley, S.; Zaworotko, M. J.; Almarsson, Ö. *European Journal of Pharmaceutics and Biopharmaceutics* **2007**, *67*, 112.

(88) Fleischman, S. G.; Kuduva, S. S.; McMahon, J. A.; Moulton, B.; Walsh, R. D. B.; Rodriguez-Hornedo, N.; Zaworotko, M. J. *Cryst Growth Des* **2003**, *3*, 909.

(89) Childs, S. L.; Chyall, L. J.; Dunlap, J. T.; Smolenskaya, V. N.; Stahly, B. C.; Stahly, G. P. *J Am Chem Soc* **2004**, *126*, 13335.

(90) Irie, M. *Chem Rev* **2000**, *100*, 1685.

(91) Li, F.; Zhuang, J. P.; Jiang, G. Y.; Tang, H. H.; Xia, A. D.; Jiang, L.; Song, Y. L.; Li, Y. L.; Zhu, D. B. *Chem Mater* **2008**, *20*, 1194.

(92) Mcbride, J. M.; Segmuller, B. E.; Hollingsworth, M. D.; Mills, D. E.; Weber, B. A. *Science* **1986**, *234*, 830.

(93) Peachey, N. M.; Eckhardt, C. J. *J Phys Chem-Us* **1993**, *97*, 10849.

(94) Al-Kaysi, R. O.; Muller, A. M.; Bardeen, C. J. *J Am Chem Soc* **2006**, *128*, 15938.

(95) Stephanou, E. G. *Nature* **2005**, *434*, 31.

(96) Andreae, M. O.; Crutzen, P. J. *Science* **1997**, *276*, 1052.

(97) Jimenez, J. L.; Canagaratna, M. R.; Donahue, N. M.; Prevot, A. S. H.; Zhang, Q.; Kroll, J. H.; DeCarlo, P. F.; Allan, J. D.; Coe, H.; Ng, N. L.; Aiken, A. C.; Docherty, K. S.; Ulbrich, I. M.; Grieshop, A. P.; Robinson, A. L.; Duplissy, J.; Smith, J. D.; Wilson, K. R.; Lanz, V. A.; Hueglin, C.; Sun, Y. L.; Tian, J.; Laaksonen, A.; Raatikainen, T.; Rautiainen, J.; Vaattovaara, P.; Ehn, M.; Kulmala, M.; Tomlinson, J. M.; Collins, D. R.; Cubison, M. J.; Dunlea, E. J.; Huffman, J. A.; Onasch, T. B.; Alfarra, M. R.; Williams, P. I.; Bower, K.; Kondo, Y.; Schneider, J.; Drewnick, F.; Borrmann, S.; Weimer, S.; Demerjian, K.; Salcedo, D.; Cottrell, L.; Griffin, R.; Takami, A.; Miyoshi, T.; Hatakeyama, S.; Shimono, A.; Sun, J. Y.; Zhang, Y. M.; Dzepina, K.; Kimmel, J. R.; Sueper, D.; Jayne, J. T.; Herndon, S. C.; Trimborn, A. M.; Williams, L. R.; Wood, E. C.; Middlebrook, A. M.; Kolb, C. E.; Baltensperger, U.; Worsnop, D. R. *Science* **2009**, *326*, 1525.

(98) Pandis, S. N.; Wexler, A. S.; Seinfeld, J. H. *J Phys Chem-Us* **1995**, *99*, 9646.

(99) Harrison, R. M.; Yin, J. X. *Sci Total Environ* **2000**, *249*, 85.

(100) Sekiguchi, M.; Nakajima, T.; Suzuki, K.; Kawamoto, K.; Higurashi, A.; Rosenfeld, D.; Sano, I.; Mukai, S. *J Geophys Res-Atmos* **2003**, *108*.

(101) Penner, J. E.; Quaas, J.; Storelvmo, T.; Takemura, T.; Boucher, O.; Guo, H.; Kirkevag, A.; Kristjansson, J. E.; Seland, O. *Atmos Chem Phys* **2006**, *6*, 3391.

(102) Petters, M. D.; Kreidenweis, S. M. *Atmos Chem Phys* **2007**, *7*, 1961.

(103) Oh, H.; Park, H.; Kim, S. *Aerosol Sci Tech* **2004**, *38*, 1045.

(104) Tang, I. N. *J Geophys Res-Atmos* **1996**, *101*, 19245.

(105) Naira, P. R.; George, S. K.; Sunilkumara, S. V.; Parameswarana, K.; Jacob, S.; Abraham, A. *Atmos Environ* **2006**, *40*, 6477.

(106) Jacobson, M. Z. *Nature* **2001**, *409*, 695.

(107) Rissler, J.; Vestin, A.; Swietlicki, E.; Fisch, G.; Zhou, J.; Artaxo, P.; Andreae, M. O. *Atmos Chem Phys* **2006**, *6*, 471.

(108) Aggarwal, S. G.; Mochida, M.; Kitamori, Y.; Kawamura, K. *Environ Sci Technol* **2007**, *41*, 6920.

(109) Hu, D. W.; Qiao, L. P.; Chen, J. M.; Ye, X. N.; Yang, X.; Cheng, T. T.; Fang, W. *Aerosol Air Qual Res* **2010**, *10*, 255.

(110) Sinclair, D.; Countess, R. J.; Hoopes, G. S. *Atmos Environ* **1974**, *8*, 1111.

(111) Minambres, L.; Sanchez, M. N.; Castano, F.; Basterretxea, F. J. *J Phys Chem A* **2010**, *114*, 6124.

(112) Asmi, E.; Frey, A.; Virkkula, A.; Ehn, M.; Manninen, H. E.; Timonen, H.; Tolonen-Kivimaki, O.; Aurela, M.; Hillamo, R.; Kulmala, M. *Atmos Chem Phys* **2010**, *10*, 4253.

(113) Abel, S. J.; Highwood, E. J.; Haywood, J. M.; Stringer, M. A. *Atmos Chem Phys* **2005**, *5*, 1999.

(114) Bellouin, N.; Boucher, O.; Haywood, J.; Reddy, M. S. *Nature* **2005**, *438*, 1138.

(115) Prince, A. P.; Kleiber, P. D.; Grassian, V. H.; Young, M. A. *Phys Chem Chem Phys* **2008**, *10*, 142.

(116) Liu, Y.; Gibson, E. R.; Cain, J. P.; Wang, H.; Grassian, V. H.; Laskin, A. *J Phys Chem A* **2008**, *112*, 1561.

(117) Lee, A. K. Y.; Chan, C. K. *Atmos Environ* **2007**, *41*, 4611.

(118) Geng, H.; Ryu, J.; Jung, H. J.; Chung, H.; Ahn, K. H.; Ro, C. U. *Environ Sci Technol* **2010**, *44*, 2348.

(119) Anttila, T.; Vaattovaara, P.; Komppula, M.; Hyvarinen, A. P.; Lihavainen, H.; Kerminen, V. M.; Laaksonen, A. *Atmos Chem Phys* **2009**, *9*, 4841.

(120) Eichler, H.; Cheng, Y. F.; Birmili, W.; Nowak, A.; Wiedensohler, A.; Bruggemann, E.; Gnauk, T.; Herrmann, H.; Althausen, D.; Ansmann, A.; Engelmann, R.;

Tesche, M.; Wendisch, M.; Zhang, Y. H.; Hu, M.; Liu, S.; Zeng, L. M. *Atmos Environ* **2008**, *42*, 6321.

(121) Onasch, T. B.; Siefert, R. L.; Brooks, S. D.; Prenni, A. J.; Murray, B.; Wilson, M. A.; Tolbert, M. A. *J Geophys Res-Atmos* **1999**, *104*, 21317.

(122) Biskos, G.; Paulsen, D.; Russell, L. M.; Buseck, P. R.; Martin, S. T. *Atmos Chem Phys* **2006**, *6*, 4633.

(123) Hoffman, R. C.; Laskin, A.; Finlayson-Pitts, B. J. *J Aerosol Sci* **2004**, *35*, 869.

(124) Wise, M. E.; Martin, S. T.; Russell, L. M.; Buseck, P. R. *Aerosol Sci Tech* **2008**, *42*, 281.

(125) Liu, Y.; Yang, Z. W.; Desyaterik, Y.; Gassman, P. L.; Wang, H.; Laskin, A.; Kim, S. J.; Han, J. *Anal Chem* **2008**, *80*, 7179.

(126) Hennig, T.; Massling, A.; Brechtel, F. J.; Wiedensohler, A. *J Aerosol Sci* **2005**, *36*, 1210.

(127) Peng, C.; Chan, M. N.; Chan, C. K. *Environ Sci Technol* **2001**, *35*, 4495.

(128) Yeung, M. C.; Chan, C. K. *Aerosol Sci Tech* **2010**, *44*, 269.

(129) Chand, D.; Guyon, P.; Artaxo, P.; Schmid, O.; Frank, G. P.; Rizzo, L. V.; Mayol-Bracero, O. L.; Gatti, L. V.; Andreae, M. O. *Atmos Chem Phys* **2006**, *6*, 2911.

(130) Murphy, S. M.; Sorooshian, A.; Kroll, J. H.; Ng, N. L.; Chhabra, P.; Tong, C.; Surratt, J. D.; Knipping, E.; Flagan, R. C.; Seinfeld, J. H. *Atmos Chem Phys* **2007**, *7*, 2313.

(131) Ling, T. Y.; Chan, C. K. *J Geophys Res-Atmos* **2008**, *113*.

(132) de Smit, E.; Swart, I.; Creemer, J. F.; Hoveling, G. H.; Gilles, M. K.; Tyliszczak, T.; Kooyman, P. J.; Zandbergen, H. W.; Morin, C.; Weckhuysen, B. M.; de Groot, F. M. F. *Nature* **2008**, *456*, 222.

(133) Muntean, L.; Planques, R.; Kilcoyne, A. L. D.; Leone, S. R.; Gilles, M. K.; Hinsberg, W. D. *J Vac Sci Technol B* **2005**, *23*, 1630.

(134) Videen, G.; Pellegrino, P.; Ngo, D.; Nachman, P.; Pinnick, R. G. *Appl Optics* **1997**, *36*, 3532.

(135) Hopkins, R. J.; Desyaterik, Y.; Tivanski, A. V.; Zaveri, R. A.; Berkowitz, C. M.; Tyliszczak, T.; Gilles, M. K.; Laskin, A. *J Geophys Res-Atmos* **2008**, *113*.

(136) Moffet, R. C.; Desyaterik, Y.; Hopkins, R. J.; Tivanski, A. V.; Gilles, M. K.; Wang, Y.; Shutthanandan, V.; Molina, L. T.; Abraham, R. G.; Johnson, K. S.; Mugica, V.; Molina, M. J.; Laskin, A.; Prather, K. A. *Environ Sci Technol* **2008**, *42*, 7091.

(137) Zaveri, R. A.; Berkowitz, C. M.; Brechtel, F. J.; Gilles, M. K.; Hubbe, J. M.; Jayne, J. T.; Kleinman, L. I.; Laskin, A.; Madronich, S.; Onasch, T. B.; Pekour, M. S.; Springston, S. R.; Thornton, J. A.; Tivanski, A. V.; Worsnop, D. R. *J Geophys Res-Atmos* **2010**, *115*.

(138) Takahama, S.; Gilardoni, S.; Russell, L. M. *J Geophys Res-Atmos* **2008**, *113*.

(139) Buijs, K.; Maurice, M. J. *Anal Chim Acta* **1969**, *47*, 469.

(140) Ma, Y.; Chen, C. T.; Meigs, G.; Randall, K.; Sette, F. *Phys Rev A* **1991**, *44*, 1848.

(141) Rahn, H.; Hammel, H. T. *Polar Biol* **1982**, *1*, 91.

(142) Wilson, K. R.; Rude, B. S.; Catalano, T.; Schaller, R. D.; Tobin, J. G.; Co, D. T.; Saykally, R. J. *J Phys Chem B* **2001**, *105*, 3346.

(143) Kim, D. Y.; Lee, K.; Ma, C. I.; Mahalingam, M.; Hanson, D. M.; Hulbert, S. L. *J Chem Phys* **1992**, *97*, 5915.

(144) Myneni, S.; Luo, Y.; Naslund, L. A.; Cavalleri, M.; Ojamae, L.; Ogasawara, H.; Pelmenschikov, A.; Wernet, P.; Vaterlein, P.; Heske, C.; Hussain, Z.; Pettersson, L. G. M.; Nilsson, A. *J Phys-Condens Mat* **2002**, *14*, L213.

(145) Diercksen, G. H. F.; Kraemer, W. P.; Rescigno, T. N.; Bender, C. F.; Mckoy, B. V.; Langhoff, S. R.; Langhoff, P. W. *J Chem Phys* **1982**, *76*, 1043.

(146) Iwata, N.; Tani, K.; Watada, A.; Ikeura-Sekiguchi, H.; Araki, T.; Hitchcock, A. P. *Micron* **2006**, *37*, 290.

(147) Wise, M. E.; Biskos, G.; Martin, S. T.; Russell, L. M.; Buseck, P. R. *Aerosol Sci Tech* **2005**, *39*, 849.

(148) Rogers, C. F.; Watson, J. G.; Day, D.; Oraltay, R. G. *Aerosol Sci Tech* **1998**, *29*, 557.

(149) Lee, C. T.; Chang, S. Y. *Atmos Environ* **2002**, *36*, 1883.

(150) Saxena, P.; Hildemann, L. M.; Mcmurry, P. H.; Seinfeld, J. H. *J Geophys Res-Atmos* **1995**, *100*, 18755.

(151) Galwey, A. K. *J Therm Anal Calorim* **2005**, *82*, 23.

(152) Lide, D. R. *Handbook of Chemistry and Physics*; 78 ed.; CRC Press: Boca Raton, FL, 1997.

(153) Tang, I. N.; Munkelwitz, H. R. *J Geophys Res-Atmos* **1994**, *99*, 18801.

(154) Cappa, C. D.; Smith, J. D.; Wilson, K. R.; Messer, B. M.; Gilles, M. K.; Cohen, R. C.; Saykally, R. J. *J Phys Chem B* **2005**, *109*, 7046.

(155) Hetenyi, B.; De Angelis, F.; Giannozzi, P.; Car, R. *J Chem Phys* **2004**, *120*, 8632.

(156) Faubel, M.; Steiner, B.; Toennies, J. P. *J Chem Phys* **1997**, *106*, 9013.

(157) Ghosal, S.; Hemminger, J. C.; Bluhm, H.; Mun, B. S.; Hebenstreit, E. L. D.; Ketteler, G.; Ogletree, D. F.; Requejo, F. G.; Salmeron, M. *Science* **2005**, *307*, 563.

(158) Jungwirth, P.; Tobias, D. J. *J Phys Chem B* **2002**, *106*, 6361.

(159) Moyers, J. L.; Duce, R. A. *Anal Chim Acta* **1974**, *69*, 117.

(160) Pyle, D. M.; Mather, T. A. *Chem Geol* **2009**, *263*, 110.

(161) Krieger, U. K.; Marcolli, C.; Reid, J. P. *Chem Soc Rev* **2012**, *41*, 6631.

(162) Ma, Q. X.; Liu, Y. C.; Liu, C.; Ma, J. Z.; He, H. *J Environ Sci-China* **2012**, *24*, 62.

(163) Cwiertny, D. M.; Young, M. A.; Grassian, V. H. *Annu Rev Phys Chem* **2008**, *59*, 27.

(164) Hanke, M.; Umann, B.; Uecker, J.; Arnold, F.; Bunz, H. *Atmos Chem Phys* **2003**, *3*, 417.

(165) Ramanathan, V.; Crutzen, P. J.; Kiehl, J. T.; Rosenfeld, D. *Science* **2001**, *294*, 2119.

(166) Usher, C. R.; Al-Hosney, H.; Carlos-Cuellar, S.; Grassian, V. H. *J Geophys Res-Atmos* **2002**, *107*.

(167) Zamora, I. R.; Tabazadeh, A.; Golden, D. M.; Jacobson, M. Z. *J Geophys Res-Atmos* **2011**, *116*.

(168) Perraud, V.; Bruns, E. A.; Ezell, M. J.; Johnson, S. N.; Yu, Y.; Alexander, M. L.; Zelenyuk, A.; Imre, D.; Chang, W. L.; Dabdub, D.; Pankow, J. F.; Finlayson-Pitts, B. J. *P Natl Acad Sci USA* **2012**, *109*, 2836.

(169) Attwood, A. R.; Greenslade, M. E. *J Phys Chem A* **2012**, *116*, 4518.

(170) Shi, Y.; Ge, M.; Wang, W. *Atmos Environ* **2012**, *60*, 9.

(171) Liu, Y.; Laskin, A. *J Phys Chem A* **2009**, *113*, 1531.

(172) Laskin, A.; Cowin, J. P.; Iedema, M. J. *J Electron Spectrosc* **2006**, *150*, 260.

(173) Ghorai, S.; Laskin, A.; Tivanski, A. V. *J Phys Chem A* **2011**, *115*, 4373.

(174) Hansson, H. C.; Rood, M. J.; Koloutsou-Vakakis, S.; Hameri, K.; Orsini, D.; Wiedensohler, A. *J Atmos Chem* **1998**, *31*, 321.

(175) Ma, Q. X.; Liu, Y. C.; He, H. *J Phys Chem A* **2010**, *114*, 4232.

(176) Yeung, M. C.; Ling, T. Y.; Chan, C. K. *J Phys Chem A* **2010**, *114*, 898.

(177) Ganguly, S.; Fernandes, J. R.; Desiraju, G. R.; Rao, C. N. R. *Chem Phys Lett* **1980**, *69*, 227.

(178) Li, L.; Dou, Q. *Polym Composite* **2010**, *31*, 966.

(179) Macoas, E. M. S.; Fausto, R.; Lundell, J.; Pettersson, M.; Khriachtchev, L.; Rasanen, M. *J Phys Chem A* **2000**, *104*, 11725.

(180) Serjeant, E. P. *Ionization Constants of Organic Acids in Aqueous Solution*; Oxford: New York, 1979.

(181) Liu, J. A.; Takada, R.; Karita, S.; Watanabe, T.; Honda, Y.; Watanabe, T. *Bioresource Technol* **2010**, *101*, 9355.

(182) Najera, J. J.; Horn, A. B. *Phys Chem Chem Phys* **2009**, *11*, 483.

(183) Dinar, E.; Mentel, T. F.; Rudich, Y. *Atmos Chem Phys* **2006**, *6*, 5213.

(184) Herich, H.; Kammermann, L.; Friedman, B.; Gross, D. S.; Weingartner, E.; Lohmann, U.; Spichtinger, P.; Gysel, M.; Baltensperger, U.; Cziczo, D. J. *J Geophys Res-Atmos* **2009**, *114*.

(185) Sloane, C. S. *Atmos Environ* **1986**, *20*, 1025.

(186) Wang, J.; Cubison, M. J.; Aiken, A. C.; Jimenez, J. L.; Collins, D. R. *Atmos Chem Phys* **2010**, *10*, 7267.

(187) Ward, D. S.; Eidhammer, T.; Cotton, W. R.; Kreidenweis, S. M. *Atmos Chem Phys* **2010**, *10*, 5435.

(188) Peng, L. L.; Wang, Y. H. *Nanoscale Res Lett* **2010**, *5*, 839.

(189) Buscher, K.; Helm, C. A.; Gross, C.; Glockl, G.; Romanus, E.; Weitschies, W. *Langmuir* **2004**, *20*, 2435.

(190) Ringe, E.; McMahon, J. M.; Sohn, K.; Cobley, C.; Xia, Y. N.; Huang, J. X.; Schatz, G. C.; Marks, L. D.; Van Duyne, R. P. *J Phys Chem C* **2010**, *114*, 12511.

(191) Hanel, G.; Thudium, J. *Pure Appl Geophys* **1977**, *115*, 799.

(192) Kelly, W. P.; Mcmurry, P. H. *Aerosol Sci Tech* **1992**, *17*, 199.

(193) McMurry, P. H.; Wang, X.; Park, K.; Ehara, K. *Aerosol Sci Tech* **2002**, *36*, 227.

(194) DeCarlo, P. F.; Slowik, J. G.; Worsnop, D. R.; Davidovits, P.; Jimenez, J. L. *Aerosol Sci Tech* **2004**, *38*, 1185.

(195) Malloy, Q. G. J.; Nakao, S.; Qi, L.; Austin, R.; Stothers, C.; Hagino, H.; Cocker, D. R. *Aerosol Sci Tech* **2009**, *43*, 673.

(196) Shilling, J. E.; Chen, Q.; King, S. M.; Rosenoern, T.; Kroll, J. H.; Worsnop, D. R.; DeCarlo, P. F.; Aiken, A. C.; Sueper, D.; Jimenez, J. L.; Martin, S. T. *Atmos Chem Phys* **2009**, *9*, 771.

(197) Zordan, C. A.; Pennington, M. R.; Johnston, M. V. *Anal Chem* **2010**, *82*, 8034.

(198) Coz, E.; Gomez-Moreno, F. J.; Casuccio, G. S.; Artinano, B. *J Geophys Res-Atmos* **2010**, *115*.

(199) Hamilton, T. D.; Bucar, D. K.; Baltrusaitis, J.; Flanagan, D. R.; Li, Y. J.; Ghorai, S.; Tivanski, A. V.; MacGillivray, L. R. *J Am Chem Soc* **2011**, *133*, 3365.

(200) Preobrajenski, A. B.; Vinogradov, A. S.; Molodtsov, S. L.; Krasnikov, S. K.; Chasse, T.; Szargan, R.; Laubschat, C. *Phys Rev B* **2002**, *65*.

(201) Torok, S.; Osan, J.; Beckhoff, B.; Ulm, G. *Powder Diffr* **2004**, *19*, 81.

(202) Outka, D. A.; Stohr, J.; Madix, R. J.; Rotermund, H. H.; Hermsmeier, B.; Solomon, J. *Surf Sci* **1987**, *185*, 53.

(203) Ishii, I.; Hitchcock, A. P. *J Electron Spectrosc* **1988**, *46*, 55.

(204) Prince, K. C.; Richter, R.; de Simone, M.; Alagia, M.; Coreno, M. *J Phys Chem A* **2003**, *107*, 1955.

(205) Lin, P.; Engling, G.; Yu, J. Z. *Atmos Chem Phys* **2010**, *10*, 6487.

(206) Salma, I.; Meszaros, T.; Maenhaut, W.; Vass, E.; Majer, Z. *Atmos Chem Phys* **2010**, *10*, 1315.

(207) Schumacher, M.; Christl, I.; Scheinost, A. C.; Jacobsen, C.; Kretzschmar, R. *Environ Sci Technol* **2005**, *39*, 9094.

(208) Guyon, P.; Graham, B.; Beck, J.; Boucher, O.; Gerasopoulos, E.; Mayol-Bracero, O. L.; Roberts, G. C.; Artaxo, P.; Andreae, M. O. *Atmos Chem Phys* **2003**, *3*, 951.

(209) Malm, W. C.; Day, D. E.; Carrico, C.; Kreidenweis, S. M.; Collett, J. L.; McMeeking, G.; Lee, T.; Carrillo, J.; Schichtel, B. *J Geophys Res-Atmos* **2005**, *110*.

(210) Reemtsma, T.; These, A.; Springer, A.; Linscheid, M. *Water Res* **2008**, *42*, 63.

(211) Chan, M. N.; Chan, C. K. *Environ Sci Technol* **2003**, *37*, 5109.

(212) Coakley, J. A.; Cess, R. D.; Yurevich, F. B. *J Atmos Sci* **1983**, *40*, 116.

(213) Charlson, R. J.; Lovelock, J. E.; Andreae, M. O.; Warren, S. G. *Nature* **1987**, *326*, 655.

(214) Berico, M.; Luciani, A.; Formignani, M. *Atmos Environ* **1997**, *31*, 3659.

(215) Cruz, C. N.; Pandis, S. N. *Environ Sci Technol* **2000**, *34*, 4313.

(216) Lesins, G.; Chylek, P.; Lohmann, U. *J Geophys Res-Atmos* **2002**, *107*.

(217) Yoon, S. C.; Kim, J. *Atmos Environ* **2006**, *40*, 4328.

(218) Moffet, R. C.; Prather, K. A. *P Natl Acad Sci USA* **2009**, *106*, 11872.

(219) Gill, P. S.; Graedel, T. E.; Weschler, C. J. *Rev Geophys* **1983**, *21*, 903.

(220) Bi, X. H.; Zhang, G. H.; Li, L.; Wang, X. M.; Li, M.; Sheng, G. Y.; Fu, J. M.; Zhou, Z. *Atmos Environ* **2011**, *45*, 3447.

(221) Okada, K.; Ikegami, M.; Zaizen, Y.; Tsutsumi, Y.; Makino, Y.; Jensen, J. B.; Gras, J. L. *Atmos Environ* **2005**, *39*, 5079.

(222) Posfai, M.; Anderson, J. R.; Buseck, P. R.; Sievering, H. *J Geophys Res-Atmos* **1999**, *104*, 21685.

(223) Posfai, M.; Simonics, R.; Li, J.; Hobbs, P. V.; Buseck, P. R. *J Geophys Res-Atmos* **2003**, *108*.

(224) Katrinak, K. A.; Rez, P.; Buseck, P. R. *Environ Sci Technol* **1992**, *26*, 1967.

(225) Yeung, M. C.; Lee, A. K. Y.; Chan, C. K. *Aerosol Sci Tech* **2009**, *43*, 387.

(226) Ruozi, B.; Tosi, G.; Tonelli, M.; Bondioli, L.; Mucci, A.; Forni, F.; Vandelli, M. A. *J Liposome Res* **2009**, *19*, 59.

(227) Schmitz, I.; Schreiner, M.; Friedbacher, G.; Grasserbauer, M. *Appl Surf Sci* **1997**, *115*, 190.

(228) Keita, B.; Nadjo, L.; Gachard, E.; Remita, H.; Khatouri, J.; Belloni, J. *New J Chem* **1997**, *21*, 851.

(229) O'Neil, K. D.; Semenikhin, O. A. *J Phys Chem C* **2007**, *111*, 14823.

(230) Podkrajsek, B.; Grgic, I.; Tursic, J.; Bercic, G. *J Atmos Chem* **2006**, *54*, 103.

(231) Glasius, M.; Lahaniati, M.; Calogirou, A.; Di Bella, D.; Jensen, N. R.; Hjorth, J.; Kotzias, D.; Larsen, B. R. *Environ Sci Technol* **2000**, *34*, 1001.

(232) Salo, K.; Jonsson, A. M.; Andersson, P. U.; Hallquist, M. *J Phys Chem A* **2010**, *114*, 4586.

(233) Post, D.; Bridgman, H. A.; Ayers, G. P. *J Atmos Chem* **1991**, *13*, 83.

(234) Kumar, N.; Kulshrestha, U. C.; Saxena, A.; Kumari, K. M.; Srivastava, S. S. *J Geophys Res-Atmos* **1993**, *98*, 5135.

(235) Kawamura, K.; Steinberg, S.; Ng, L.; Kaplan, I. R. *Atmos Environ* **2001**, *35*, 3917.

(236) Gunz, D. W.; Hoffmann, M. R. *Atmos Environ a-Gen* **1990**, *24*, 1673.

(237) Khwaja, H. A. *Atmos Environ* **1995**, *29*, 127.

(238) Bardouki, H.; Liakakou, H.; Economou, C.; Sciare, J.; Smolik, J.; Zdimal, V.; Eleftheriadis, K.; Lazaridis, M.; Dye, C.; Mihalopoulos, N. *Atmos Environ* **2003**, *37*, 195.

(239) Kawamura, K.; Umemoto, N.; Mochida, M.; Bertram, T.; Howell, S.; Huebert, B. J. *J Geophys Res-Atmos* **2003**, *108*.

(240) Yao, X. H.; Fang, M.; Chan, C. K.; Ho, K. F.; Lee, S. C. *Atmos Environ* **2004**, *38*, 963.

(241) Karcher, B.; Koop, T. *Atmos Chem Phys* **2005**, *5*, 703.

(242) Lohmann, U.; Feichter, J. *Atmos Chem Phys* **2005**, *5*, 715.

(243) Kawamura, K.; Sakaguchi, F. *J Geophys Res-Atmos* **1999**, *104*, 3501.

(244) Pant, A.; Fok, A.; Parsons, M. T.; Mak, J.; Bertram, A. K. *Geophys Res Lett* **2004**, *31*.

(245) Pope, F. D.; Dennis-Smither, B. J.; Griffiths, P. T.; Clegg, S. L.; Cox, R. A. *J Phys Chem A* **2010**, *114*, 5335.

(246) Kawamura, K.; Usukura, K. *J. Oceanogr.* **1993**, *49*, 271.

(247) Leopold, K. R.; Haim, A. *Int. J. Chem. Kinet.* **1977**, *9*, 83.

(248) Yamabe, S.; Tsuchida, N.; Miyajima, K. *J Phys Chem A* **2004**, *108*, 2750.

(249) Bertran, O.; Armelin, E.; Estrany, F.; Gomes, A.; Torras, J.; Aleman, C. *J Phys Chem B* **2010**, *114*, 6281.

(250) Cabaniss, S. E.; Leenheer, J. A.; McVey, I. F. *Spectrochim Acta A* **1998**, *54*, 449.

(251) Al-Abadleh, H. A.; Grassian, V. H. *Langmuir* **2003**, *19*, 341.

(252) Sinclair, R. G.; Mckay, A. F.; Myers, G. S.; Jones, R. N. *J Am Chem Soc* **1952**, *74*, 2578.

(253) Dalby, F. W.; Nielsen, H. H. *J Chem Phys* **1956**, *25*, 934.

(254) Fursule, R. A.; Patil, P. O.; Shewale, B. D.; Kosalge, S. B.; Deshmukh, P. K.; Patil, D. A. *Chem Pharm Bull* **2009**, *57*, 1243.

(255) Braun, A.; Wirick, A.; Kubatova, A.; Mun, B. S.; Huggins, F. E. *Atmos Environ* **2006**, *40*, 5837.

(256) Wang, J.; Morin, C.; Li, L.; Hitchcock, A. P.; Scholl, A.; Doran, A. *J Electron Spectrosc* **2009**, *170*, 25.

(257) Xu, W. L.; Fu, Y.; Willander, M. *Phys Rev B* **1993**, *48*, 11477.

(258) Felicissimo, V. C.; Cesar, A.; Luo, Y.; Gel'mukhanov, F.; Agren, H. *J Phys Chem A* **2005**, *109*, 7385.

(259) Lim, Y. B.; Tan, Y.; Perri, M. J.; Seitzinger, S. P.; Turpin, B. J. *Atmos Chem Phys* **2010**, *10*, 10521.

(260) Tillmann, R.; Hallquist, M.; Jonsson, A. M.; Kiendler-Scharr, A.; Saathoff, H.; Iinuma, Y.; Mentel, T. F. *Atmos Chem Phys* **2010**, *10*, 7057.

(261) Murthy, B. R.; Ng, J. K. K.; Selamat, E. S.; Balasubramanian, N.; Liu, W. T. *Biosens Bioelectron* **2008**, *24*, 723.

(262) Vlad, A.; Reddy, A. L. M.; Ajayan, A.; Singh, N.; Gohy, J. F.; Melinte, S.; Ajayan, P. M. *P Natl Acad Sci USA* **2012**, *109*, 15168.

(263) Beck, R. J.; Parry, J. P.; Shephard, J. D.; Hand, D. P. *Appl Optics* **2011**, *50*, 2899.

(264) Chu, L. W.; Liu, P. T.; Ker, M. D. *J Disp Technol* **2011**, *7*, 657.

(265) Staley, C. S.; Morris, C. J.; Thiruvengadathan, R.; Apperson, S. J.; Gangopadhyay, K.; Gangopadhyay, S. *J Micromech Microeng* **2011**, *21*.

(266) Zhao, S. S.; Li, Y. H.; Liu, C. *Sensor Actuat a-Phys* **2011**, *170*, 90.

(267) Schulz, M. *Nature* **1999**, *399*, 729.

(268) Muller, D. A.; Sorsch, T.; Moccio, S.; Baumann, F. H.; Evans-Lutterodt, K.; Timp, G. *Nature* **1999**, *399*, 758.

(269) Kaltenbrunner, M.; White, M. S.; Glowacki, E. D.; Sekitani, T.; Someya, T.; Sariciftci, N. S.; Bauer, S. *Nat Commun* **2012**, *3*.

(270) Sun, N. H.; Fang, G. J.; Qin, P. L.; Zheng, Q. A.; Wang, M. J.; Fan, X.; Cheng, F.; Wan, J. W.; Zhao, X. Z.; Liu, J. W.; Carroll, D. L.; Ye, J. M. *J Phys D Appl Phys* **2010**, *43*.

(271) Feldman, A. K.; Steigerwald, M. L.; Guo, X. F.; Nuckolls, C. *Accounts Chem Res* **2008**, *41*, 1731.

(272) Bulovic, V.; Burrows, P. E.; Forrest, S. R. *Semiconduct Semimet* **2000**, *64*, 255.

(273) Desiraju, G. R. *Angewandte Chemie-International Edition in English* **1995**, *34*, 2311.

(274) Lin, N.; Huang, J.; Dufresne, A. *Nanoscale* **2012**, *4*, 3274.

(275) Halasz, I. *Cryst Growth Des* **2010**, *10*, 2817.

(276) Morimoto, M.; Kobatake, S.; Irie, M. *Chem Commun* **2008**, 335.

(277) Sokolov, A. N.; Friscic, T.; MacGillivray, L. R. *J Am Chem Soc* **2006**, *128*, 2806.

(278) Turowska-Tyrk, I. *J Phys Org Chem* **2004**, *17*, 837.

(279) Li, F.; Zhuang, J.; Jiang, G.; Tang, H.; Xia, A.; Jiang, L.; Song, Y.; Li, Y.; Zhu, D. *Chem Mater* **2008**, *20*, 1194.

(280) Takahashi, S.; Miura, H.; Kasai, H.; Okada, S.; Oikawa, H.; Nakanishi, H. *J Am Chem Soc* **2002**, *124*, 10944.

(281) Bucar, D. K.; MacGillivray, L. R. *J Am Chem Soc* **2007**, *129*, 32.

(282) Reddy, C. M.; Krishna, G. R.; Ghosh, S. *Crystengcomm* **2010**, *12*, 2296.

(283) Guo, S.; Akhremitchev, B. B. *Langmuir* **2008**, *24*, 880.

(284) Hertz, H. J. *Reine Angew. Math.* **1881**, *92*, 156.

(285) Hutter, J. L.; Bechhoefer, J. *Rev Sci Instrum* **1993**, *64*, 1868.

(286) Ditzler, L. R.; Karunatilaka, C.; Donuru, V. R.; Liu, H. Y. Y.; Tivanski, A. V. *J Phys Chem C* **2010**, *114*, 4429.

(287) Sheldrick, G. M. *Acta Crystallogr A* **2008**, *64*, 112.

(288) Schmidt, G. M. J. *Pure Appl. Chem.* **197**, *27*, 647.

(289) Wornyo, E.; Gall, K.; Yang, F.; King, W. *Polymer* **2007**, *48,* 3213.

(290) Cook, R. F. *Science* **2010**, *328*, 183.

(291) Burnham, N. A.; Colton, R. J. *J Vac Sci Technol A* **1989**, *7*, 2906.

(292) Shulha, H.; Zhai, X. W.; Tsukruk, V. V. *Macromolecules* **2003**, *36*, 2825.

(293) Buth, F.; Kumar, D.; Stutzmann, M.; Garrido, J. A. *Appl Phys Lett* **2011**, *98*.

(294) Kim, S. J.; Song, J. M.; Lee, J. S. *J Mater Chem* **2011**, *21*, 14516.

(295) O'Neill, M.; Kelly, S. M. *Adv Mater* **2011**, *23*, 566.

(296) Sasabe, H.; Kido, J. *Chem Mater* **2011**, *23*, 621.

(297) Shi, J. S.; Chan-Park, M. B.; Wang, Y. L.; Yang, H. B.; Li, C. M. *J Mater Chem* **2011**, *21*, 16184.

(298) Zhang, X. J.; Wu, J. S. *Curr Org Chem* **2012**, *16*, 252.

(299) Jee, H. G.; Hwang, H. N.; Han, J. H.; Lim, J.; Shin, H. J.; Kim, Y. D.; Solak, H. H.; Hwang, C. C. *Acs Nano* **2010**, *4*, 4997.

(300) Fang, H.; Yuan, D. J.; Guo, R.; Zhang, S.; Han, R. P. S.; Das, S.; Wang, Z. L. *Acs Nano* **2011**, *5*, 1476.

(301) De Feyter, S.; De Schryver, F. C. *Chem Soc Rev* **2003**, *32*, 139.

(302) Braga, D.; Grepioni, F.; Desiraju, G. R. *Chem Rev* **1998**, *98*, 1375.

(303) Wu, S.; Shi, F.; Zhang, Q. J.; Bubeck, C. *Macromolecules* **2009**, *42,* 4110.

(304) Tang, C. B.; Sivanandan, K.; Stahl, B. C.; Fredrickson, G. H.; Kramer, E. J.; Hawker, C. J. *Acs Nano* **2010**, *4*, 285.

(305) Friscic, T.; Drab, D. M.; MacGillivray, L. R. *Org Lett* **2004**, *6*, 4647.

(306) Bhogala, B. R.; Captain, B.; Parthasarathy, A.; Ramamurthy, V. *J Am Chem Soc* **2010**, *132*, 13434.

(307) Aakeroy, C. B.; Chopade, P. D. *Cocrystals: Synthesis, Structure, and Applications. Supramolecular Chemistry: From Molecules to Nanomaterials*; Wiley: New York, 2012.

(308) Lahav, M.; Schmidt, G. M. J. *J Chem Soc B* **1967**, 239.

(309) Friscic, T.; MacGillivray, L. R. *Supramol Chem* **2005**, *17*, 47.

(310) Katz, H. E.; Huang, J. *Annu Rev Mater Res* **2009**, *39*, 71.

(311) Qiu, L. Z.; Xu, Q.; Lee, W. H.; Wang, X. H.; Kang, B.; Lv, G. Q.; Cho, K. *J Mater Chem* **2011**, *21*, 15637.

(312) Thompson, N. J.; Jandl, A. C.; Spalenka, J. W.; Evans, P. G. *J Cryst Growth* **2011**, *327*, 258.

(313) Murphy, A. R.; Frechet, J. M. J. *Chem Rev* **2007**, *107*, 1066.

(314) Chun, J. Y.; Han, J. W.; Han, J. M.; Seo, D. S. *Jpn J Appl Phys* **2009**, *48*.

(315) Anokhin, D. V.; Lejnieks, J.; Mourran, A.; Zhu, X. M.; Keul, H.; Moller, M.; Konovalov, O.; Erina, N.; Ivanov, D. A. *Chemphyschem* **2012**, *13*, 1470.

(316) Bayer, F. M.; Hiltrop, K.; Huber, K. *Langmuir* **2010**, *26*, 13815.

(317) Hitchcock, A. P.; Morin, C.; Zhang, X. R.; Araki, T.; Dynes, J.; Stover, H.; Brash, J.; Lawrence, J. R.; Leppard, G. G. *J Electron Spectrosc* **2005**, *144*, 259.

(318) Otero, E.; Wilks, R. G.; Regier, T.; Blyth, R. I. R.; Moewes, A.; Urquhart, S. G. *J Phys Chem A* **2008**, *112*, 624.

(319) Watts, B.; Swaraj, S.; Nordlund, D.; Luning, J.; Ade, H. *J Chem Phys* **2011**, *134*.

(320) Lorenz, H.; Despont, M.; Fahrni, N.; Brugger, J.; Vettiger, P.; Renaud, P. *Sensor Actuat a-Phys* **1998**, *64*, 33.

(321) Campos, L. M.; Truong, T. T.; Shim, D. E.; Dimitriou, M. D.; Shir, D.; Meinel, I.; Gerbec, J. A.; Hahn, H. T.; Rogers, J. A.; Hawker, C. J. *Chem Mater* **2009**, *21*, 5319.

(322) Hong, X. D.; Gan, Y.; Wang, Y. *Surf Interface Anal* **2011**, *43*, 1299.